Spatial and Temporal Analysis of Sodium-Ion Batteries

Dewen Hou,[§] Dawei Xia,[§] Eric Gabriel, Joshua A. Russell, Kincaid Graff, Yang Ren, Cheng-Jun Sun, Feng Lin,* Yuzi Liu,* and Hui Xiong*

Read Online

ACCESS | Metrics & More | Article Recommendations

ABSTRACT: As a promising alternative to the market-leading lithium-ion batteries, low-cost sodium-ion batteries (SIBs) are attractive for applications such as large-scale electrical energy storage systems. The energy density, cycling life, and rate performance of SIBs are fundamentally dependent on dynamic physiochemical reactions, structural change, and morphological evolution. Therefore, it is essential to holistically understand SIBs reaction processes, degradation mechanisms, and thermal/mechanical behaviors in complex working environments. The recent developments of advanced *in situ* and operando characterization enable the establishment of the structure−processing−property−performance relationship in SIBs under operating conditions. This Review summarizes significant recent progress in SIBs exploiting *in situ* and operando techniques based on X-ray and electron analyses at different time and length scales. Through the combination of spectroscopy, imaging, and diffraction, local and global changes in SIBs can be elucidated for improving materials design. The fundamental principles and state-of-the-art capabilities of different techniques are presented, followed by elaborative discussions of major challenges and perspectives.
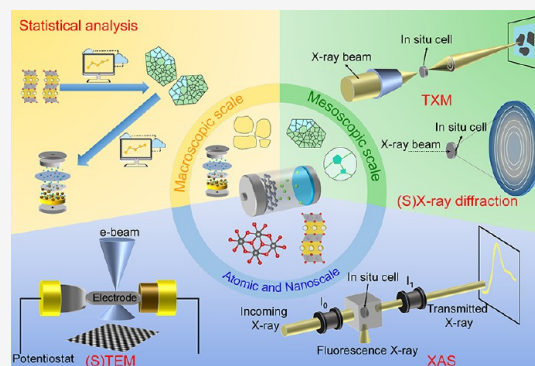
Lithium-ion batteries (LIBs) are dominant energy storage solutions in portable electronics and electrified transportation. However, risks related to the supply chain of key elements of LIBs have intensified the search for more sustainable alternatives toward decarbonization. Sodium-ion batteries (SIBs) have been considered as an appealing candidate owing to the low cost of raw materials, high natural abundance, and environmental benignity compared to LIBs. Historically, research on LIBs and SIBs began around the same time in the 1970s and early 1980s.[1−4] Since the commercialization of LIBs by Sony in 1991, research and development in LIBs skyrocketed; meanwhile, progress on SIBs slowed down because of their inferior energy density and capacity retention compared to LIBs. In the past decade, we witnessed the renaissance of SIBs with improved electrochemical performance and retained economic advantages. Despite advancements of many other beyond-Li technologies, including K-ion batteries, Mg-ion batteries, etc., SIBs best satisfy performance, cost, and scaling targets, approaching a commercialization stage recently. The revival of SIBs is also catalyzed by demands for reliable and cost-effective grid-scale energy storage systems for intermittent renewable energy sources (e.g., wind and solar).

The advantages and disadvantages of SIBs are often highlighted in open literature.[5−7] Concerning the former, first, it is acknowledged that the raw materials, e.g., sodium salts, are more abundant in the Earth's crust and more widely distributed geographically than LIBs counterparts.[7] SIB cathodes may rely less on scarce minerals containing Ni and Co. Second, sodium is free of alloy reaction with aluminum at room temperature, allowing for the use of cheaper and lighter aluminum rather than copper as the current collector for anodes to further reduce cost.[8] Third, the safety issue of SIBs is less severe: the thermal runaway during the electrode and electrolyte decomposition is much less than for the LIB counterparts.[9] Fourth, although Na^+ has a larger size than Li^+, sodium ion transport is faster in electrolytes because it is less polarizing and has smaller solvation energy.[10] The lower desolvation energy penalty is conducive to the capacity

retention at low temperature. Additionally, because of the similar working principles and cell configurations, the manufacturing infrastructure of LIBs can be readily adapted to SIBs. Last but not least, Na metal is softer than Li, and formation of dendrites may be restrained by mechanical pressure or by employing appropriate separators with higher shear modulus.[11] Considering the aforementioned merits depicted in Figure 1, SIBs can be complementary to LIBs, catering to grid storage, industrial/household power, low-speed electric cars, etc.
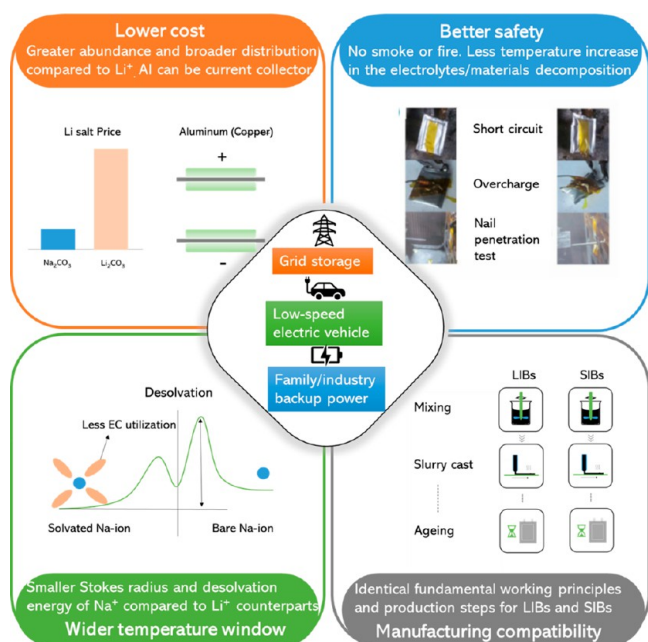

Figure 1. Schematic of major advantages of SIBs. "EC" in the bottom-left panel represents ethylene carbonate (indispensible solvent in LIBs) that hampers low-temperature performances. The figure in the top-right panel is reprinted with permission from ref 9. Copyright 2016 Elsevier.

Regarding the disadvantages, the standard electrode potential of Na (-2.70 V) is higher than that of Li (-3.04 V) with respect to the standard hydrogen electrode (SHE). In addition, Na is heavier than Li. Hence, generally speaking, the theoretical specific energy of a SIB is lower than its LIB counterpart.[12,13] Nevertheless, it has been shown that the difference in theoretical energy of LIBs and SIBs with similar electrode materials (Li: $C\|Li_{0.5}Li_{0.5}CoO_2$; Na: $C\|Na_{0.5}Li_{0.5}CoO_2$) is only ~10%, excluding the consideration of the weight of other battery components such as electrolyte, current collector, additives, and packaging.[14,15]

Over the past decade, enormous efforts have been devoted to the design of new active materials as well as improvement of existing ones for SIBs. However, the majority of the candidates to date cannot meet the stringent performance requirements for practical applications, urging fundamental understandings toward pertinent battery degradation mechanisms.

In principle, the analysis of a battery can be categorized on different spatial scales from atomic scale, primary particle scale, secondary particle scale, and electrode scale, as illustrated in Figure 2. Global information includes the phase evolution, valence change, and coordination of cations and anions, representing the averaged behaviors from all particles. Local

From the standpoint of materials science and chemistry, it is equally important to fundamentally interpret the working mechanisms of new materials involved in sodium-ion batteries, including those with seemingly limited practical value.

information includes disorder, defects, orientation, and heterogeneity, representing individual behaviors within and between particles.[16] Various processes occurring at the meso-scale involve charge distribution, phase propagation, micro-structure evolution, transition metal (TM) migration, and changes in geometric/mechanical properties.[17,18] It should be mentioned that multi-scale charge heterogeneity is universal, tremendously affecting material degradation, cycling performances, and safety. This phenomenon is modulated by reaction mechanism/grain orientation at the particle level and tortuosity/porosity at the electrode level. At the nanoscale, atomic arrangement, surface reconstruction, and solid–electrolytes interphase (SEI) formation/growth are key points of information. During cycling, all of these physical, chemical, and structural properties can potentially undergo changes.

A battery can be either an open or a closed system, which is a collection of dynamic bulks as well as interfaces. Most commonly, active materials are analyzed using different *ex situ* characterization methods at specific states of charge (SOCs) and cycles. *Ex situ* characterizations require disassembling batteries and post-treatments of battery materials, leading to potential contamination of the samples. If the tested materials are sensitive to air/moisture, they need additional protection. More importantly, during the storage and transfer, the real chemical and structural information might have altered. *Ex situ* analysis can be preliminary steps, but only the equilibrium state is probed. Therefore, to gain sufficient understanding of aforementioned dynamic changes, it is essential to apply higher-level *in situ* or real-time (operando) characterizations.

The advances of various *in situ*/operando characterization tools in LIBs serve as a cornerstone for the development of SIB characterizations. There has been phenomenal progress toward developing *in situ*/operando electron- and X-ray-based methods in LIBs, which have been summarized in many reviews.[20–24] These developments paved the way for various *in situ* and operando investigations in SIBs, including trans-mission electron microscopy (TEM), X-ray diffraction (XRD), X-ray absorption spectroscopy (XAS), X-ray imaging and tomography, and pair distribution function (PDF). Never-theless, compared to LIBs, SIBs offer ample opportunities to broaden the horizon to investigate dynamic processes such as those associated with ion–ion or ion–lattice interactions, defect evolution, and interfacial chemistry. It should be noted that properties and processes such as thermodynamic/kinetic properties and phase transitions can be distinctly different for SIBs and LIBs for similar compounds. For example, electro-chemical cycling of olivine $NaFePO_4$ is accompanied by different reaction mechanisms and partial amorphization as compared to the $LiFePO_4$ counterpart.[25] The reaction intermediates of electrodes cycled in SIBs (e.g., TiO_2, Sn) are often found to be metastable or amorphous, making them challenging to probe using *post mortem* analysis. Many of the
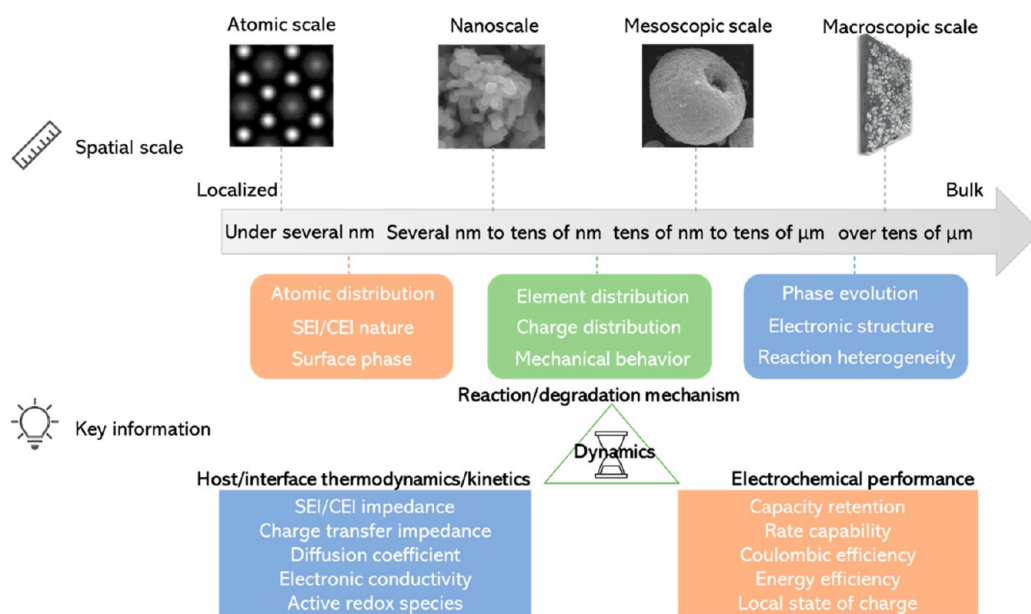
Figure 2. Scheme of a battery at different scales and underlying scientific information correlated with electrochemical properties. The image at atomic scale is from Wikipedia, while the image at the macroscopic scale is adapted from ref 19, copyright 2020 Springer Nature.

reaction pathways in electrodes used in SIBs remain elusive. Hence, it is critical to focus on the *in situ*/operando investigations that elucidate charge storage and transport mechanisms, phase transitions, crystalline-to-amorphous transformations, and morphological and mechanical responses of electrodes in SIBs during operation. Besides the hardware and protocol compatibility, the remarkable advantage of *in situ*/operando characterization of Na-based system lies in the imaging: Li in LIBs is of low Z number (3), which makes the direct measurement of spatial Li propagation under operation almost impossible. In SIBs, the increased Z (11) of Na enables the direct observation of the Na^+ migration pathway and distribution at the primary particle level.[26] These fundamental understandings will not only inspire future design of battery materials for SIBs but also provide valuable insights into the development of other battery systems.

In this Review, recent advances in *in situ* and operando characterizations for SIBs studies are summarized. The focus will be on how state-of-the-art analytical techniques facilitate the elucidation of the reaction mechanisms and degradation mechanisms in SIBs under operation. Pertinent establishment of structure—property—processing—performance relationship is based on distinct diagnosis methods that can unravel materials chemistry information, including global/local crystal structure, overall/heterogeneous electronic states, the evolution of morphology, dissolution or redistribution, thermal and mechanical dynamics of electrode materials, etc. We present research case studies organized by the class of different reaction mechanisms and discuss how complementary probing tools can be integrated. In addition, we outline the pitfalls, limitations, and perspectives for each characterization.

1. *IN SITU* TEM

TEM has been widely applied in diagnosis of battery systems. A wide range of secondary signals are produced when the incident electrons interact with a thin specimen.[27] These signals are categorized according to their corresponding analytical information: (1) imaging modes in real space, (2)

diffraction modes in reciprocal space, (3) spectroscopy mode in energy space, and (4) in temporal domains. As a result, TEM benefits from the strong interactions between electrons and materials to provide localized structural and chemical information. A typical TEM has a resolving power of ∼0.2 nm, establishing a direct communication between the lattice image and the projected crystal structure. More recently, the development of aberration-corrected (cs-corrected) TEM and cryo-TEM instrumentation has achieved higher resolution down to 0.5 Å and lower dose environment, which is particularly suitable for studies of radiation-sensitive materials. The pnCCD TEM camera employs a direct monitor which has a minimum readout speed of 1000 full frames per second with a size of 264 × 264 pixels, providing the ability to capture transient structural changes.[28] *In situ* TEM analysis at the atomic scale and nanoscale is an ideal tool for understanding reactions and phase transitions of battery materials during synthesis or insertion/extraction of Na^+ during electrochemical cycling—morphological evolution (especially volume changes of electrode materials along with Na^+ insertion/extraction), phase transformations upon charging/discharging processes, degradation mechanisms of active materials during cycling, SEI formation, and thermal stability and mechanical behaviors of electrodes.[29,30]

Primary performance metrics of SIBs include capacity, cycle life, rate capability, and safety. The electrochemical reactions of electrode materials are generally categorized into three types according to the Na^+ storage mechanism: *intercalation reaction*, *alloying reaction*, and *conversion reaction*. In order to elucidate the underlying mechanisms of these reactions, comprehensive *in situ* TEM studies have been conducted. Various *in situ* TEM designs have been successfully applied for the LIB studies.[31,32] Considering the high vacuum operation condition in the TEM, two types of configurations are commonly used for *in situ* TEM investigation: open-cell and sealed liquid-cell configurations (Figure 3). In the case of an open-cell platform (Figure 3a), working electrode directly contacts with non-volatile electrolytes (Li_2O or ionic liquid) to form a micro-cell system. Here,
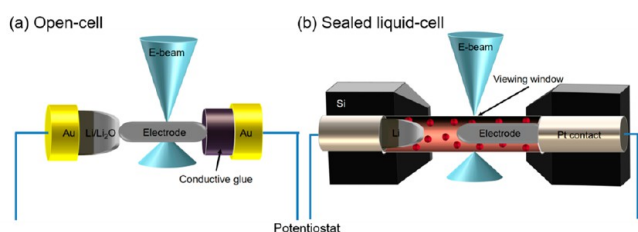
Figure 3. Schematic of *in situ* TEM experimental configurations: (a) open-cell setup and (b) sealed liquid-cell setup.

Li_2O is a product from surface oxidation of Li metal when a TEM holder is inserted into the column. Due to the direct irradiation of the electron beam onto samples, the open-cell setup allows high-resolution imaging and accurate chemical composition analysis. However, this configuration has intrinsic limitations including the electrolytes adopted being different from those in real batteries, insufficient contact area between the electrolyte and electrode, and inability to decipher the critical SEI formation process. To emulate the operation conditions in a real battery, the sealed liquid-cell configuration is designed for *in situ* TEM investigations employing a SiN_x membrane as the electron transparent windows and common electrolytes (Figure 3b). However, the resolution is downgraded, governed by the thickness of the view windows and electrolytes. To date, due to the ease of fabrication, the primary *in situ* TEM setup used in SIBs studies is the open-cell platform. Although the processes at the electrodes in the open-cell platform are not strictly electrochemical due to the absence of common electrolytes, visualization of the microstructural/mechanical evolution accompanied by phase transformation and tracking of ion diffusion deem *in situ* TEM a useful tool to obtain critical localized information upon sodiation/desodiation and failure mechanism. This section will focus on recent progress of *in situ* TEM in investigations of reaction mechanisms of electrode materials in SIBs and highlights the science accomplished by *in situ* TEM, discussing challenges and potential future directions.

1.1. Intercalation Reactions. Carbonaceous materials are the most studied intercalation anodes for SIBs due to their highly abundant resources, decent capacity, and stability. Various carbon materials including hard carbon, soft carbon, graphite, and graphene have been studied for Na storage. Na storage mechanisms in these materials remain elusive due to the limitations of the characterization techniques and their complicated structure. First, poor crystallinity in disordered carbons (e.g., hard carbon) indicates that diffraction cannot uncover sufficient information regarding disorder. Second, various types of defects and micropores present different reaction behaviors, and to identify the contribution of these factors individually to battery performance is difficult. Third, the performance of disordered carbon materials is also highly influenced by the electrolyte and SEI. Finally, microstructure variations of disordered carbon materials are closely related to the pyrolysis process, which is complex and challenging to characterize.

To date, a desirable route to characterize the evolution of the host structure and Na ions diffusion is by tracking volume change and formation processes of Na and Na_2O in the host structure during reactions.[33−37] For example, hard carbon is the most popular anode, which has an amorphous structure with multiple types of storage sites for Na ions. Three Na storage mechanisms have been proposed in hard carbon:

adsorption, nanopore filling, and intercalation.[38,39] However, the exact voltage ranges for different storage processes are still under debate due to the challenges in characterization. Based on the smaller volume expansion due to Na adsorption compared to that by Na intercalation, Wang et al.[40] determined that the sodium storage process in hard carbon undergoes two steps (Figure 4). The first step is Na^+
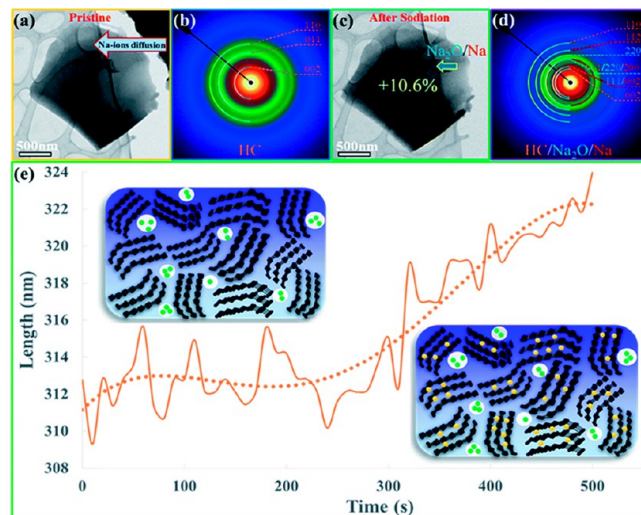

Figure 4. Sodiation of hard carbon studied by *in situ* TEM. (a, c) TEM image of the pristine and sodiated hard carbon. (b, d) Corresponding electron diffraction patterns. (e) Illustration of Na absorption and intercalation; the curves show the volume change of the hard carbon during sodiation. Adapted with permission from ref 40. Copyright 2019 Royal Society of Chemistry.

adsorption at high-energy surface sites and defect sites (corresponding to the voltage slope from ∼2 to 0.15 V vs Na/Na^+), and the second step is the intercalation process at the curved graphene platelets (∼5% expansion of the average graphene interlayer distance, corresponding to the voltage plateau near 0.15 V). The real-time visualization of volume expansion in hard carbon anode helps to unveil its charge storage mechanisms.

Apart from carbonaceous anodes, most cathode materials also possess layered structures. Various phase transformations and volume changes of cathode materials will occur during Na insertion/extraction, which might lead to battery degradation. To our knowledge, there is lack of *in situ* TEM studies on cathode materials, and it is hoped that such studies could be conducted in the future to provide in-depth understanding and references for cathode design.

1.2. Alloying Reactions. Alloying type electrodes are sodiated by forming intermetallic compounds between inserted Na ions and host elements, which present high capacity and low sodiation potential. However, a well-known issue associated with alloy-type electrodes is that they usually suffer from serious volume changes during cycling leading to capacity fading.

In situ TEM can provide direct information of electrode morphology change, including volume change and appearance of cracks. The direct imaging of morphological changes is significant to understand the degradation mechanisms of alloy electrodes. Some pure element anodes in the IV and V groups, such as Sn,[41] Sb,[42,43] Ge,[44] and Bi,[45] have been studied by *in situ* TEM, where distinct Na (de)alloying behaviors are
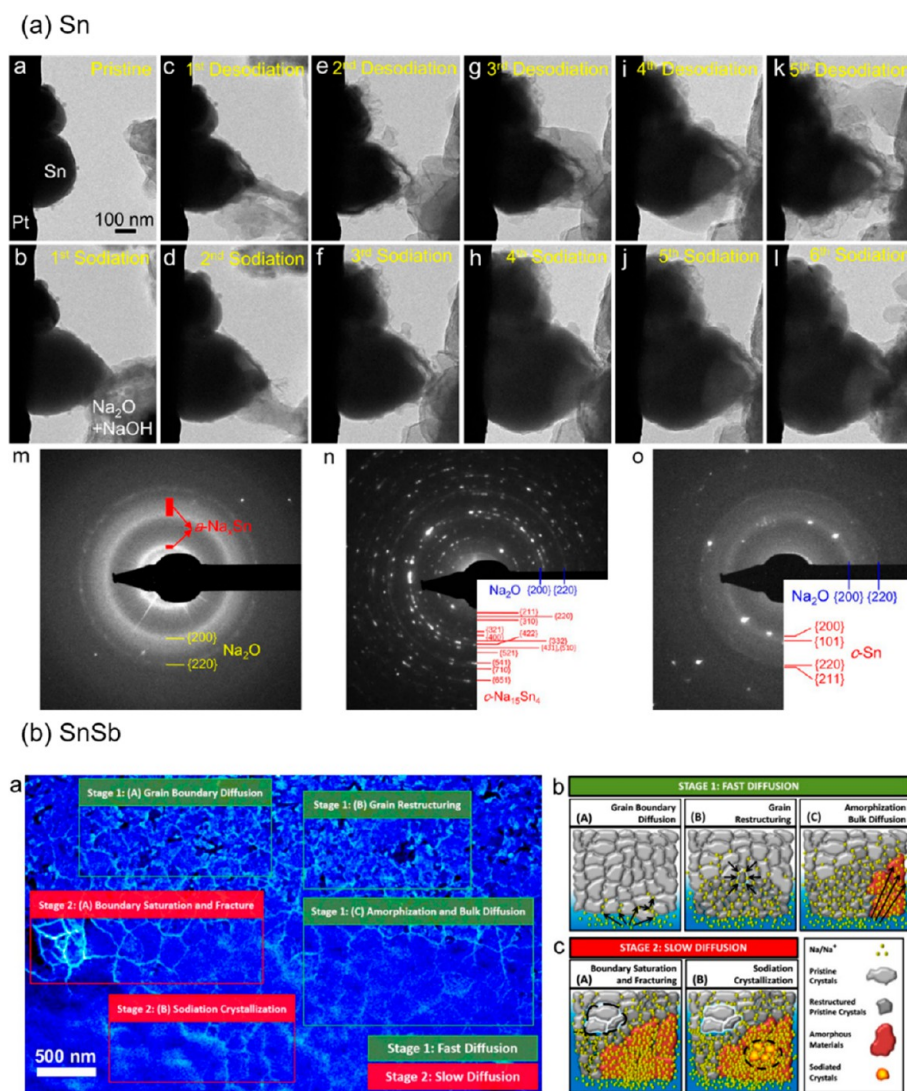
Figure 5. *In situ* TEM studies for alloying electrode materials in sodiation/desodiation cycles. Microstructural evolution of the (a) Sn nanoparticles. Reprinted with permission from ref 41. Copyright 2012 American Chemical Society. (b) Microstructure evolution during sodiation in SnSb thin-film anodes. Adapted with permission from ref 47. Copyright 2019 American Chemical Society.

elucidated. Meanwhile, complex phase transformation also occurs in alloy electrode materials during electrochemical cycling. Microcosmic information of phase transformation can be identified by *in situ* electron diffraction, which is extremely useful when reactions involve multiple intermediates and sometimes amorphorization. For example, Sn undergoes reversible two-step phase transformations during sodiation/desodiation, involving the formation of an amorphous intermediate Na_xSn and the fully crystallized $Na_{15}Sn_4$ phase (Figure 5a).[41] From these *in situ* investigations, the phase transformation is accompanied by large volume changes during electrochemical cycling, which results in quick capacity fading. These findings indicate that the application of pure alloying-type elements as electrodes may not be promising, and optimizations of electrode and electrolyte need to be considered.

One approach to mitigate volume expansion of pure element alloying-type electrodes is to add (in)active elements forming intermetallic compounds. However, when alloying/dealloying with Na, different elements have different electrochemical reaction kinetics, leading to a more complex reaction process

than that of a pure element electrode. For instance, in the binary β-SnSb intermetallic electrode, Sn and Sb are sodiated sequentially rather than simultaneously, leading to discontinuous increases in the diameter of the nanowire.[46] In addition, Unocic and co-workers investigated the sodiation kinetics of nanocrystalline SnSb thin film and observed during *in situ* sodiation the electrode initially underwent amorphorization.[47] They further quantitatively analyzed the sodiation kinetics using time-lapsed bright-field TEM images to extract Na^+ diffusion coefficient and suggested that microstructural changes play a critical role in Na^+ transport (Figure 5b).

1.3. Conversion Reactions. Materials such as TM oxides, sulfides, and fluorides, which are based on conversion mechanism, are another prospective class of electrode candidate for SIBs owing to their high specific capacity. However, conversion-type electrodes normally suffer from severe capacity decay, low ionic/electronic conductivity, poor initial Coulombic efficiency, and relatively large volume change.[48] Understanding of fundamental reaction mechanisms in this family of electrode materials is still challenging due to reasons such as formation of amorphous intermediates. The
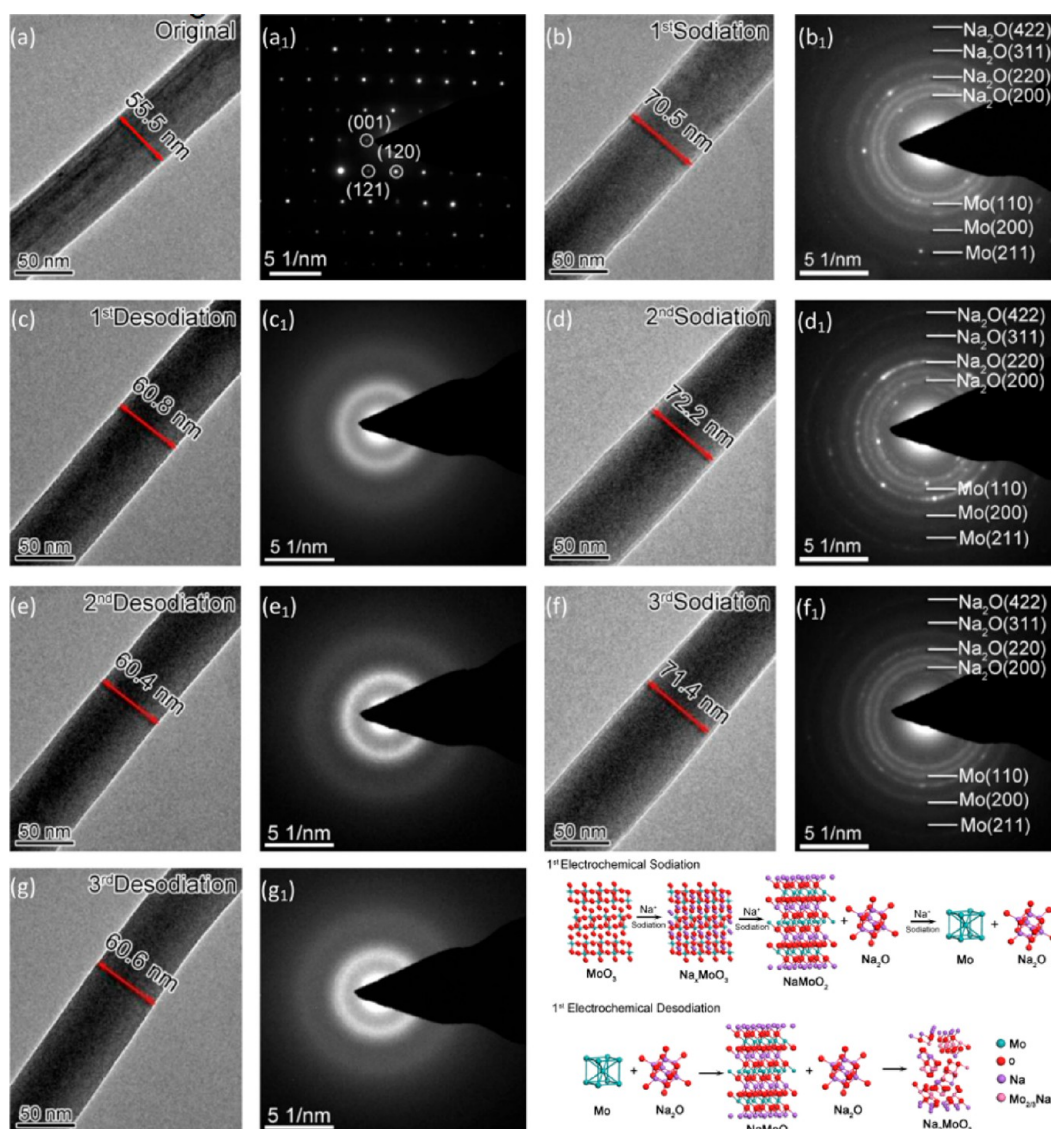
Figure 6. *In situ* TEM investigation of the microstructural evolution of conversion-type α-MoO$_3$ electrode during Na diffusion. Reprinted with permission from ref 54. Copyright 2016 Elsevier.

volume expansion and corresponding cycling performance in conversion electrodes are related to their complex phase transformations. These changes can be directly visualized by *in situ* TEM during Na$^+$ insertion/extraction. Especially, detailed local crystallographic information, heterogeneous reaction processes, and subtle structural changes can be probed by electron diffraction and fast Fourier transform (FFT).

In situ TEM can capture the reversible metallic phase formation in some conversion metal oxide electrodes, such as Co$_3$O$_4$,[49,50] NiO,[51] and ZnO.[52,53] It is found that metal nanoparticles after oxide reduction are interconnected to form a metallic network and disperse within Na$_2$O matrix, providing a good electron pathway. However, the Na$_2$O that formed during sodiation can block further transport of Na$^+$, and the quantity of Na$_2$O will gradually accumulate as the cycle progresses, leading to deteriorated diffusion kinetics. Irreversible volume change also occurs during Na$^+$ insertion/extraction, further degrading host materials. In addition, crystallographic defects, including point defects, line defects, and planar defects, are usually generated during electrochemical process, which may change the mechanical and electronic properties of host materials. Compared to other characterizations, *in situ* high-resolution TEM (HRTEM) can capture these defects directly. Defects in crystal lattice are often considered to reduce battery performance, but *in situ* TEM studies found that defects are somehow conducive to improving SIBs reaction kinetics. For instance, high-density dislocations in polycrystalline ZnO nanowires enable improved ductility and thus the cycling performance of the ZnO/Na cell.[52] Performance optimizations are expected to benefit from these findings by utilizing crystal defects (vacancies, dislocations, stacking faults, interfaces, etc.) produced during cycling and material synthesis.

In situ TEM is powerful to track microstructural changes of chemically identical electrode materials upon sodiation. Xu et al.[53] investigated the sodiation behaviors of single-crystalline (sc) and polycrystalline (pc) ZnO nanowires (ZNWs). *In situ* TEM distinctly showed that while the non-uniform sodiation in sc-ZNWs manifested a slow step-by-step propagating displacement reaction front as well as the generation of heterogeneous interfaces, pc-ZNWs underwent ultrafast sodiation which possibly was associated with unobstructed

ionic transport pathways among ZnO nanograins. The results highlight the benefit of *in situ* TEM to probe different microstructural responses in chemical identical electrode materials under operation.

In situ TEM can be used to probe reaction intermediates of complex reactions and monitor the reversibility of conversion electrodes. Xia et al.[54] studied the chemo-mechanical dynamics of α-MoO_3 nanobelts which undergo multi-step phase transitions and volume changes during electrochemical cycling (Figure 6). During the first sodiation, the orthorhombic α-MoO_3 transforms to amorphous Na_xMoO_3, followed by the formation of the crystalline $NaMoO_2$ phase, then further transformed to the final mixture of crystalline Mo nanograins and Na_2O. By tracking the swelling of the nanobelt at different time, the conversion reaction rates are measured in the range of 1−30 nm s^{-1}. Upon the next desodiation, the sodiated products are consumed but not fully transformed back to the pristine state, indicating that an irreversible phase transformation occurred in the first cycle. The phase transformation afterward is reversible between crystalline Mo and amorphous Na_2MoO_3. The volume expansion is 27% after the first sodiation and 16−19.5% during subsequent cycles, giving rise to the different Coulombic efficiencies during cycling. Such first-cycle irreversible phase transformations have also been observed by *in situ* TEM in the $NiCo_2O_4$,[55] CuO,[56−58] and MnO_2,[59,60] as well as some metal sulfides/selenides, like Ni_3S_2,[61] FeSe,[62] Cu_2S,[63] and Co_9S_8.[64]

1.4. Mixed Reactions. In addition to single-reaction mechanisms, certain electrode materials exhibit more than one reaction mechanism. As discussed above, reaction mechanisms of different types of materials can be revealed by *in situ* TEM (either imaging mode in real space or diffraction mode in reciprocal space) and at various length scales (from micron scale to nanoscale). Meanwhile, ultra-fast acquisition time ensures temporal resolution to monitor the dynamic reaction processes; thus, *in situ* TEM analysis is expected to empower researchers to elucidate complex and heterogeneous electrochemical reactions with more than one type of charge storage mechanisms.

Phosphorus-based materials are intercalation-alloying-type electrodes, possessing high theoretical capacity (e.g., 2596 mAh g^{-1} for P) and low redox potential.[65] P-based materials with open space in their crystal lattice allow the intercalation of Na$^+$ prior to alloying reactions. Nevertheless, serious structural changes and poor electronic conductivity of the electrodes tend to induce electrode pulverization and thus rapid capacity fade. Recently, Sun et al.[66] revealed that intercalation and alloying-type reactions dominate in black phosphorus for Na storage. The *in situ* TEM observations before and after sodiation show that intercalation is achieved by Na$^+$ insertion into phosphorus layers along the *x*-axis-orientation channel. The alloying reaction leads to high specific capacity but reduces cycling performance due to anisotropic expansion during sodiation. In other *in situ* TEM investigations, it is found that this anisotropic expansion arises from anisotropy of Na diffusion and insertion strain in black phosphorus.[67,68]

Some conversion-type materials with open sites in their crystal lattices, such as FeP,[69] TiS_2,[70,71] MoS_2,[72,73] FeS_2,[74] and CaV_4O_9,[75] undergo an intercalation reaction prior to the conversion reaction. Multi-step reaction behaviors are observed in these materials by *in situ* TEM. For example, in 1D shape polycrystalline FeS_2 nanotubes, Na intercalation in spinel FeS_2 results in the formation of crystalline $NaFeS_2$ in the

early stages of sodiation while further Na interclation converts $NaFeS_2$ into Fe and Na_2S (Figure 7).[76] Upon following
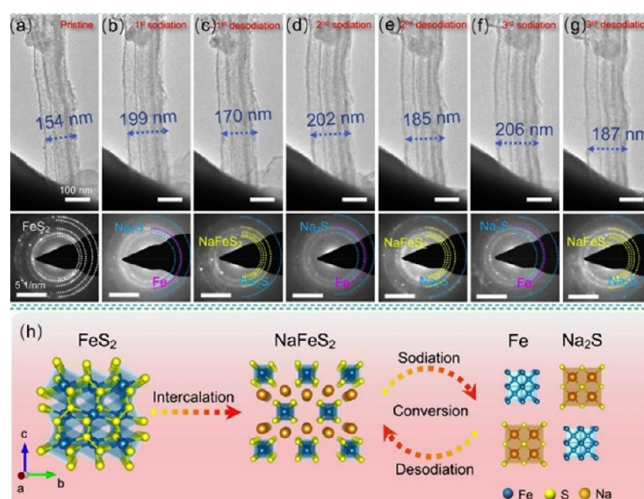

Figure 7. Intercalation−conversion reaction: FeS_2. Reprinted with permission from ref 76. Copyright 2019 Elsevier.

desodiation, the as-formed Fe and Na_2S transformed to crystalline $NaFeS_2$ rather than pristine FeS_2. This conversion reaction between $NaFeS_2$ and Fe/Na_2S is reversible after the first cycle.

For some conversion-type electrodes, if the metal cation can react with Na (e.g., Sn, Sb, and Bi), the sodiation process usually undergoes an intercalation−conversion−alloying reaction pathway and exhibits different reaction kinetics during various reaction steps.[77−82] Such differences are probably caused by the difference in mobility of Na$^+$ in different lattice frames.[83] Thus, it is necessary to further understand the differences in various conversion-type materials by *in situ* TEM. These *in situ* TEM findings, especially the localized morphological and structural characteristics at nanoscale, support structural engineering and surface modification on the improvement of the cycling stability of the conversion-type electrodes.

1.5. Thermal Stability and Mechanical Property. In principle, structural changes might originate not only from the Na$^+$ insertion into the host but also from the increase of temperature, which might cause battery degrade. At high temperature the material breakdown is normally accompanied by remarkable oxygen evolution, resulting in thermal runaway with flammable electrolytes.[84,85] Thus, it is important to understand the intrinsic thermal behaviors of electrodes during operation. An *in situ* heating chip in the unique TEM holder can precisely control the temperature and heating rate, which can be applied to reveal the thermal degradation process of electrodes.

Recently, Liu et al.[86] quantitatively analyzed the thermal degradation processes of mechanically exfoliated 2D black phosphorus by *in situ* (S)TEM and found that the crystal structure of the black phosphorus flakes appear unchanged when the annealing temperature is below 400 °C (Figure 8a). Amorphization occurs after annealing above 400 °C, and the flake remains amorphous after holding at 500 °C for 20 min. Black phosphorus degradation proceeds by sublimation, which occurs at edges/defects of flakes and propagates as eye-shaped cracks, rather than melting.
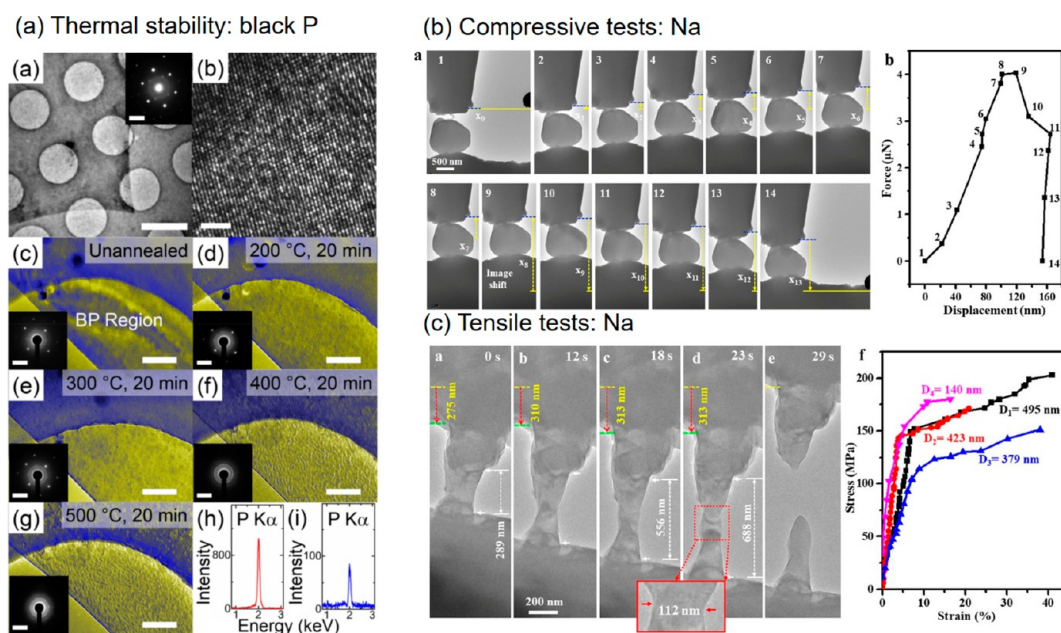
Figure 8. (a) *In situ* heating of black phosphorus. Adapted with permission from ref 86. (b) *In situ* compression and unloading processes for a Na particle and (c) *in situ* tensile tests of a Na dendrite. Reprinted with permission from ref 87. Copyright 2020 American Chemical Society

In situ mechanical testing in the TEM has been widely applied in various bulk materials to study their deformation behaviors and mechanical properties. Through delicate experimental designs, mechanical properties of materials and the corresponding structural evolution can be obtained simultaneously, establishing the relationship between structural and mechanical properties. Recently, this design has been adopted to study the mechanical properties of dendrites in sodium metal batteries. Like Li, Na metal can form dendrites during deposition leading to safety issues. Liu et al.[87] reported the *in situ* electro-chemo-mechanical response of Na dendrites and SEI during cycling via an environmental TEM–atomic force microscopy (ETEM-AFM) platform which allows operation in a CO_2 atmosphere. During electrochemical plating, nanostructured Na deposition, approximately Na dendrites, appear but is stabilized by a SEI layer (<20 nm). The surface is predominantly comprised of Na_2CO_3. The mechanical nature of Na dendrites is measured using *in situ* compression and tension tests (Figure 8b,c). The compressive and tensile strengths range from 36 to 203 MPa, and Young's modulus varies from 1.3 to 3.5 GPa. Such dendrites are distinct from bulk Na metal (the stress varies from 0.1 to 0.25 MPa at 8% strain with Young's modulus of ∼ 3.9 GPa).[88] The higher strength in Na dendrites is considered to be a result of the reinforcement of the Na_2CO_3 SEI layer, which possesses a compressive strength varying from 261 to 682 MPa. The mechanical properties of other SEI components, such as NaF, Na_2O can be more focused, as a Na whisker is easier to generate compared to its Li counterpart.

In this section, recent *in situ* TEM studies of SIB electrodes during cycling are summarized in terms of dynamic phase transformation, structural evolution, reaction kinetics, thermal stabilities, and mechanical properties. While a fundamental understanding can be provided by *in situ* TEM approach, innovation is necessary for further study: (1) As the "pseudo" electrolyte (i.e., Na_2O) typically used in current *in situ* TEM might not reflect the real circumstance in a SIB, it is necessary

to use sealed liquid-cell configuration and design new *in situ* TEM cells that can mimic the working conditions of practical battery systems. (2) Only individual nanoparticle is observed in most *in situ* TEM works, inviting questionable representativeness. It is also challenging to observe the effect of the surrounding environment near the particle. Thus, it is necessary to combine *in situ* TEM with other techniques to gain a holistic perspective both locally and globally in multiple modalities across a large range of length scales. (3) Current *in situ* TEM setups can only run for a few cycles, which limits investigations of the evolution of electrodes under long-term cycling. (4) The electron beam and the TEM vacuum condition will influence the materials and electrochemical processes involved. Proper operation conditions are critical to less artifacts. (5) The formation of SEI profoundly influences the SIBs degradation, especially for full cell construction. However, there is very limited understanding of the formation and evolution of SEI in SIBs due to the lack of methods that can be used to directly characterize SEI. (6) Compared to Li, Na can be directly imaged by STEM technique, which is a great potential to track Na ion transport during electrochemical reactions. Cryo-TEM excels at characterizing SEI but the low-temperature environment imposes grand challenges on mimicking real cell operation. With the continuous development of electron microscopy, including the application of advanced new techniques in battery systems, such as 4D-STEM, a comprehensive understanding of electrode materials in SIBs could be achieved in the future.

2. *IN SITU*/OPERANDO XRD

XRD is a well-established technique essential to obtain structural information to understand the electrochemical reaction mechanisms of electrode materials. XRD characterization is based on the X-ray elastic scattering by periodically ordered atoms inside a crystalline material, producing constant diffraction patterns that provide average structural information with length scales from angstroms to microns.[89] XRD pattern

(a) Carbon

(c) O3-$Na_{1.2}Ni_{0.2}Mn_{0.2}Ru_{0.4}O_2$

(b) P2-$Na_{2/3}MnO_2$

(d) NASICON-type $Na_3MnTi(PO_4)_3$
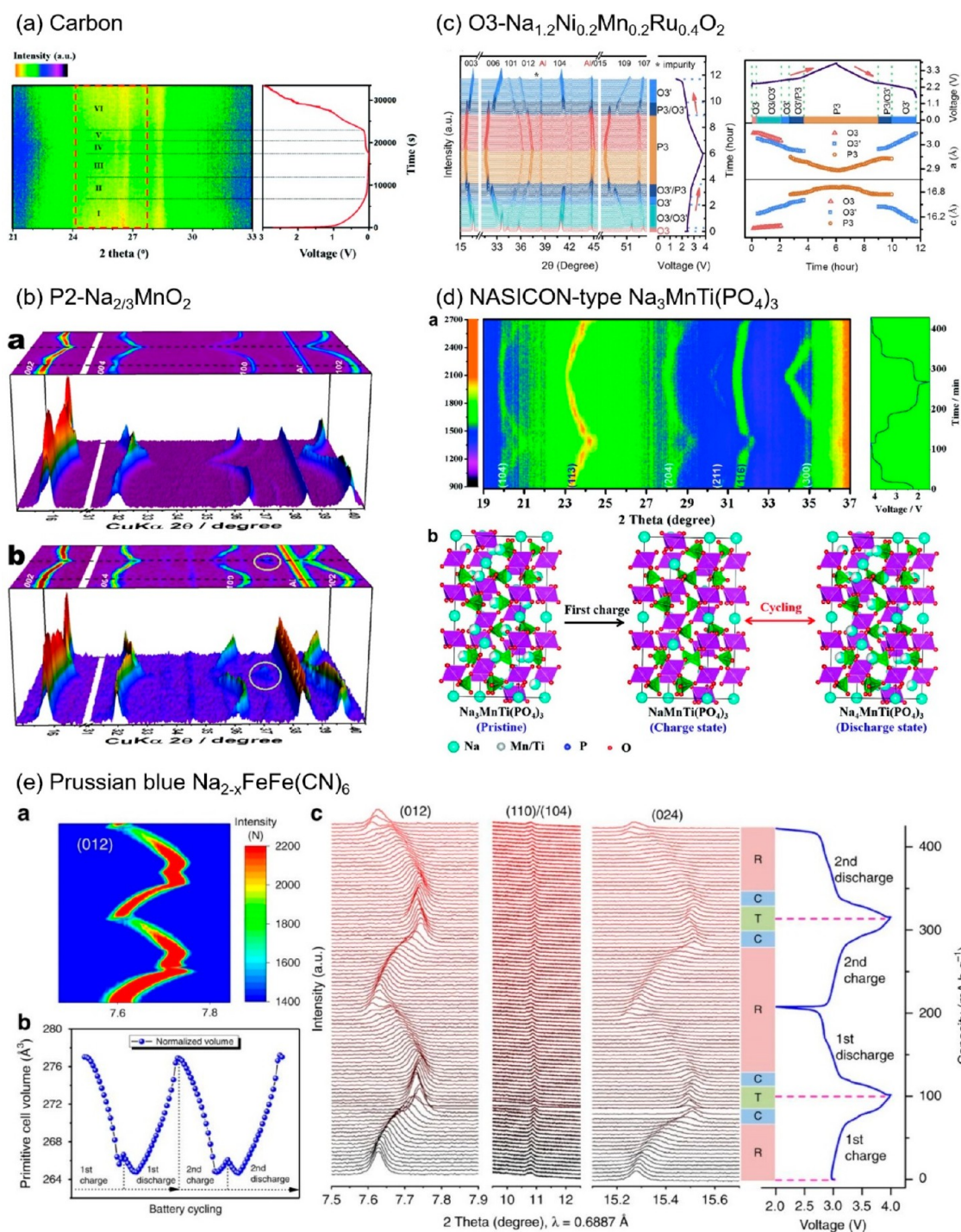
(e) Prussian blue $Na_{2-x}FeFe(CN)_6$

Figure 9. *In situ*/operando XRD investigations in intercalation-type electrode materials. (a) *In situ* XRD mapping of hard carbon anode during the first cycle at 200 mA g^{-1} at room temperature. Adapted permission from ref 97. Copyright 2017 Wiley. (b) Operando XRD of P2-$Na_{2/3}MnO_2$ (top panel) and P2-$Na_{2/3}[Mn_{0.8}Co_{0.2}]O_2$ (bottom panel). Reprinted with permission from ref 111. Copyright 2019 American Chemical Society. (c) *In situ* XRD of $Na_{1.2}Ni_{0.2}Mn_{0.2}Ru_{0.4}O_2$ (left panel) and the corresponding lattice parameters evolutions (right panel). Adapted with permission from ref 120. Copyright 2018 Elsevier. (d) *In situ* XRD of the $Na_3MnTi(PO_4)_3$ cathode cycled at 50 mA g^{-1} and schematic illustration showing Na$^+$ (de)intercalating from/into $Na_3MnTi(PO_4)_3$ cathode upon electrochemical processes. Adapted with permission from ref 122. Copyright 2019 Wiley. (e) 2D contour map of (012) reflection plan of $Na_{2-x}FeFe(CN)_6$ (top-left panel), and normalized volume during cycling obtained from *in situ* SXRD patterns (bottom-left panel), as well as (012), (110)/(104), and (024) reflection planes of *in situ* SXRD patterns (right panel). Reprinted with permission from ref 123. Copyright 2020 Springer Nature.

is as unique as fingerprint, which enables routine qualitative analysis for crystalline materials. Detailed structural information on battery materials is obtained by performing refinement, including the symmetry, chemical composition, atomic positions, site occupancies, lattice parameters, etc.[90,91] *In situ*/operando XRD is used to monitor the structural evolutions including lattice and atomic occupation change of materials during cycling. Specifically, compared to laboratory

XRD and conventional emission spectroscopy, synchrotron-based XRD (SXRD) with higher photon energies and intensities provides stronger penetration power, better signal-to-noise ratios, as well as higher spatial and temporal resolution.[92,93] Thus, SXRD greatly shortens the acquisition time (∼10−30 min for laboratory XRD and ∼10 s for SXRD) and enable investigations close to real time (operando). In general, for intercalation electrode materials, there are two typical reaction characteristics: the single-phase solid reaction without phase transformation, namely solid-solution reaction, and the phase-transition reaction mechanisms. In the former reaction, only the shift of initial diffraction peaks can be observed without symmetry change during cycling. In phase transition, the materials undergo symmetry changes leading to new peak appearing or old peak disappearing, depending on symmetry. Due to the popularity of this method, there are several reviews with the focus on this topic in general.[92−94] For distinction, this section is mainly focused on the important development and perspectives of the in situ/operando XRD in SIBs. The focus aims to deliver holistic overview of the advancements and challenges of this method in various SIBs operating conditions.

2.1. Intercalation Reactions. In contrast to TEM, XRD can be performed in real battery configurations, allowing for in situ/operando studies at larger length scales.[95] A variety of in situ and operando XRD setups have been developed, such as modified coin cell, pouch cell, Argonne's multipurpose in situ X-ray (Ampix) cell, radially accessible tubular in situ X-ray cell, and capillary-type cell.[96] In situ/operando XRD has been widely used to probe the structural change and phase transformation of various intercalation-type electrodes. Compared with alloying- and conversion-type electrodes, the structural changes in intercalation-type electrodes are less substantial. For example, adsorption−insertion mechanisms of Na^+ into typical carbonaceous materials were studied by Qiu et al.[97] combining high-resolution in situ XRD and other techniques, as well as simulations. Na^+ intercalates into the regions of graphene layers with relatively wide spacing, resulting in relatively large interlayer spacing, reflected by the Bragg peak at lower angle (Figure 9a). Another part of graphite layers with narrow spacing hardly allows Na^+ intercalation; thus, the Bragg peak remains in its initial position. The split reflections merge into a single peak during Na extraction, indicating reversible structure change.

Ti-based compounds are widely studied as anode for SIBs, which store Na through intercalation-type reaction. Recently, from in situ (S)XRD findings, it is found that Ti oxides with different polymorphs exhibit different reaction kinetics. Anatase TiO_2 undergoes an irreversible amorphization upon the first sodiation, and the amorphous phase yields pseudocapacitive sodium storage mechanisms upon subsequent cycles.[98] However, TiO_2-B electrode with monoclinic structure undergoes a single-phase reaction upon sodiation/desodiation cycles, yet a portion of the intercalated Na^+ is not reversibly extracted from TiO_2-B structure, resulting in an unfavorable initial Coulombic efficiency.[99]

Layered transition metal oxides are another intercalation-type electrode material for SIBs. According to the Na coordination environment (prismatic and octahedral) and the packing sequence of oxygen layers (ABBA and ABCABC), layered transition metal oxides are usually categories following the notation by Demas: P2-type and O3-type.[100] It is well known that there are often complex crystal structural changes

and multi-phase transitions in various layered metal oxide structures, which have considerable impacts on SIBs performance. In situ/operando XRD identifies crystal structure of bulk electrode materials during cycling, including phase, lattice parameter, atomic position, site occupancy, stacking faults, strain, and texture, which reveals the effect of these evolutions on SIBs performance.

P2-type cathode materials have large prismatic sites for Na^+ which often undergo undesired P2- to O2- or P′2 (OP4)-type phase transformation in high-voltage regions, causing rapid capacity decay. This phase transformation reaction mechanism has been elucidated by in situ/operando XRD in different P2-type electrode materials, such as $Na_{2/3}Ni_{1/3}Mn_{2/3}O_2$,[101,102] $Na_{0.44}MnO_2$,[103] $Na_{0.75}Ni_{0.22}Co_{0.78}O_2$,[104] $Na_{0.7}Fe_{0.4}Mn_{0.4}Co_{0.2}O_2$,[105] $Na_{2/3}Mn_{0.8}Fe_{0.1}Ti_{0.1}O_2$,[106] $Na_{0.7}[Cu_{0.15}Fe_{0.3}Mn_{0.55}]O_2$,[107] $Na_{0.66}Li_{0.18}Mn_{0.17}Mg_{0.21}Co_{0.08}O_2$,[108] etc. In order to mitigate this problem, other elements have been adopted to substitute Na sites or TM sites and suppress the P2-O2 phase transition for better electrochemical performance.[109] For instance, Xiong et al.[110] recently investigated the effect of Li doping on the electrochemical properties of P2-$Na_{0.67}Ni_{0.33}Mn_{0.67}O_2$ cathode. It was found that Li occupancy on different sites (Na sites and/or TM sites) in the P2 structure has different effects on the crystallographic stability and electrochemical performance. According to the operando SXRD measurements, these different effects lead to the different structural stability (relates to lattice parameters change) during cycling. Myung and co-workers studied the influence on different content of Co dopant in P2-$Na_{2/3}MnO_2$ and probed the structural change of optimal P2-$Na_{2/3}[Mn_{0.8}Co_{0.2}]O_2$ compound via operando XRD.[111,112] The whole cycling process of the P2-$Na_{2/3}[Mn_{0.8}Co_{0.2}]O_2$ electrode exhibits a typical single-phase reaction, which is accompanied by only peak shifts and no new peaks appearance (Figure 9b). Regarding the P2-$Na_{2/3}MnO_2$ compound, besides the peaks shift, a new phase arises around 37.5° during discharge, which is recognized as the phase evolution from the P2 to P′2 phase. Operando XRD results revealed that the Co-doped material can maintain the initial P2 structure, leading to a small volume change. Likewise, the substitution of Cu,[113] Zn,[114] Mg,[115] as well as co-substitution of Cu and Mg[116] for Ni in P2-$Na_{2/3}Ni_{1/3}Mn_{2/3}O_2$ can also endows P2 phase by less severe phase transformation, contributing to improve structural reversibility.

Compared to the P2-type structure, the O3-type structure has a higher Na content, and Na^+ ions reside at octahedral sites. In situ/operando XRD studies show that there is often a series of biphasic, triphasic, and solid-solution multi-phase transformations from O3- to P3- and to O′3-type structures which cause capacity fade.[117] The addition of a certain amount of dopants can also improve the O3-type structural stability.[118,119] Su et al.[120] reported a ruthenium substituted sodium-excess O3-type $Na_{1.2}Ni_{0.2}Mn_{0.2}Ru_{0.4}O_2$ cathode, which shows enhanced cycling stability. The material undergoes the sequential phase transitions of O3−O3′ (a new hexagonal O3-type phase with a larger (001) interplanar distance compared to the pristine O3 structure)−P3 during charge and P3−O3′ during discharge in the first cycle (Figure 9c). In the subsequent cycles, the single reversible phase transformation between P3 and O3′ dominates, leading to the smooth voltage curve and cycle stability of the $Na_{1.2}Ni_{0.2}Mn_{0.2}Ru_{0.4}O_2$.

Besides layered transition metal oxides, polyanionic compounds (Na superionic conductor compounds (NASI-

CON-type), pyrophosphates, mix-polyanion) and Prussian blue analogues are also used for Na storage due to their open framework structure which could easily accommodate sodium ions. Recently, Mai's group used high-resolution *in situ* XRD to study the phase transformation behaviors in a NASICON-type cathode material of $Na_3V_2(PO_4)_3$ at different scan rates and different temperatures.[121] The materials form a one-phase solid solution upon desodiation rather than common two-phase reactions. They later designed another NASICON-structured $Na_3MnTi(PO_4)_3$ cathode for SIBs and found that both solid-solution and two-phase transformation reactions occur in this material during electrochemical cycling.[122] As illustrated in Figure 9d, the diffraction peaks (104), (113), (204), and (300) exhibit reversible shifts during cycling, indicating a solid-solution reaction. Meanwhile, presence/absence of (211) and (116) peaks indicate a biphasic reaction. Wang et al[123] fabricated a series of sodium-rich Prussian blue $Na_{2-x}FeFe-(CN)_6$ for SIBs and investigated their electrochemical reaction mechanisms. Based on *in situ* SXRD investigations, the highly reversible three-phase transformations between rhombohedral, cubic, and tetragonal are observed during Na$^+$ (de)-intercalations (Figure 9e).

2.2. Alloying and Conversion Reactions. In addition to intercalation-type electrode materials, *in situ*/operando XRD has also been used to study the electrochemical reaction mechanisms of various electrode materials based on alloying and conversion reactions, as well as complex mixed reactions involving two or three reactions. Although *in situ* TEM has revealed complex reaction mechanisms during sodiation/desodiation, *in situ* and operando XRD studies provide more realistic pictures of the reaction process on a global scale. For example, in the case of alloying reactions, Palaniselvam et al.[124] studied the (de)sodiation reaction mechanisms of tin-carbon composite anodes using *in situ* XRD. A gradual disappearance of the Sn diffraction peaks along with the appearance of some new broad reflections during discharging, indicating that several Na-Sn intermediates with limited crystallinity are formed during sodiation (Figure 10a). This behavior is in agreement with their recent findings[125] and the results from Obrovac and co-workers.[126] The reaction partially reverses during desodiation, as several unknown intermediates appear again until the final Sn forms. These (de)alloying reaction mechanisms were also demonstrated in other alloying-type anode materials using *in situ*/operando XRD studies, such as Bi,[127] Sb,[128] Pb,[129] SnSb,[130] Bi-Sb alloy,[131] and Fe-Sb intermetallic alloy.[132]

In the case of conversion-type electrode, some direct conversion reactions observed by *in situ* TEM have been supported by *in situ* XRD investigations.[133] For example, according to the *in situ* XRD patterns, the MoP anode undergoes a typical conversion-type reaction (Figure 10b).[134] It is noted that minor peaks of Na_3P and Mo are observed after the first cycle, indicating incomplete reversibility of MoP anode. In some electrode materials with mixed reactions, *in situ*/operando XRD analysis also provides detailed information in reaction pathways.[135−137] For example, the *in situ* XRD of Sb_2Se_3 nanorods anode shown by Ou et al.[138] presents typical initial intercalation and subsequent conversion and alloying reactions. According to the reaction sequence (Figure 10c) revealed by cyclic voltammetry, a six-stage reaction mechanism can be derived. When the battery is discharged to 1.1 V (first stage), the peaks of Sb_2Se_3 shift to lower 2θ, suggesting the Na$^+$ intercalation into host materials and the formation of
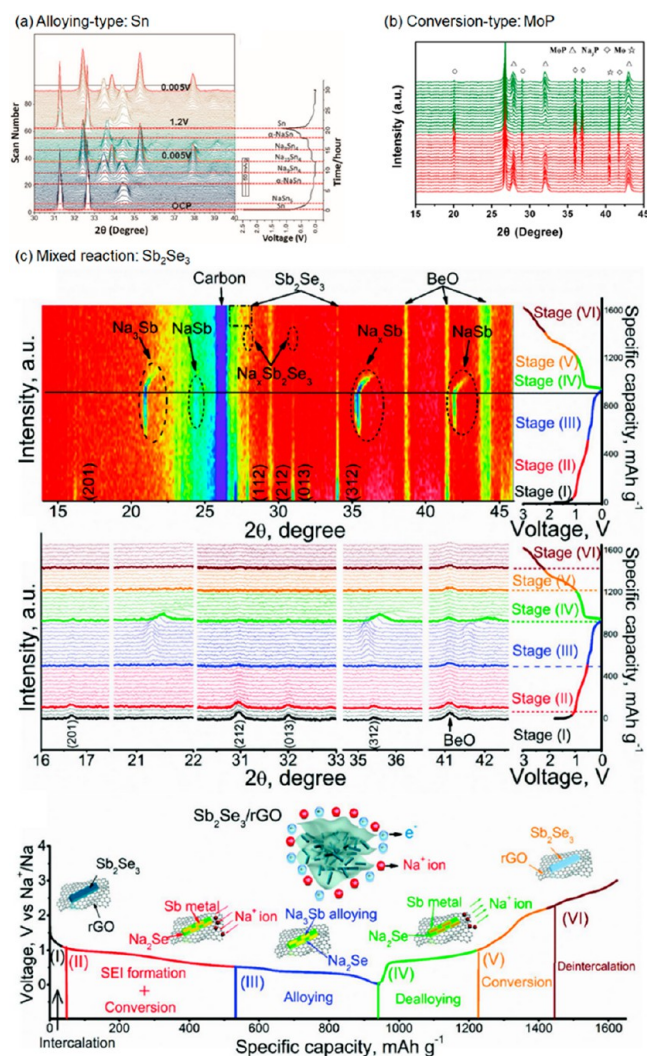

Figure 10. *In situ*/operando XRD in alloying-type and conversion-type electrode materials. (a) *In situ* XRD patterns of Sn and corresponding voltage profiles. Reprinted with permission from ref 124. Copyright 2019 Wiley. (b) *In situ* XRD of MoP during the first cycle at a voltage range between 0.01 and 3.0 V. The green and red curves represent the charge and discharge process. Reprinted with permission from ref 134. (c) *In situ* XRD of Sb_2Se_3 during the initial cycle and schematic of the reaction mechanism during charge/discharge process. Adapted with permission from ref 138. Copyright 2017 Wiley.

intermediate $Na_xSb_2Se_3$. When discharged to 0.6 V (second stage), the peaks of Sb_2Se_3 become gradually weakened in intensity until complete disappear accompanying with the appearance of new peaks of Na_2Se and Sb, indicative of conversion reaction from $Na_xSb_2Se_3$ to Na_2Se and Sb. When the battery is fully discharged to 0.01 V (third stage), the new peaks of NaSb and Na_3Sb appear, implying that the alloying reaction occurs between Na$^+$ and Sb. During the subsequent charging process, the reverse phase transformations sequentially occur, which are in agreement with the results of electrochemical measurement.

2.3. Thermal Behaviors. *In situ*/operando XRD also facilitates studying thermal behaviors of electrode materials during synthesis and electrochemical processes. Unlike the vacuum environment of TEM, *in situ* heating XRD can be operated in ambient condition, thus providing more accurate
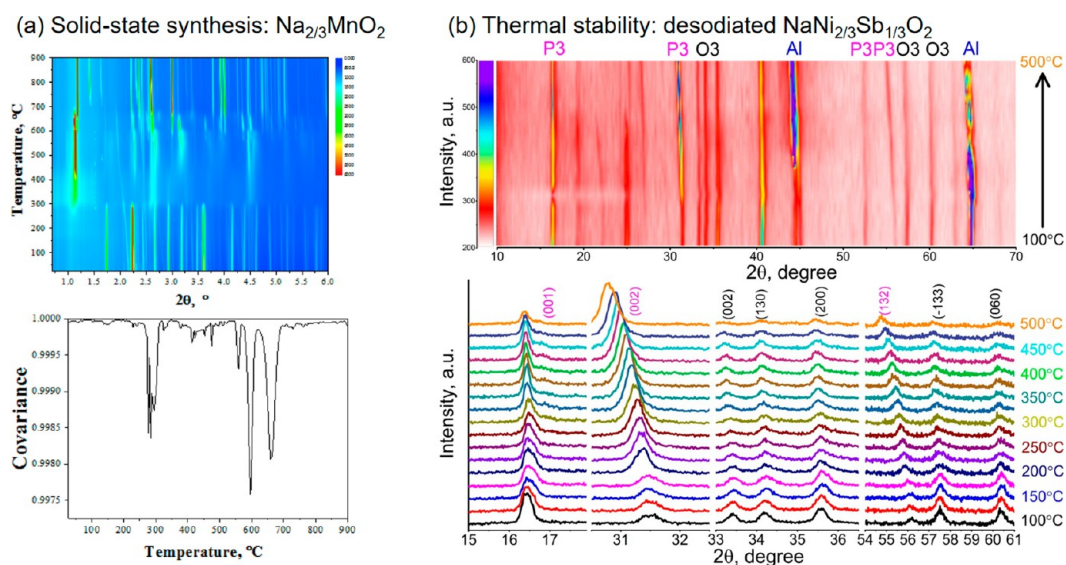
Figure 11. *In situ*/operando XRD investigation during materials synthesis and for thermal stability of electrode materials. (a) Contour plot of *in situ* XRD patterns collected during the solid-state synthesis and corresponding covariance analysis. Reprinted with permission from ref 139. Copyright 2017 Elsevier. (b) Contour plots of high-temperature *in situ* XRD patterns of charged state $Na_xNi_{2/3}Sb_{1/3}O_2$ electrode and corresponding selected diffraction patterns. Reprinted with permission from ref 140. Copyright 2017 Elsevier.

information during the synthesis process of electrode materials. Ma et al.[139] studied the formation mechanism of the P2-type $Na_{2/3}MnO_2$ phase during the solid-state synthesis by *in situ* high-energy XRD. Before sintering, the pristine powder consists of Na_2CO_3, $MnCO_3$, and Mn_3O_4 (Figure 11a). On the basis of the *in situ* XRD results (top panel) and corresponding covariance analysis (bottom panel), the solid-state reaction occurs at two temperature ranges: 270−300 °C and 550−710 °C. Multiple intermediates are formed during the lower temperature range, and the P2-type $Na_{2/3}MnO_2$ phase appears at about 600 °C. At the end of the heating (900 °C), the diffraction peaks of the O′3-type $NaMnO_2$ phase are observed. The findings highlight the importance of elaborate synthesis parameters modulation enabling high-performance cathodes.

In addition, thermal stability is another important aspect to consider in SIB applications. To understand the thermal behaviors, Dai et al.[140] used high-temperature *in situ* XRD to probe structural evolution of the desodiated $NaNi_{2/3}Sb_{1/3}O_2$ electrode as a function of temperature between 100 and 500 °C. The material exhibits no sign of phase transformation or new phase formation, only gradual changes in diffraction peaks to lower 2θ angles during heating processes, indicating that this structure is relatively stable within the high temperature range (Figure 11b). Though thermal runaway issue in SIBs is less severe compared to LIBs, stability in electrode materials under extreme temperatures is still recommended.

Overall, *in situ*/operando (S)XRD technique has been used in various aspects of SIBs, including elucidating electrochemical reaction mechanisms, degradation mechanisms, thermal stability, and the solid-state synthetic process of electrode materials (mostly cathodes). For lab-based XRD, the acquisition rate or the temporal resolution is far inferior to that of high-speed synchrotron-based XRD. Therefore, SXRD is strongly recommended for accurate analysis. Following with elaborate refinements, the information obtained from this technique enables an atomic understanding of the structural evolution. The power of X-ray diffraction is far beyond the

aforementioned applications. In light of better spatial resolution, Bragg coherent diffraction imaging (BCDI) of much smaller beam size is capable of resolving the strain and morphological information for isolated single crystals. For sufficient temporal resolution, ultrafast SXRD can be implemented in the case that the metastable phase cannot be captured, especially for those multi-phasic reactions. Although *in situ*/operando (S)XRD techniques previously designed for LIBs can be readily applied for SIBs, there is still room for improvement from different aspects. For example, to realize interaction between active materials and X-rays, punched hole(s) are often fabricated on *in situ*/operando cells. The hole(s) covering with insulating materials may cause precarious pressure and hamper the electrical connection. As the photon energy is high (transmission mode), if applicable, pouch cell can be performed for *in situ* XRD experiments. In a word, the hardware design of *in situ*/operando configurations should be stabler and more adaptable. As a diffraction-based technique, the intrinsic disadvantage is apparent: it is knotty to address materials of poor crystallinity; therefore, a combination of other techniques that can probe local information and materials' lack of long-range order can provide more comprehensive information, which will be introduced in the following sections.

3. *IN SITU*/OPERANDO XAS

XAS is a synchrotron-associated characterization technique. Unlike XRD, XAS does not require long-range order in materials for characterization—that is, it works equally well in amorphous materials, crystalline solids, and liquids. The basic principle of XAS based on how strongly selected elements within a material absorb X-rays as a function of X-ray energy. This reduction is described by the absorption coefficient according to Beer's law, i.e., $I_t = I_0 e^{-\mu(E)t}$, where $\mu(E)$ is the absorption coefficient that is related to the photon energy, I_t and I_0 represent the intensities of transmitted and incident X-rays, and t is the thickness of the sample.[141] The XAS data analysis usually falls into two regions: the X-ray absorption
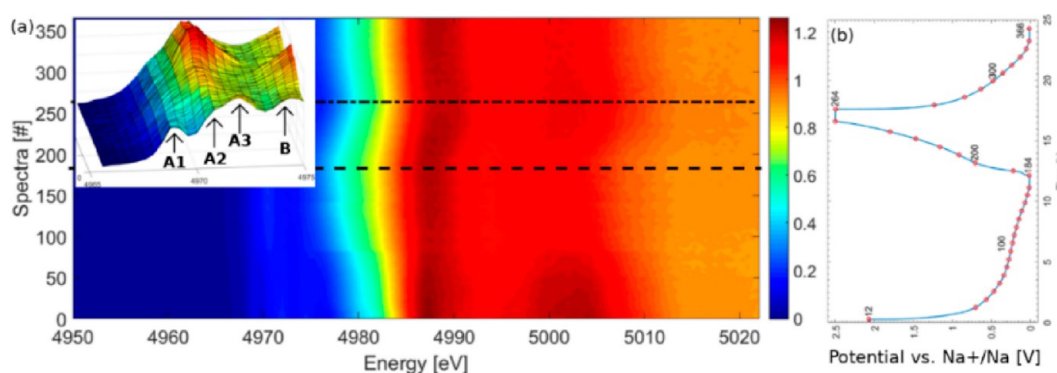
Figure 12. (a) Observation of Ti K-edge XANES of TiO_2 anatase structure. Dashed line and dashed-dotted line present the end of first charge and end of charge positions. The inset panel is the evolution of the pre-edge features. (b) Corresponding electrochemical cycling curves. Reprinted with permission from ref 147. Copyright 2020 MPDI.

near-edge structure (XANES) and the extended X-ray absorption fine structure (EXAFS).[142] The XANES region is located in the range of 5−150 eV from the ionization edge, which displays a sudden jump in the spectrum due to the strong absorption of X-ray. It provides chemical and structural information, such as the oxidation state, orbital occupancy, and symmetry. The EXAFS region comprises the energy range beyond the absorption edge, which reflects local atomic structure. To be more specific, the bond distance, coordination number, and type of neighboring atoms can be known. These two regions are dependent on the incident X-ray energy and the atomic number (Z) of elements; thus, a method called fingerprinting is used to match the XANES spectrum of unknown material to those of foregone species.[143] In addition, XAS is usually divided into hard XAS (hXAS) and soft XAS (sXAS) according to the energy range of the synchrotron X-ray. The hXAS energy is above 5 keV and covers the K-edges of TM elements, while the sXAS energy is between 100 eV and 3 keV and covers the K-edges of light elements (include B, C, N, O, and F) as well as the L-edges of TM elements.[144] There is also an intermediate region (2−7 keV), namely tender X-ray, which can probe the narrow solid−liquid interface but by exploiting photoelectron emission rather than measuring absorption.[145] The following subsections discuss the application of *in situ*/operando hard/soft XAS in the bulk and surface chemistry, especially the charge compensation mechanisms of SIB electrode materials.

3.1. In situ/Operando hXAS. hXAS is a bulk-sensitive technique which can be used in transmission and fluorescence modes. A synchrotron radiation source of high brightness can penetrate materials with proper thickness to probe atoms, molecules, and chemical bonds. For example, in the most commonly used transmission mode, synchrotron light can well probe a homogeneous sample when its total thickness is below 2−3 absorption lengths (the absorption length is proportional to $1/\mu(E)$). In addition, the hXAS does not need an ultra-high-vacuum environment and has short characteristic time (a few seconds to tens of seconds), which is suitable for operando studies of SIBs.

3.1.1. Intercalation Reactions. Most electrochemical reactions involve electron transfers, resulting in the change of oxidation state and sometimes formation of intermediate amorphous phases. Like other *in situ*/operando techniques, *in situ*/operando hXAS has been successfully employed in various SIB systems, which is focused on investigation of the dynamic

charge compensation as well as electronic structure evolution of materials during electrochemical processes.[94,146]

The intercalation reaction mechanism in TiO_2 has been confirmed in LIBs, but the Na storage mechanism in TiO_2 remains controversial. Recently, Fehse et al.[147] revealed that the sodiation of anatase TiO_2 is primarily based on the $Ti^{4+/3+}$ redox and accompanied by an irreversible change of the pristine structure (Figure 12). The sodiation of anatase TiO_2 proceeds through the following reaction mechanisms: upon the first sodiation process, $TiO_2 + xNa → "Na_xTiO_2"$, and during subsequent cycles, $"Na_xTiO_2" ↔ "TiO_2" + "Na_xTiO_2" + Na$, where the quotation marks in the reactions refer to amorphous or disordered phases or both. Siebert et al.[148] further quantified the amount of reversible and irreversible Na ions inserted into a anatase TiO_2 electrode based on an analytical fit and principal component analysis with a linear combination analysis (LCA) of operando XANES data at the Ti K-edge. The irreversible loss of the structural ordering are responsible for the low Coulombic efficiency during the first cycle.

Most TM-based cathode materials of the SIBs also proceed through the intercalation reaction mechanism. In general, TMs are heterovalent elements, which occur in a wide range of formal oxidation states during sodiation/desodiation. In order to restrain the unfavorable phase transformation and stabilize the structure, the multi-TM-cation substitution or doping approach is employed. These TMs with special electronic structures, especially their absorption energy close to each other, are ideal targets for the *in situ*/operando hXAS investigations. In addition, the distribution of elements at multiple crystal sites in TM oxides may influence the batteries performance. The structure fitting and analysis of EXAFS can confirm the coordinated atoms, pertinent bond lengths, and ratio of different atomic occupancies.[149] These crystal site occupancies require local or short-range information that are difficult to be identified by XRD. In combination with *in situ* EXAFS analysis and corresponding electrochemical experiments, the roles of the metal elements at specific crystal sites can be well understood.

The following discussion is restricted to the application of *in situ*/operando hXAS characterization in TM-based cathode materials. The exact valence can be readily calculated from the reference based on the linearity between energy shift and oxidation state. In most reports, Mn remains in the +4 oxidation state in the layered oxides during cycling, showing minor participation in the electrochemical reaction.[150,151] The main function of the Mn in layered oxides is to stabilize the

(a) P2-Na$_{0.78}$Ni$_{0.23}$Mn$_{0.69}$O$_2$
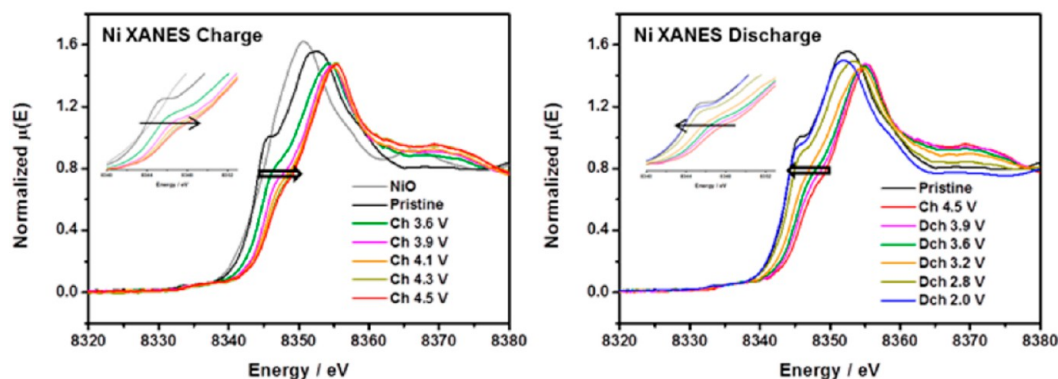
(b) Prussian blue analogue

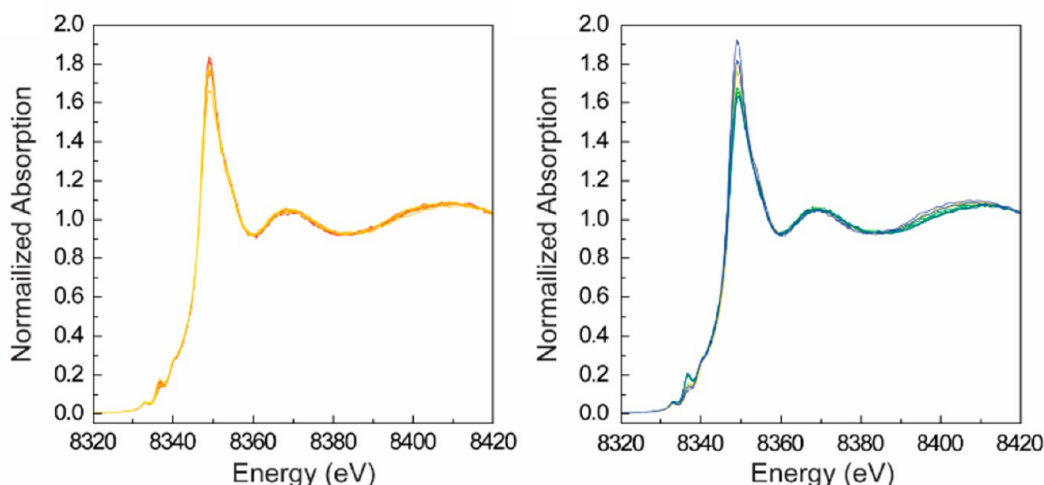**Figure 13.** *In situ*/operando XANES at Ni K-edge XANES of the (a) P2-type Na$_{0.78}$Ni$_{0.23}$Mn$_{0.69}$O$_2$ material. Reprinted with permission from ref 151. Copyright 2017 American Chemical Society. (b) Prussian blue analogue. Reprinted with permission from ref 155. Copyright 2020 American Chemical Society.

host structure, which provides a negligible contribution to the charge compensation. However, some recent studies found that the redox pair of Mn^{4+}/Mn^{3+} involves in the charge compensation process with other TMs, and its activity depends on the cutoff voltage.[152,153] Co exhibits typical redox behaviors as a key contributor to the charge compensation mechanism during Na insertion and extraction. For example, in P2-Na$_{0.74}$CoO$_2$ electrode, the sodium intercalation/deintercalation proceeds with the Co^{3+}/Co^{4+} redox reaction,[154] and the Co^{3+}/Co^{2+} redox pair is involved in the charge compensation process of a P2-Na$_{2/3}$Co$_{2/3}$Mn$_{1/3}$O$_2$ electrode.[152] Ni is also found to be electrochemically active in layered oxide materials but is electrochemically inactive in Prussian blue analogue materials. The Ni^{2+}/Ni^{4+} redox couple is the main charge compensation contributor at the TM sites during Na ions intercalation/deintercalation in a P2-type Na$_{0.78}$Ni$_{0.23}$Mn$_{0.69}$O$_2$ cathode (Figure 13a)[151] but is electrochemically inactive in a Prussian blue material Na$_2$Ni(II)[(Fe(II)CN$_6$)] (no remarkable changes of Ni K-edge position in *operando* XANES data (Figure 13b), indicating that the capacity contribution of Ni is negligible).[155] Ni^{2+}/Ni^{4+} redox couple is active in layered oxides with mixed structures of P2/P3/O3-Na$_x$Mn$_{0.5}$Ni$_{0.3}$Fe$_{0.1}$Mg$_{0.1}$O$_2$ materials.[156] Other Ni redox pairs, such as the Ni$^{2-3}$/Ni^{4+}[150] and the Ni^{3+}/Ni^{4+},[157] were also proved to be active via *in situ*/operando XANES. Likewise, the Fe^{2+}/Fe^{3+} redox reaction is

well established in iron phosphate cathodes,[158] where the cationic/anionic redox reactions in iron-based layered oxides are complex. For instance, the iron-based layered oxides are inactive materials in LIBs but exhibit reversible capacity in SIBs. From the *in situ* and *ex situ* XANES results, the charge compensation of the layered NaFeO$_2$ material occurs through the oxygen redox activity during Na insertion and extraction, rather than through the Fe^{3+}/Fe^{4+} redox reaction.[159] However, it was reported that the Fe^{3+}/Fe^{4+} redox activity is responsible for charge compensation in some layered binary Na$_x$Fe$_y$-TM$_{1-y}$O$_2$ structure[153] and ternary Na$_x$Fe$_y$TM$_z$TM′$_{1-y-z}$O$_2$ compounds.[156,160] The Fe redox and anionic activity can be a future directions for SIB cathodes.

3.1.2. Alloying Reactions. *In situ*/operando *h*XAS is also suitable for tracing alloying reactions. Darwiche et al.[161] used operando *h*XAS to investigate the dynamic behaviors of Sb electrode during the first three cycles (Figure 14a). Despite slight changes in overall shape of the XANES region, the oscillation of EXAFS spectra is notable during different cycling processes due to a low energy resolution of the absorption Sb K-edge. During the first sodiation process, the crystalline Sb gradually turns into a disordered Na$_3$Sb phase accompanying the amorphization of Sb; during the subsequent desodiation process, the Na$_3$Sb phase transforms back to the amorphous Sb rather than pristine crystalline Sb. This amorphous Sb can
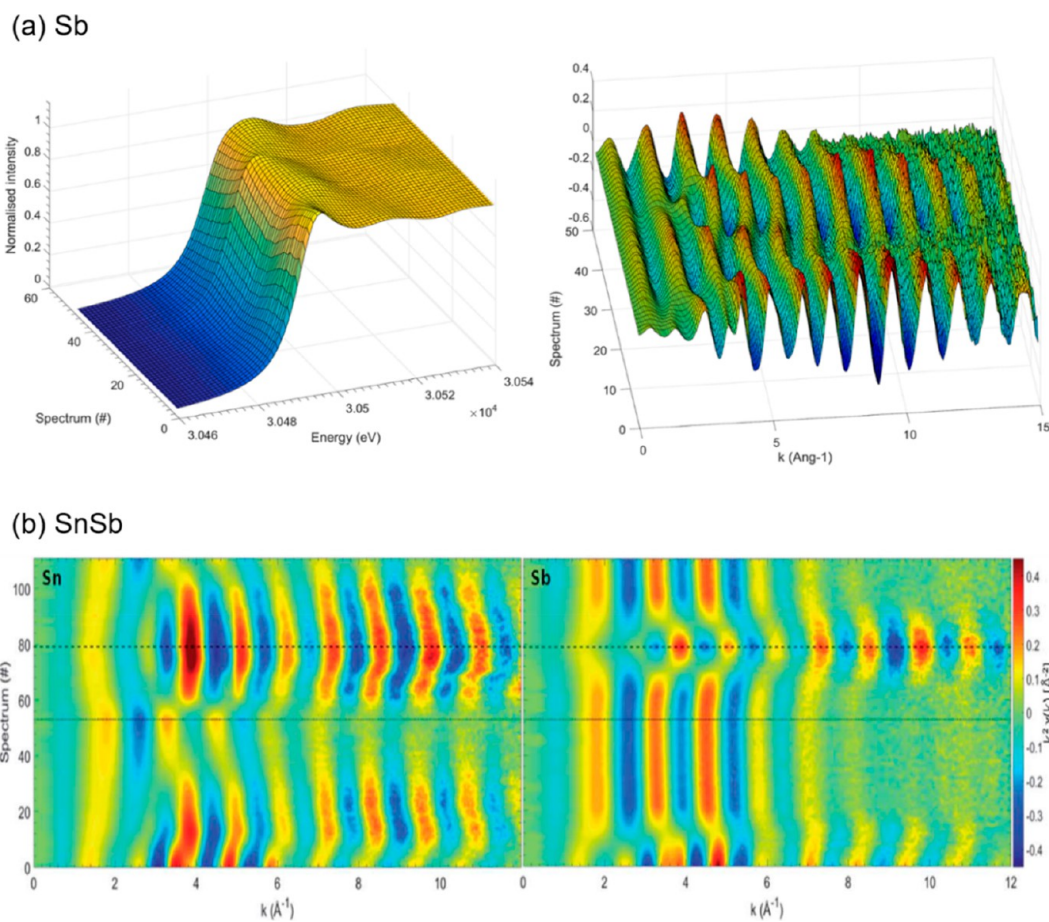
Figure 14. (a) Operando Sb K-edge XANES and EXAFS spectra collected during the first one and a half cycles. Reprinted with permission from ref 161. Copyright 2018 Batteries MDPI. (b) Operando Sn and Sb K-edge EXAFS spectra measured during the first three cycles. Reprinted with permission from ref 162. Copyright 2018 Royal Society of Chemistry.
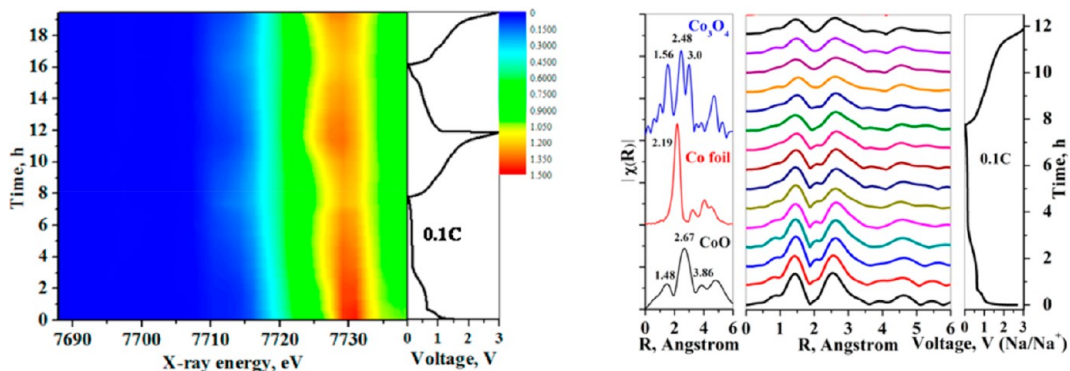

Figure 15. Operando XANES spectra and corresponding EXAFS analysis along with discharge/charge profiles of porous cobalt oxide electrode. Reprinted with permission from ref 167.

reversibly transform into Na_3Sb phase in the second sodiation process. In addition, the model-based EXAFS analysis can be further used to detect the reaction kinetics in bimetallic electrodes. Fehse et al.[162] investigated binary SnSb electrode with Sn and Sb K-edges during cycling. From the evolution of EXAFS spectra during sodiation process (Figure 14b), the changes of Sn and Sb do not occur synchronously, suggesting a complex multi-step alloying reaction process: (1) the sodiation of Sb first occur—the Sb in the pristine SnSb phase transforms to the Na_3Sb phase and an unstable intermediate phase of nanosized metallic Sn (α-Sn); (2) as the reaction continues,

the Sn gradually transforms to $Na_{15}Sn_4$ phase. Furthermore, EXAFS fingerprints demonstrate that the amorphous SnSb generate after a complete cycle is different from the pristine SnSb phase.

3.1.3. Conversion Reactions. As mentioned above, degradation mechanisms of conversion-type electrode materials are generally arising from the irreversible phase transformations, volume change, and reaction kinetics. The effects of phase transformation and volume change have been demonstrated in various *in situ*/operando XRD and *in situ* TEM studies. The coupling of *in situ*/operando XAS is helpful
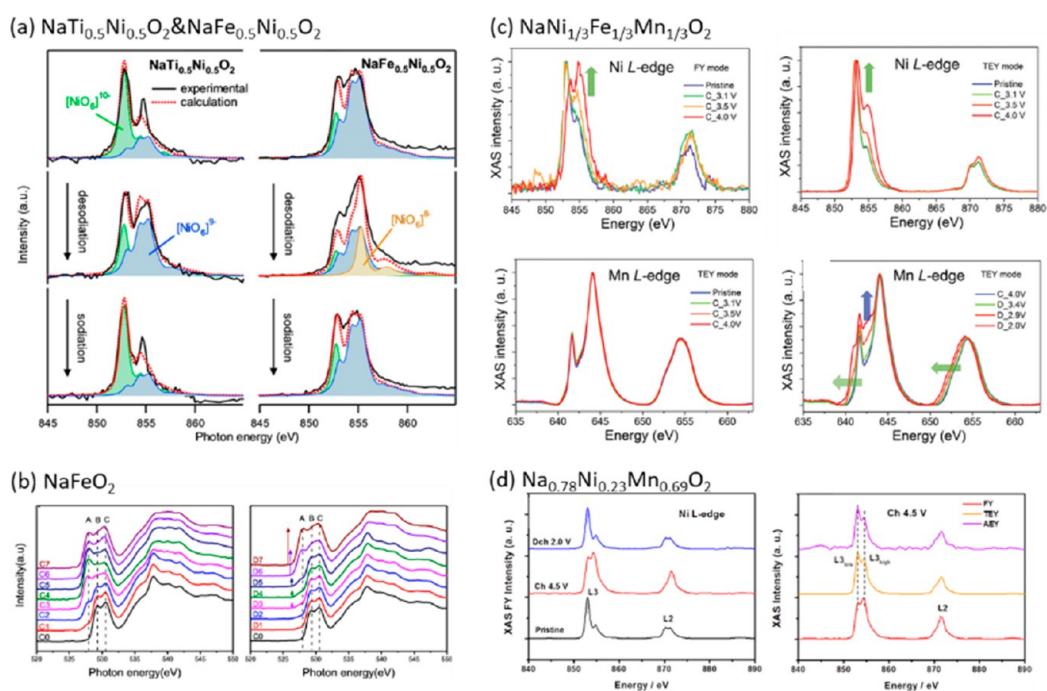
Figure 16. (a) Ni L-edge of $NaTi_{0.5}Ni_{0.5}O_2$ and $NaFe_{0.5}Ni_{0.5}O_2$ at different charged/discharged states in PFY mode. Linear combination was applied based on calculated patterns. Reprinted with permission from ref 175. Copyright 2016 American Chemical Society. (b) O K-edge O3-$NaFeO_2$ at different charged/discharged states in TFY mode. C0-C7 means charging from 2.5 to 4.5 V continuously. D7-D1 is the reverse process. Adapted with permission from ref 159. (c) Mn and Ni L-edge of $NaNi_{1/3}Fe_{1/3}Mn_{1/3}O_2$ at different charged (C)/discharged (D) states. Ni was performed in total electron yield and fluorescence yield mode while Mn was under total electron yield mode. Reprinted with permission from ref 189. Copyright 2018 Wiley. (d) L-edge of Ni for $Na_{0.78}Ni_{0.23}Mn_{0.69}O_2$. Adapted with permission from ref 195.

in reflecting the electronic structure information on the bulk of electrodes in real cells with conventional liquid electrolytes, providing a quantitative assessment of reaction kinetics in various conversion-type materials, such as crystallography-dependent kinetics[163,164] and morphology-dependent kinetics.[165,166] For instance, combined with operando XAFS, XRD, and small-angle X-ray scattering analysis, Xu et al.[167] shed light on the structural evolution of porous cobalt oxide materials (composed of two phases: Co_3O_4 and CoO) during sodiation. As shown in Figure 15, no evident changes are observed during the first and second sodiation cycles, from either crystal structure changes in EXAFS or valence states evolution in XANES analysis, which is attributed to the sluggish transportation of Na ions into the bulk material hindered by the large radius of Na ion and the intrinsic large sodiation barrier of cobalt oxides.[168] Therefore, a large anion framework is required to boost Na diffusion and conversion reaction kinetics, such as replacing metal oxides with metal sulfides. It has been proved that cobalt sulfides exhibit greater electrochemical activities than that of cobalt oxides (the Co reduction from $Co^{+1.78}$ to Co^0 was evidenced by in situ XANES of Co_9S_8).[169]

Overall, in situ/operando hXAS techniques provide opportunities to describe the local structural changes in battery materials during continuous cycling, such as charge transfer and changes in bond length and local coordination environment. However, this technique is insensitive to light elements due to the energy limit. Being an element-sensitive characterization, information on long-range order is unavailable. Therefore, a combination of the electrochemical and other complementary characterizations is crucial to more comprehensive understandings regarding the complex phenomena that

emerge during SIB operation with different aspects of physical/chemical changes and at multiple length scales. In the in situ experiments, due to the auxiliary cell components, the transmission mode sometimes cannot offer sufficient signal as the X-ray energy is not as high as that in XRD. The fluorescence signal can be also problematic, dependent on the hole size, sensitivity of detector, and the self-absorption effect. For EXAFS-needed measurements, as the acquisition time is 10−20 min, depending on different k ranges, a hold at certain voltage must be applied for the materials.

3.2. sXAS for Surface Studies. sXAS is a sensitive spectroscopic technique resolving electronic structure from subsurface to surface, using synchrotron X-ray energy from 100 eV to 2 keV (no absolute boundary is set, 3 keV is also proposed as the upper limit).[170] Similar to hXAS, sXAS is an element-specific characterization that can be combined with XRD, TEM, etc. While both probing unoccupied states, sXAS for TM delineates a 2s-3d transition (L-edge), unlike the 1s-4p transition as K-edge in hXAS. Therefore, sXAS can provide direct and precise interpretation for the oxidation state and spin state of TM, the building blocks for numerous SIBs electrodes. Anchored by lower energy of incident photon, besides L-edge of TM, K-edge (1s-2p transition) of low-Z elements such as Na, C, N, and O can be readily covered. Overall, capable of resolving light elements (K-edge), anodes free of TM can be investigated, from carbon families to multiple alloy-type and conversion-type materials. Specifically in oxides, pre-edge of O K-edge symbolizing the hybridization effect between O 2p and TM 3d orbitals can provide useful information, in combination with the valence change of other elements in electrodes.[171] In addition, chemical environments can be resolved in sXAS, from the surface (down to 1 nm) to

the subsurface (around 100 nm). To realize this function, either fluorescence or electron signal is detected, originating from distinct relaxation processes.[172] The former includes total fluorescence yield (TFY), partial fluorescence yield (PFY), and inverse partial fluorescence yield (iPFY), whereas the latter consists of total electron yield (TEY), partial electron yield (PEY), and Auger electron yield (AEY). The TFY mode is subsurface-sensitive with a probing depth of 50−100 nm depending on the sample.[173] However, it usually suffers from self-absorption and saturation effects, which is minimized by iPFY. In contrast, TEY mode probes a depth of a few nanometers and partial electron yield is even more shallow, attributed to the limited escaping depth for electrons compared to photons depending on mean free path.[174] Generally, TFY and TEY are popular detection modes for SIBs research in the past decade while the most surface-sensitive AEY is less. The instrumentation of operation modes can be checked in several reviews, which is not the focus here.[170,172]

To the best of our knowledge, there has not been a comprehensive employment of *in situ*/operando *s*XAS in SIBs. These can be attributed to three reasons: (1) Soft X-ray is of lower energy compared to hard X-rays, limiting the penetration depths that forbids signal detection. (2) It requires ultrahigh vacuum that can be hardly achieved as batteries normally involves volatile liquid electrolytes. (3) *In situ*/operando experimental setup is challenging to construct. The first one can be viewed as the fundamental reason that hampers the pertinent feasibility. Therefore, we will introduce the *ex situ* *s*XAS studies in the following subsections.

3.2.1. Intercalation Reactions. *s*XAS has been widely applied to investigate cathode materials based on the intercalation mechanism. Because of its sensitivity to the surface electronic structure, *s*XAS can provide critical information about charge compensation and surface degradation mechanisms.

Most oxide-based cathode materials consist of multiple TM elements, with each of them performing certain functions during battery cycling. The elemental specificity of *s*XAS allows for pinpointing the roles of each element without interferences from other elements. For example, *s*XAS can be highly useful to specify the capacity contributions from distinct redox species at different voltages, which is complementary to *h*XAS and provides surface redox states. Layered cathodes are endowed by compositional flexibility where tuning the substituents can modulate the redox reactions and voltage profile. In O3-type $NaFe_{0.5}Ni_{0.5}O_2$ and $NaTi_{0.5}Ni_{0.5}O_2$, Nanba et al. obtained O K-edge and Ni L-edge in PFY mode.[175] A so-called redox potential paradox was unveiled: the latter with Ni^{2+}/Ni^{3+} redox pair delivers higher potential than the former relying on Ni^{3+}/Ni^{4+}. As shown in Figure 16a, the Ni L-edge in original $NaTi_{0.5}Ni_{0.5}O_2$ displays a major peak at ~852.8 eV, corresponding to high-spin Ni^{2+} that is oxidized to Ni^{3+} in the desodiation process. Differently, Ni L-edge of $NaFe_{0.5}Ni_{0.5}O_2$ shifts toward higher energy, indicating Ni^{4+} formation. Here, the standard curves are theoretical calculation results of $[NiO_6]^{n-}$ clusters based on different Ni oxidation states. The linear combination of *s*XAS L-edge spectra provides quantitate analysis toward charge compensation at various states of charge. After deconvolution, $[NiO_6]^{9-}$ is divided into two portions, 37% $Ni^{2+}O_5{}^{2-}O^-$ and 60% ground-state $Ni^{3+}O_6{}^{2-}$.[176] Besides the unambiguous clarification of reaction extent and electronic states for TM, for some SIBs electrodes,

i.e., Prussian blue analogs, *s*XAS can shed light on the influence of coordination environments on redox reactions.[177,178]

In addition to conventional cationic redox, the anionic redox, i.e., oxygen redox, can be a major contribution at high voltage to elevate the energy density. However, materials of oxygen redox face grand challenges including O_2 evolution, irreversible structural change, large voltage hysteresis, and voltage decay. *s*XAS can substantiate the existence of oxygen redox via O K-edge. The pre-edge intensity is normally assigned to the hybridization effect of O 2p and TM 3d orbitals, reflecting the hole state distribution and the effective charge on the oxygen atom. Among diverse anionic active cathodes, O3-$NaFeO_2$ is a well-studied material.[159,179] Exhibited in Figure 16b, pre-edge peaks are denoted as A, B, and C. Peak A becomes striking upon sodium extraction, signifying the removal of electron density from O atoms, considering that Fe L-edge is free of change at high-voltage range. More specifically, peak A is on behalf of ligand hole-that is, an electronic structure of 3d5L for Fe^{4+}. Though the oxygen redox seemed to be highly reversible, as peak A disappeared continuously during the discharge process, the anionic activity triggered the surface Fe_3O_4 formation hampering sodium diffusion and thus inducing degradation. Other investigations using *s*XAS related to anionic redox incorporates P2-type $Na_{0.78}Co_{1/2}Mn_{1/3}Ni_{1/6}O_2$,[180−182] $Na_{0.67}[Li_{0.21}Mn_{0.59}Ti_{0.2}]$-$O_2$,[183] $Na_{0.72}[Li_{0.24}Mn_{0.76}]O_2$,[184] P3-$Na_{0.6}[Li_{0.2}Mn_{0.8}]O_2$,[185] and disordered rock-salt $Na_{1.3}Nb_{0.3}Mn_{0.4}O_2$.[186] These researches made similar arguments on accounts of intensity change in the pre-edge region. However, in recent years, Yang et al. proposed that the line shape, peak position, and peak intensity can all be attributed to TM characters.[187] Hence, *s*XAS might not be a direct characterization for O anionic redox.

Taking advantage of various detection modes, the inhomogeneity of electronic structure can be discerned in the intercalation-based electrodes, facilitating insights into depth-dependent reaction dynamics.[188] The fundamental interfacial chemistry for cathodes at various operating conditions can be anticipated to help design better materials. For example, Mu et al. used *s*XAS to uncover the surface evolution of electronic structure in O3-$NaNi_{1/3}Fe_{1/3}Mn_{1/3}O_2$ at different SOCs (Figure 16c).[189] It was confirmed that Ni and Mn encountered distinct oxidation and reduction degrees from surface to subsurface. For both TEY and TFY modes, Ni is oxidized and reduced during desodiation and sodiation, respectively. The change in the TEY mode is less than that of the TFY mode, which means reduced Ni species at the surface regardless of the bulk electrochemical oxidized Ni. In contrast, in the charging process and partial discharging process (>2.9 V), the Mn valence remains +4. Interestingly, it was unambiguous that the Mn L-edge shifts toward lower energy with decreased discharge voltage (<2.9 V), symbolizing the formation of Mn^{2+} and Mn^{3+}. The reduction is attributed to the surface reconstruction. After 20 cycles, the surface Mn is reduced to a lower oxidation state, partially responsible for the low Coulombic efficiency at the beginning cycles. Like O3-$NaNi_{1/3}Fe_{1/3}Mn_{1/3}O_2$, a slight reduction of Mn^{4+} at the surface was widely captured in many layered cathodes by TEY mode though Mn species are almost inactive in the bulk.[180−182] Obviously, such surface reduction is not trivial during long-term cycling, especially for materials entirely based on Mn. *s*XAS clarified the fading mechanism of tunnel-type $Na_{0.44}MnO_2$, where increased surface Mn^{3+} and Mn^{2+} were
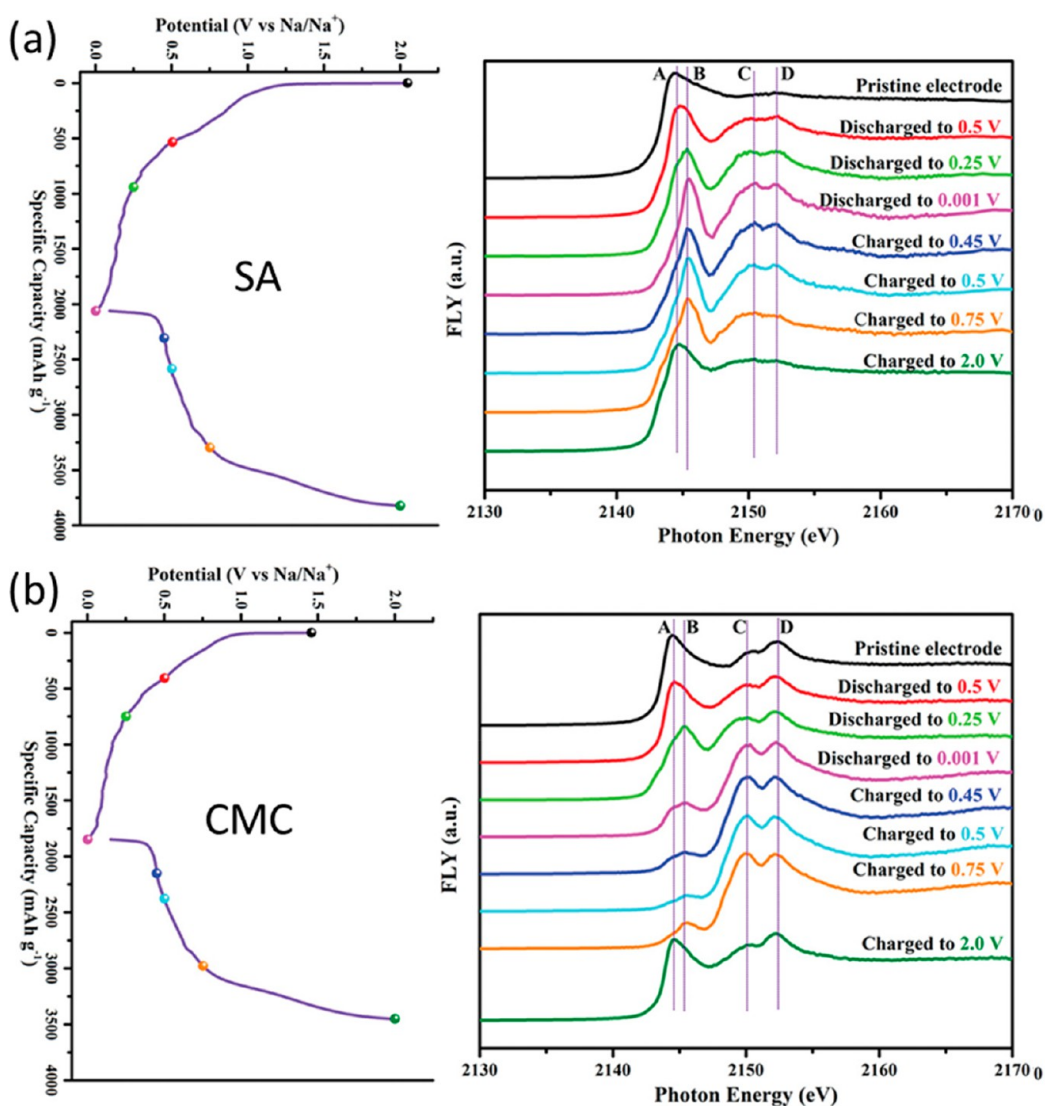
Figure 17. P K-edge of (a) sodium alginate-SA and (b) sodium carboxymethyl cellulose-CMC binders in electrodes at different charged/discharged states (left). Total fluorescence yield mode is applied. Reprinted with permission from ref 200. Copyright 2020 Wiley.

detected.[190,191] The gradient valence distribution for multiple other TM was reported, in which Ni manifests remarkable difference at distinct depths, such as $Na_{1-x}Ni_{2/3}Sb_{1/3}O_2$,[192] $Na_{0.78}Co_{1/2}Mn_{1/3}Ni_{1/6}O_2$,[193] and $Na_{2/3}Ni_{1/3}Mn_{2/3}O_2$.[194] This unique phenomenon can also be due to the catalytic effect of high-valence TM inducing self-discharge and Na migration from the subsurface to the surface.[171,174] Apart from TEY and TFY, the most surface-sensitive AEY mode can help systematically examine the gradient valence distribution, for example, in $Na_{0.78}Ni_{0.23}Mn_{0.69}O_2$ (Figure 16d).[195] The valence of Ni on average is nearly +4 in the fully charged state, while a decrease in the valence from subsurface to surface to top-surface can be discerned. The problem of the Auger electron utilization is the coverage and interference of cathode−electrolyte interface (CEI). It can be also facilely replaced by another more common surface-sensitive technique, X-ray photoelectron spectroscopy (XPS). These might be the reasons that AEY is much less often employed in the sXAS compared to other modes.

As noted above, sXAS delineates TM valence from subsurface to surface in the cathode, paving a foundation for further rational material design. Among various modification

routes, surface coating is an effective approach to stabilize cathodes.[196] Mu and co-workers designed conformal coating onto the aforementioned $NaNi_{1/3}Fe_{1/3}Mn_{1/3}O_2$ cathode.[197] Comparing spectra from TEY and TFY modes, Fe and Ni are without notable difference while surface Mn is reduced judging from the enhanced intensity of low-energy shoulder. Endowed by the reduced oxidation state of surface (tailored with Mn^{2+} and Mn^{3+}) and organic embedment, the interface instability was mitigated. In addition to coating, doping is an alternative for improving cyclability. Xu and co-workers introduced electrochemically inert Cu into the Fe/Mn-based layered oxide to alleviate Fe migration and suppress voltage decay, confirmed by TEY and TFY modes.[198] Effects of Li-doping toward surface chemistry also received attention.[199] Especially for the O3-type $Na(Ni_xFe_yMn_z)O_2$, Li-substitution contributes to the mixed phase (layered + spinel) with superb connectivity, ameliorating the ion diffusion and structural reversibility.[181] As a result, the Ni redox couple is highly reversible based on the Ni L-edge. In conclusion, sXAS can greatly accelerate the fundamental understanding of the cathode materials as well as provide guidelines/proofs for enhancing structural stability or energy density.
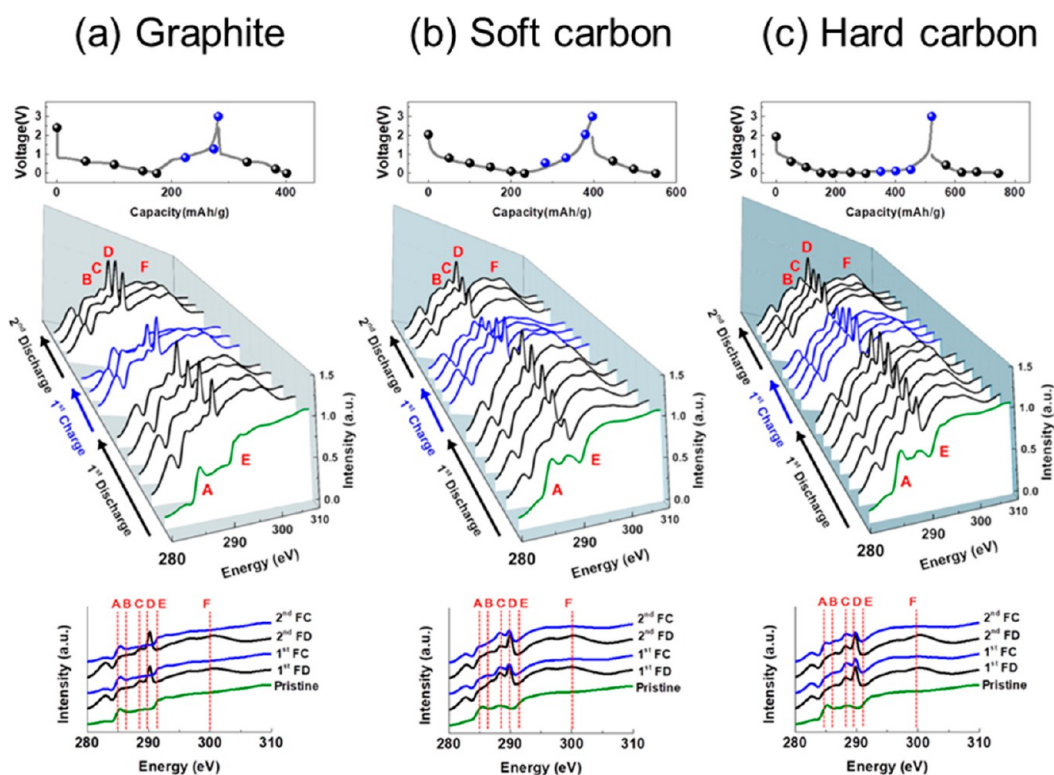
Figure 18. K-edge of C under total electron yield mode for cycled (a) graphite, (b) soft carbon, and (c) hard carbon anodes. Graphite is operated in ether-based electrolytes, and the others are in carbonate-based electrolytes. Reprinted with permission from ref 204. Copyright 2018 American Chemical Society.

3.2.2. Conversion Reactions. In addition to the considerable exploitation of *s*XAS in analyzing multi-scale and multi-component TM-based intercalation electrodes, capable of resolving light elements (K-edge), electrodes free of TM are investigated, from carbon families to broad alloy-type and conversion-type electrodes. For conversion-type electrodes, the surface phase and interphase layers govern the structural reversibility and side reaction with electrolytes. In recent work, Sun and co-workers used *s*XAS to study the interfacial compatibility of P anode upon sodiation/desodiation with different binders.[200,201] Rational choice of binder is discovered to activate phosphorus particles at various contents (Figure 17). Peak A represents the original P−P bonding, while peak B symbolizes the P−Na bonding in Na$_x$P. The difference is that the sodium alginate-based electrode demonstrated a sharp B peak at 2145.5 eV, implying more Na−P bonding in accordance with slightly higher capacity. C and D denote the P−O bonding useful in the interface analysis—that is, $(PO_2)^{3-}$ species and $(PO_4)^{3-}$ species, respectively. In both electrodes the C and D peaks are more visible upon discharge process, indicative of the side reactions between Na$_x$P and electrolytes in the first cycle. Apparently, C and D evolve and fade away, on behalf of the reversible decomposition/dissolution of surface P−O species. This case suggests that *s*XAS can also advance the understanding of active materials interacting with other auxiliary components within the electrodes. This is essential for materials of large volume expansion that normally suffer from interface instability and poor cyclability.

3.2.3. SEI Properties. Given the capability to inspect top-surface chemical information, *s*XAS has potential to illuminate complicated SEI properties. This has been realized concurrently when uncovering storage mechanism in the subsur-

face. Historically, dating back to the 2000s, *s*XAS had been employed to investigate the SEI and CEI for LIBs.[202,203] However, to the best of our knowledge, only one work used the technique to specifically explore the composition and stability of SEI in SIBs. Kim and co-workers collected C K-edge spectra in ether-based electrolytes for graphite and carbonate-based electrolytes for hard carbon/soft carbon (Figure 18).[204] Peaks B, C, D, and F are interpreted as Na$_2$CO$_3$ and some other complex organic sodium salts. The intensity change represents the disappearance and re-development of SEI. It is pinpointed that recovery to pristine interface (charged to 3.0 V) happened merely in the graphite−ether system, consistent with the earlier results obtained via XPS.[205] Peaks A and E as fingerprints of pristine carbon families could not be seen in both disordered carbon, implying much thicker SEI in carbonates beyond the TEY probing limit.[206] To conclude, the non-destructive *s*XAS can minimize the degradation of SEI layer, in which the depth-profiling of components in the complex multi-layer structure could be better completed.[207,208] Furthermore, the effect of crystal orientation on SEI nature can be readily investigated.[209] For the hard carbon of preeminent practical value, the film-forming effect during long cycling can be more focused in the ester-based electrolytes, which tends to induce thicker SEI and noticeable degradation.

To summarize, *s*XAS steadily gains prominence in SIBs during the past decade. Compared to hXAS, *s*XAS can offer more detailed electronic states and, importantly, the depth sensitivity. *s*XAS can also be a support but perhaps not direct evidence of oxygen activity. Given the insufficient energy density and cycling performance of SIBs, limitless opportunities are still available for *s*XAS for the purpose of

elucidating diverse charge compensation mechanisms, gradient valence distribution, reversibility of redox pair, water stability of cathodes, SEI components, etc.[210] Here we only exemplify the principles and capability of sXAS. In the current stage, all the characterizations were ex $situ$, and conceivably in the future in $situ$/operando studies may be initiated for SIBs, which has been seen in other fields.[211−213] One conceivable problem would be the representativeness of the spectra-that is, i.e., the signal comes from limited materials (several hundred nm at most) because of low X-ray energy. Close to current collector or separator, the local state of charge and element valence may be distinct.

4. IN SITU/OPERANDO X-RAY SPECTROSCOPIC IMAGING AND TOMOGRAPHY

In the past few years, X-ray imaging and tomography have been better developed to empower the visualization of chemical and morphological information for battery materials, mainly including X-ray computed tomography (CT), transmission X-ray microscopy (TXM), scanning transmission X-ray microscopy (STXM), and X-ray fluorescence microscopy (XFM).[214,215] Being complementary to other characterizations such as XRD, hXAS, these imaging and tomography characterizations capture the localized information rather than bulk information at different spatial resolution. Hence, the impacts of material heterogeneities on electrochemical performances can be unraveled. Principles for aforementioned different techniques are summarized in several reviews.[215−217] Among various imaging methods, in SIBs the most popular one is TXM (or full-filled TXM) using hard X-ray, excelling in resolving the electronic state and distribution of TM with a nominal resolution of ∼30 nm.[214] The three-dimensional (3D) chemical map can be reconstructed from projection images of individual particle collected at different angles, which is advantageous to discern the charge and compositional inhomogeneity of pristine materials as well as impacts of electrochemical cycling. STXM employs soft X-ray to potentially provide even better resolution down to ∼12 nm.[214,217] XFM is of the lowest resolution (sub-micrometer) but achieving ppm scale differentiation. Therefore, XFM is suitable for probing dissolving species from electrodes. The above imaging approaches are implemented with synchrotron light sources, while X-ray CT can be readily accessible by lab-based instruments. X-ray micro-CT is able to assess the macroscale morphological parameters including surface area, porosity, and tortuosity though the resolution cannot be comparable to that of TXM.[215] Endowed with the non-destructive nature of hard X-ray and no requirement for vacuum environment, TXM and CT are suitable for in $situ$/operando experiments. On the contrary, STXM utilizing low-energy soft X-rays could be for in situ/operando experiments. In summary, spatial chemical mapping of TM and morphological parameters can be beneficial to elucidate the mechanism of irreversible capacity, localized over-discharge/over-charge, and gas generation, causing safety issues.[218] The following discussion majorly focus on in $situ$/operando experiments, especially TXM, whereas ex $situ$ measurements will also be reviewed.

4.1. Intercalation Reactions. X-ray based imaging techniques (i.e., TXM-XANES) under in $situ$/operando conditions excel in probing the charge heterogeneity that is normally reported to negatively affect the cathode electrochemical behaviors by changing electronic properties and ion diffusion.[188] The in $situ$/operando measurement can specifically study fixed individual particles and particle agglomerates, which cannot be realized by ex $situ$ experiments. For higher capacity, a broad voltage window can be deployed while the influence on phase transformation and charge inhomogeneity should be scrutinized. Xie and co-workers used operando TXM to support the formation of a non-equilibrium solid-solution phase of intercalation-based $NaNi_{1/3}Fe_{1/3}Mn_{1/3}O_2$ cathode at high SOC (Figure 19).[219] XRD and TEM recorded the
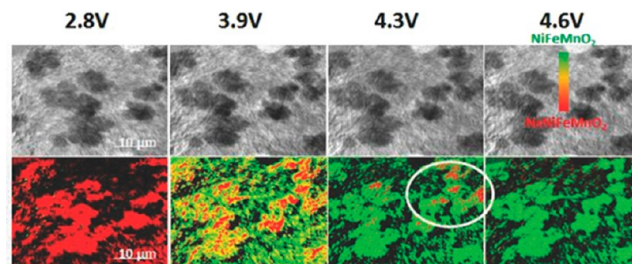

Figure 19. Reconstructed images of $NaNi_{1/3}Fe_{1/3}Mn_{1/3}O_2$ cathode at different states of charge derived from operando TXM. Reprinted with permission from ref 219. Copyright 2016 Wiley.

existence of the O3′ and P3′ monoclinic phase from 4.0 to 4.3 V. On the basis of 2D chemical map, from 2.8 to 4.6 V increased sodium extracted from the lattice finally resulted in $Ni_{1/3}Fe_{1/3}Mn_{1/3}O_2$ (green). When the voltage is higher than 3.9 V, Na-deficient $Na_{1-x}Ni_{1/3}Fe_{1/3}Mn_{1/3}O_2$ exists as substitutional solid solution. Even charging to 4.3 V unreacted core can be found in some particles (white circle). From 4.0 to 4.3 V, it is seen that Ni^{3+}/Ni^{4+} and Fe^{3+}/Fe^{4+} are dominating redox species of desired reversibility. Such depth dependent and SOC-dependent phase segregation were also reported in the $NaNiO_2$.[220] The inhomogeneity can be manifested by the "core-shell" structure. Over 4.0 V, the layered Na_xNiO_2 partially transforms into inactive phase due to severe lattice distortion, calling for cation-doping methods to improve structural reversibility.

4.2. Alloy Reactions. Besides chemical and compositional information, another important aspect of battery material is the geometric dynamics, including volume change, specific surface area, porosity, etc. These parameters determining long-term cycling are important for alloy-type materials which intrinsically uptake large amount of Na^+, inducing drastic morphological variation. As such, early in 2015, in $situ$ TXM has been applied for visualizing alloy reaction in SIBs. Sn was chosen since it possesses impressively better cyclability compared to Li counterparts even though the reaction mechanism is identical.[221] It is found out that the volume change of Sn particles is notable during the initial cycle, but microstructural integrity is still maintained in the following cycles without pulverization, in line with superior cycling performance (Figure 20a). The volume expansion in the first sodiation is ∼326%, while the later values are steadily less than 30%. Likewise, the specific surface area remains stable after the first cycle. To achieve some general design principles for alloy-type materials, the authors obtained 3D images for three particles of distinct sizes: 0.5 μm is proposed as a critical value for fully maintaining the microstructural stability without cracks (Figure 20b). As few particles are demonstrated here, it should be pointed out that statistic analysis of more particles
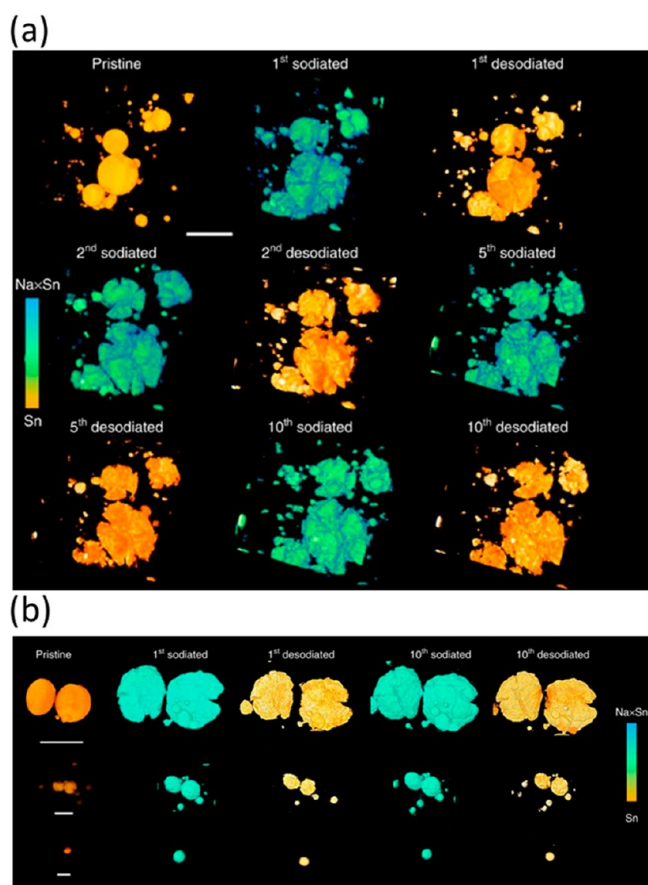
Figure 20. (a) 3D reconstructed images from *in situ* synchrotron hard X-ray nanotomography for tin anode during the first 10 sodiation−desodiation cycles. Scale bar, 10 μm. (b) Comparison of volume change of three particles of distinct size after the 1st cycle and the 10th cycle. Scale bars: 10, 2, and 1 μm. Reprinted with permission from ref 221. Copyright 2015 Springer Nature.

can tremendously enhance the representativeness of the results.

4.3. Conversion Reactions. For conversion-type electrodes, the particle-level charge and phase heterogeneity also occur, which can be more influential than that of intercalation-based materials. Multiple phases co-exist in the cycled conversion-type electrodes, with nanosized TM anchored on Na_2O matrix. These *in situ* formed hierarchical nanocomposite structure has tremendous influence on the battery performances. For example, in NiO anode, exterior Na_2O reaction

layer was proposed to hamper sodium insertion to the core NiO, decorated with reduced Ni nanoparticles by reconstructed visualization.[222] This hints that the utilization is a challenge because of sluggish sodium diffusion kinetics in Na_2O. Recently, Yu et al. utilized *in situ* TXM to discover unreacted core in CuO for the purpose of explaining undesired capacity loss.[223] Figure 21 demonstrates that even discharged to 0.01 V the CuO is still notable. Meanwhile, the shell (Cu +Na_2O) cannot recover to pristine state, in agreement with the low Coulombic efficiency in the first cycle. The core−shell microstructure can be separated and sliced layer by layer in a 3D reconstruction, where the depth-dependent phase can be directly seen. The slow kinetics and large irreversible capacity issues were also observed in NiS and FeS by operando 2D TXM and 3D nano-tomography[224,225] To resolve the utilization issue, the author synthesized CuO of nanosheet primary structure instead of bulk structure. Related 3D hierarchical structure design strategy can be promoted to Fe_3S_4 composed of 2D nanosheet building block.[226] Hence, we can conclude that the *in situ*/operando TXM can facilitate the rational design of conversion-type electrode for improved cyclability. Beside the morphological nanoengineering, the intrinsic sluggish ion transport through the interface in the two-phase reaction process is needed for better understood. For another classical conversion-based P anode, operando X-ray CT based on diffraction was reported, but with inferior resolution.[227] Overall, though it is supposed that the conversion-type anodes are far from practical applications, fundamental investigations can be initiated via time-resolved fully filled TXM to grasp the irreversible capacity and sodiation/desodiation kinetics.

Like any *in situ* experiments, the necessity of exploiting *in situ*/operando X-ray tomography should be examined. Here we present some thoughts toward TXM, XFM, and CT. *In situ*/operando TXM is highly desired for materials (normally based on multi-phasic reactions) displaying rapid and significant phase segregation during relaxation via interparticle and intraparticle diffusion. Uniquely, sodium insertion/extraction pathway and contribution of redox species at different voltage range within one particle can be temporally tracked that is hard to be completed via *ex situ* measurements. It should be noted that as 3D TXM requires long acquisition time, *in situ* measurements can be applied in the 2D mode while 3D analysis can be complementary through *ex situ* samples. Regarding XFM, it is especially suitable for *in situ* measurements in aqueous system: perpendicular to the electrode surface, the spatial gradient distribution of dissolved TM ions
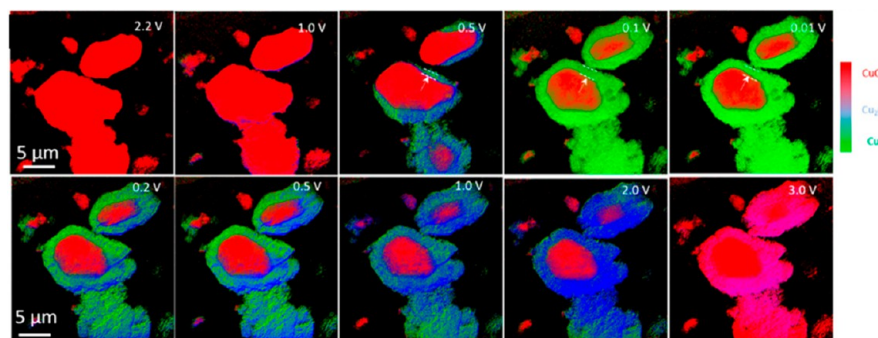

Figure 21. Reconstructed 2D chemical mapping images of CuO intercalated with sodium ions from *in situ* TXM. Reprinted with permission from ref 223. Copyright 2019 American Chemical Society.

at the electrochemical interface can be imaged from tens of micrometers to hundreds of nanometers resolution. As synchrotron resources are limited, *in situ* experiments using lab-based X-ray micro-CT and nano-CT can be more deployed, especially for long-term cycled products. The features of CT should be the large field of view and versatile targets: besides the active phase and inactive phase of material, binder, current collector, etc. can also be analyzed, mostly related to the fading mechanism correlated to electrochemical performances.

In short, taking advantage of multiple virtues, X-ray tomography can be flexible in microscopic and macroscopic levels for SIBs, including spatial distribution of elements, local SOC, dendrite formation, TM dissolution, and morphological parameters, enormously facilitating holistic comprehension of the structure−property−performance relationships in SIBs. Specifically, the material inhomogeneity as well as its relationship with electrochemical performance at different length scales can be better understood. What's more, employing complementary tomography techniques is essential: *in situ*/operando TXM/X-ray nanotomography can provide localized information, corroborating the results from bulk structural characterization, i.e., *in situ* hXAS and *in situ* XRD. Last but not least, as hard X-ray imaging does not require ultrahigh vacuum and easily penetrates the sample, *in situ*/operando experiments can be designed for achieving time-resolved multi-scale chemical and structural information. This means the SIBs can be desirably analyzed at the application level using pouch cells and cylinder cells. In summary, various cutting-edge X-ray based imaging and tomography techniques under *in situ*/operando conditions can be much more exploited to accelerate the development and evaluation of SIBs.

5. *IN SITU*/OPERANDO PDF

Like conventional (S)XRD, the pair-distribution-function (PDF) is also an elastic scattering technique. The powder diffraction data for PDF analysis can be obtained from synchrotron-based X-ray and pulsed neutron sources.[228] The

PDF is used to extract local structural information no matter the samples is solid or liquid, amorphous or crystalline, microscopic or nanoscale materials. Identification of phases

> Techniques based on electron and X-ray methods are complementary on spatial and temporal scales, and it is important to combine different techniques to understand the complex material chemistry in a dynamic system.

and phase fractions as well as stoichiometry can be achieved, similar to Rietveld refinement.[229] The PDF, $G(r)$, is normally derived via a Fourier transform of the total scattering function $S(Q)$, which can be obtained from experimental total scattering data after appropriate data treatments and corrections.[230] The r in $G(r)$ is the distance between a pair of atoms in the structure, and Q is the magnitude of the scattering vector. In a PDF histogram, peak positions present the bond length or atom-to-atom distance, and peak intensities are related to the relative abundance of each atom−atom pair.[231] Therefore, PDF provides direct structural information in real space, which can be quantitatively analyzed similarly to the Rietveld refinement, or by computational simulation and modeling.

The local structure of battery materials (either crystalline or amorphous) can become partially disordered during cycling. The disorder may play an important role in the electrochemical properties of battery materials. However, such local changes cannot be discerned by the conventional XRD. In this context, PDF technique stands out as an effective tool to address a series of questions that appear in electrode materials of SIBs, such as local short-range order, anion redox reaction mechanism, and Na storage mechanism.[232] In addition, due to the highly perceptive and low-absorption of high-energy X-rays, *in situ*/operando PDF studies are suitable for monitor the dynamics of battery materials during cycling.
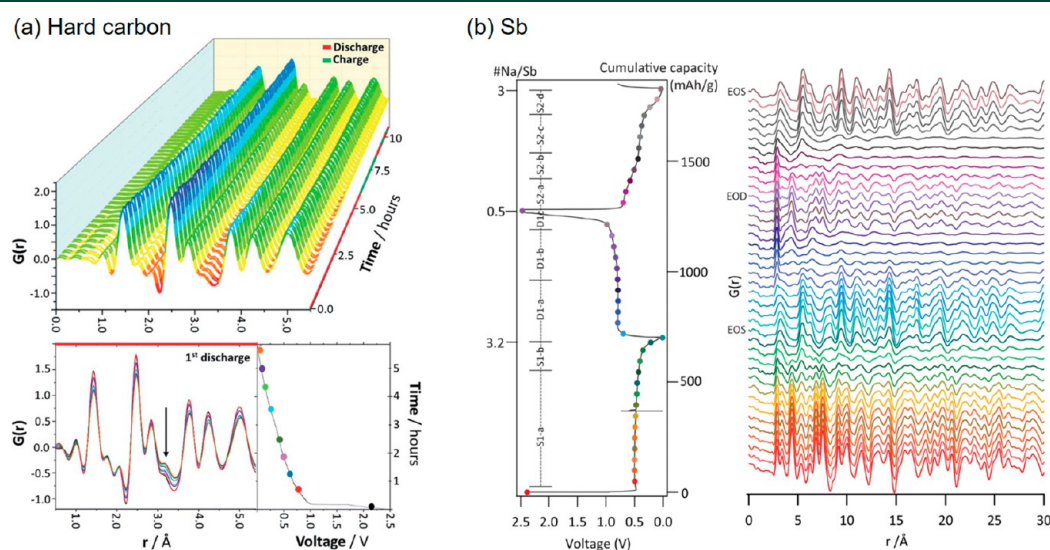
Figure 22. (a) Operando PDF study of the dynamic change of the graphene structure during sodiation/desodiation. (Top) Operando PDF data in the *r*-range. (Below) Selected operando PDFs of the first discharge. Reprinted with permission from ref 233. Copyright 2019 Royal Society of Chemistry. (b) Discharge−charge profiles obtained for Sb during the operando PDF study (left), and corresponding selected PDFs obtained from different discharge/charge states. Reprinted with permission from ref 235. Copyright 2016 American Chemical Society.

A typical application of operando PDF in SIBs is to study the structural response of the hard carbon electrode.[233] The C−C correlations between the in-plane and interplane distances at different states of discharge/charge are tracked by operando total scattering (Figure 22a). The PDF refinement data in this study shows the occurrence of in-plane elongation and contraction during cycling, which is related to a reversible charge transfer between the σ-orbitals of Na and the antibonding orbitals in the upper π-band of the graphene sheet. In addition, due to the introduction of Na into the host materials upon discharge, the peaks describing the C−C correlated distances are not being able to fully reverse back to the initial state, indicating the hard carbon structures become increasingly disordered upon Na intercalation. These irreversible structural changes are consistent with the observed irreversible capacity fading. It should be noted that there was no formation of Na metallic and clusters in this study, which is different from other reports.[234] The absence of metallic Na might be due to the state of Na metal formation has not yet been reached.

Grey's group recently used operando PDF analysis to study the alloying mechanism of Sb electrode during cycling and found that two intermediate phases are generated during sodiation: amorphous a-$Na_{1.7}$Sb with the structure featuring Sb−Sb bonding and amorphous a-Na_{3-x}Sb ($x \approx 0.4-0.5$) with the structure locally similar to the crystalline Na_3Sb phase but with a lot of Na vacancies (Figure 22b).[235] In the subsequent desodiation, a composite of amorphous and crystalline Sb network is formed via different reaction pathways at different voltages. They later used operando PDF coupled with other characterization techniques to investigate alloying reaction behaviors in Sn electrodes and cleared structures of amorphous and crystalline intermediates that were unidentified previously.[236]

Overall, the PDF represents another approach of deciphering the local structural information of battery materials ranging from non-crystalline and poorly crystalline to fully crystalline, complementary to XRD which provides global information of materials under investigation. Unfortunately, few reports using in situ/operando PDF have been conducted in the SIB systems, and it is hoped that such studies will provide more understanding of the electrochemical reaction mechanisms in electrode materials in the future.

The demand for the development of sustainable and large-scale energy storage systems provides an opportunity for SIBs. However, the issues of low capacity, degradation, and capacity fade have hindered practical applications of SIBs. The undesired degradation of SIBs occurs due to active host materials suffering from irreversible phase transformations, SEI formation, volume change, and so on. Further developments in addressing these problems rely on an in-depth and fundamental understanding of the relationships among the composition of electrode materials, morphology, phase transformations, heterogeneity in electrodes while in operation with the assistance of multi-modal characterization techniques.

In this Review, the major in situ and operando characterization techniques used in SIBs have been summarized. In microstructure-related characterization, in situ TEM has proved to be a useful tool to trace phase transformations and morphological evolutions during Na insertion/extraction processes. In situ/operando scattering techniques including XRD and PDF provide valuable information about monolithic/local structural evolutions and phase transformations during

charge/discharge cycles. Various spectroscopy techniques, such as in situ/operando XAS and TXM, can give information regarding charge compensation, local chemo-mechanical properties, and SOC heterogeneity. The recent development of these in situ and operando methods can not only directly elucidate structural evolution and identify reaction mechanisms under operating conditions but also supply comprehensive insights into the thermodynamic and kinetic processes. Therefore, the information from these in situ and operando techniques can energize research to improve and optimize novel energy materials in SIBs toward broad applications in the future. From the perspective of the targeted electrodes, an intercalation reaction is still the desired mechanism for decent cyclability and fast-charge performance, despite its moderate specific energy. Cathodes based on conversion reactions and anodes based on alloy reactions can be future directions to enhance the energy density of SIBs.

> Understanding the chemical and structural heterogeneity in battery particles, electrodes, and cells is non-trivial. Efforts should be made to lower or eliminate the chance of drawing biased conclusions.

Despite the extraordinary success and significant development of in situ and operando characterization techniques that have taken place in recent years, some important issues remain to be addressed in the future. For example, (1) in situ/operando techniques usually require complex experimental configurations and expensive devices, in facilities not conveniently accessible to most researchers. (2) Various novel in situ/operando configurations should be designed and optimized to mimic the working conditions of real battery cells. (3) Combination of different in situ and operando characterization techniques should be considered to provide more reliable, robust, and comprehensive interpretations of the SIB systems under study. For example, as shown in Figure 23a, the beam of electrons and X-rays produces various imaging, diffraction, and chemical information via constructive interference of scattered or unscattered waves, but the length scales are different. The wavelength/mean free path of electrons is shorter than that of X-rays. Hence, electron microscopies often unveil the localized information free of statistical significance, while X-ray-based characterizations can investigate the averaging behaviors of materials. In light of the electrochemical as well as mechanical heterogeneity across the electrode, attention to statistics is crucial to reduce biased conclusions. In addition, ex situ samples can also offer better statistical analysis of many-particle systems. (4) Compared to electrons, experimental configurations for in situ/operando high-energy X-ray measurements are easier to design and implement. Thus, it is hoped that the same area of a sample can be co-localized and examined by complementary characterizations. (5) The applications of in situ/operando techniques such as soft XAS, X-ray tomography, and PDF need to be greatly extended in SIBs. (6) From a fundamental point of view, the performance of a battery depends on the configuration of all internal components. Binders, conductive additives, and separators used in SIBs, although not electrochemically active, are necessary constituents in the electrodes. However, relevant in
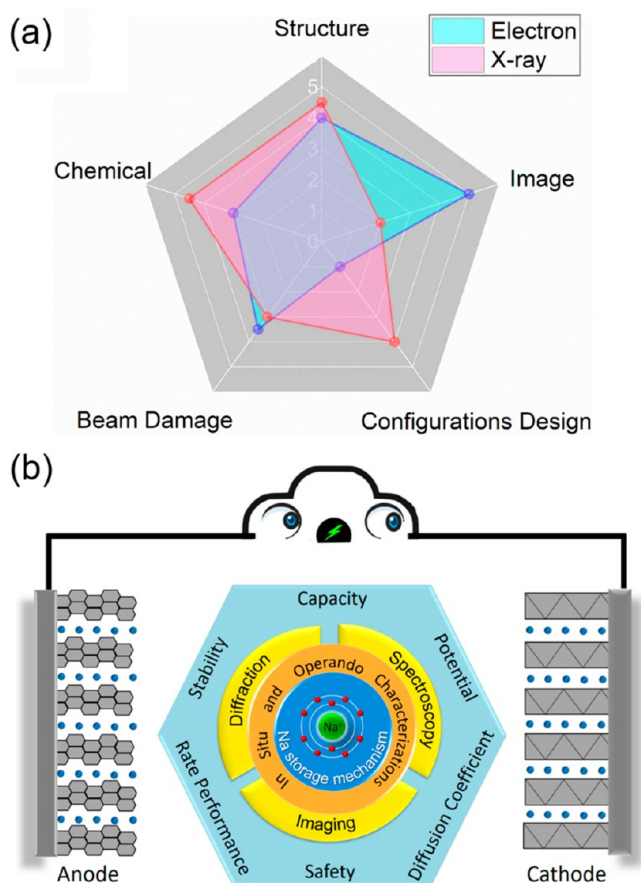
Figure 23. (a) Radar chart comparing electron and X-ray based methods. (b) An overview of various *in situ* and operando characterizations which promote the research and development of SIBs.

situ/operando research on these components is rare due to the need for more complex hardware. It is expected that craftier design of characterization techniques can be developed and used to elucidate the physical and electrochemical interrelationships between electrode materials and these inactive components. (7) The electron beam and X-ray interact with materials immediately after exposure; therefore, radiation damage cannot be overlooked.[237] (8) Understanding the chemical and structural heterogeneity in battery particles, electrodes, and cells is non-trivial. Efforts should be made to lower or eliminate the chance of drawing biased conclusions. (9) Fast data collection and data mining are needed to probe the non-equilibrium states in the study of SIBs. Some advanced *in situ*/operando techniques such as ultrafast XRD and quick XAS are important for kinetic studies of high rate cycling, so it is expected to expand these tools to study SIBs in the future. (10) High-throughput *in situ*/operando characterization techniques are very important for materials discovery and component optimization by the Materials Genome Initiative approach.[238] To improve the efficiency of characterization and accelerate data generation, expanding these techniques to SIB studies is expected. The screening of electrodes and electrolytes (especially solid-state electrolytes) can downsize the tremendous labor and expense related to laboratory trials. (11) Currently, an important megatrend in new materials design and large data processing is the increasing digitalization, which is often associated with terms like "smart manufacturing",

"machine learning", or "deep learning".[239,240] *In situ*/operando data of SIBs often exhibit complex characteristics due to their interactions with known and unknown structural evolution with cycling. Toward a larger scale, microstructural and physiochemical aspects with statistical confidence can be better quantified with the aid of machine learning. Therefore, it is promising to apply unsupervised learning to obtain perception beyond the current expert level for the understanding of battery performance, reaction, and degradation mechanisms. Given the recent developments, it can be expected that advanced *in situ* and operando characterization techniques will continue providing fundamental insights into the correlation between structural evolution and electrochemical performance in SIBs and keep playing a significant role in the development of future generations of SIBs (Figure 23b).

■ AUTHOR INFORMATION

Corresponding Authors

Feng Lin − *Department of Chemistry, Virginia Tech, Blacksburg, Virginia 24061, United States;* orcid.org/0000-0002-3729-3148; Email: fenglin@vt.edu

Yuzi Liu − *Center for Nanoscale Materials, Argonne National Laboratory, Argonne, Illinois 60439, United States;* orcid.org/0000-0002-8733-1683; Email: yuziliu@anl.gov

Hui Xiong − *Micron School of Materials Science and Engineering, Boise State University, Boise, Idaho 83725, United States; Center for Advanced Energy Studies, Idaho Falls, Idaho 83401, United States;* orcid.org/0000-0003-3126-1476; Email: clairexiong@boisestate.edu

Authors

Dewen Hou − *Micron School of Materials Science and Engineering, Boise State University, Boise, Idaho 83725, United States; Center for Nanoscale Materials, Argonne National Laboratory, Argonne, Illinois 60439, United States*

Dawei Xia − *Department of Chemistry, Virginia Tech, Blacksburg, Virginia 24061, United States*

Eric Gabriel − *Micron School of Materials Science and Engineering, Boise State University, Boise, Idaho 83725, United States*

Joshua A. Russell − *Micron School of Materials Science and Engineering, Boise State University, Boise, Idaho 83725, United States*

Kincaid Graff − *Micron School of Materials Science and Engineering, Boise State University, Boise, Idaho 83725, United States*

Yang Ren − *X-ray Science Division, Argonne National Laboratory, Argonne, Illinois 60439, United States*

Cheng-Jun Sun − *X-ray Science Division, Argonne National Laboratory, Argonne, Illinois 60439, United States*

Complete contact information is available at:
https://pubs.acs.org/10.1021/acsenergylett.1c01868

Author Contributions

§D.H. and D.X. contributed equally.

Notes

The authors declare no competing financial interest.

Biographies

Dewen Hou is a postdoctoral fellow in the Electrochemical Energy Materials Laboratory at Boise State University led by Professor Hui

(Claire) Xiong. His research focuses on advanced analytical TEM characterizations of electrode materials for sodium-ion batteries.

Dawei Xia is currently a graduate student under the supervision of Prof. Feng Lin in the Department of Chemistry at Virginia Tech. He is interested in discovering novel materials chemistry in the field of rechargeable batteries.

Eric Gabriel is a Ph.D. student in the Electrochemical Energy Materials Laboratory at Boise State University led by Professor Hui (Claire) Xiong. His research focuses on structural order/disorder, degradation mechanisms, and stabilization strategies for sodium-ion battery positive electrode materials at high potentials.

Joshua Russell is a graduate student in the Micron School of Materials Science and Engineering at Boise State University. He received his B.S. in materials science and engineering from North Carolina State University. His research interests include understanding the formation and evolution of the solid−electrolyte interphase at alkali and alkaline-earth metal electrodes as well as graphite electrodes in rechargeable batteries.

Kincaid Graff is a graduate student under the supervision of Prof. Hui Xiong at the Micron School of Materials Science and Engineering in Boise State University. His research focuses on the design, synthesis, and characterization of layered transition metal oxide positive electrodes for sodium-ion batteries.

Yang Ren is a Chair Professor of Physics at City University of Hong Kong. Previously he was a Senior Physicist at Argonne National Laboratory. He received his Ph.D. in chemical physics from Groningen University, The Netherlands. His research focuses on phase transition and structure−property studies using synchrotron and neutron techniques.

Cheng-Jun Sun is a beamline scientist at Argonne Photon Source, Argonne National Laboratory. He is interested in applying advanced X-ray spectroscopy in materials research.

Feng Lin is an Associate Professor of Chemistry at Virginia Tech. He holds a Bachelor's degree in materials science and engineering from Tianjin University and a Ph.D. degree in materials science from Colorado School of Mines. Previously, he worked at QuantumScape, Lawrence Berkeley National Laboratory, and National Renewable Energy Laboratory. His research interests include energy storage, catalysis, and smart windows. https://thelinlabatvt.weebly.com/

Yuzi Liu is a scientist at Argonne National Laboratory. He received his Ph.D. in condensed matter physics in 2007 from the Institute of Physics, The Chinese Academy of Sciences. His research focused on materials transformation studies by *in situ* electron microscopy to correlate the materials' performance to microstructure.

Hui (Claire) Xiong is an Associate Professor at the Micron School of Materials Science and Engineering at Boise State University. She received a Ph.D. degree in electroanalytical chemistry from the University of Pittsburgh (2007). Her research focuses on the design, development, and characterization of advanced energy materials for Li-ion and Na-ion batteries and beyond. https://www.boisestate.edu/coen-eeml/

■ REFERENCES

(1) Whittingham, M. S. Electrical Energy Storage and Intercalation Chemistry. *Science* **1976**, *192* (4244), 1126−1127.

(2) Whittingham, M. S.; Gamble, F. R. The Lithium Intercalates of the Transition Metal Dichalcogenides. *Mater. Res. Bull.* **1975**, *10* (5), 363−371.

(3) Fouassier, C.; Delmas, C.; Hagenmuller, P. Evolution structurale et proprietes physiques des phases AXMO2 (A = Na, K, M = Cr, Mn, Co) (x ⩽ 1). *Mater. Res. Bull.* **1975**, *10* (6), 443−449.

(4) Braconnier, J.-J.; Delmas, C.; Fouassier, C.; Hagenmuller, P. Comportement electrochimique des phases NaxCoO2. *Mater. Res. Bull.* **1980**, *15* (12), 1797−1804.

(5) Slater, M. D.; Kim, D.; Lee, E.; Johnson, C. S. Sodium-Ion Batteries. *Adv. Funct. Mater.* **2013**, *23* (8), 947−958.

(6) Komaba, S. Sodium-Driven Rechargeable Batteries: An Effort towards Future Energy Storage. *Chem. Lett.* **2020**, *49* (12), 1507−1516.

(7) Yabuuchi, N.; Kubota, K.; Dahbi, M.; Komaba, S. Research Development on Sodium-Ion Batteries. *Chem. Rev.* **2014**, *114* (23), 11636−11682.

(8) Nayak, P. K.; Yang, L.; Brehm, W.; Adelhelm, P. From Lithium-Ion to Sodium-Ion Batteries: Advantages, Challenges, and Surprises. *Angew. Chem., Int. Ed.* **2018**, *57* (1), 102−120.

(9) Li, Y.; Lu, Y.; Chen, L.; Hu, Y.-S. Failure Analysis with a Focus on Thermal Aspect towards Developing Safer Na-Ion Batteries. *Chin. Phys. B* **2020**, *29* (4), 048201.

(10) Shakourian-Fard, M.; Kamath, G.; Smith, K.; Xiong, H.; Sankaranarayanan, S. K. R. S. Trends in Na-Ion Solvation with Alkyl-Carbonate Electrolytes for Sodium-Ion Batteries: Insights from First-Principles Calculations. *J. Phys. Chem. C* **2015**, *119* (40), 22747−22759.

(11) Cannarella, J.; Liu, X.; Leng, C. Z.; Sinko, P. D.; Gor, G. Y.; Arnold, C. B. Mechanical Properties of a Battery Separator under Compression and Tension. *J. Electrochem. Soc.* **2014**, *161* (11), F3117.

(12) Eftekhari, A. On the Theoretical Capacity/Energy of Lithium Batteries and Their Counterparts. *ACS Sustainable Chem. Eng.* **2019**, *7* (4), 3684−3687.

(13) Kubota, K.; Dahbi, M.; Hosaka, T.; Kumakura, S.; Komaba, S. Towards K-Ion and Na-Ion Batteries as "Beyond Li-Ion.". *Chem. Rec.* **2018**, *18* (4), 459−479.

(14) Eftekhari, A.; Kim, D.-W. Sodium-Ion Batteries: New Opportunities beyond Energy Storage by Lithium. *J. Power Sources* **2018**, *395*, 336−348.

(15) Ong, S. P.; Chevrier, V. L.; Hautier, G.; Jain, A.; Moore, C.; Kim, S.; Ma, X.; Ceder, G. Voltage, Stability and Diffusion Barrier Differences between Sodium-Ion and Lithium-Ion Intercalation Materials. *Energy Environ. Sci.* **2011**, *4* (9), 3680.

(16) Yang, Z.; Lin, F. Heterogeneous, Defect-Rich Battery Particles and Electrodes: Why Do They Matter, and How Can One Leverage Them? *J. Phys. Chem. C* **2021**, *125* (18), 9618−9629.

(17) Zhang, W.; Zhang, F.; Ming, F.; Alshareef, H. N. Sodium-Ion Battery Anodes: Status and Future Trends. *EnergyChem* **2019**, *1* (2), 100012.

(18) Klein, F.; Jache, B.; Bhide, A.; Adelhelm, P. Conversion Reactions for Sodium-Ion Batteries. *Phys. Chem. Chem. Phys.* **2013**, *15* (38), 15876.

(19) Jiang, Z.; Li, J.; Yang, Y.; Mu, L.; Wei, C.; Yu, X.; Pianetta, P.; Zhao, K.; Cloetens, P.; Lin, F.; Liu, Y. Machine-Learning-Revealed Statistics of the Particle-Carbon/Binder Detachment in Lithium-Ion Battery Cathodes. *Nat. Commun.* **2020**, *11* (1), 2310.

(20) Qian, D.; Ma, C.; More, K. L.; Meng, Y. S.; Chi, M. Advanced Analytical Electron Microscopy for Lithium-Ion Batteries. *NPG Asia Mater.* **2015**, *7* (6), No. e193.

(21) Wu, F.; Yao, N. Advances in Sealed Liquid Cells for In-Situ TEM Electrochemial Investigation of Lithium-Ion Battery. *Nano Energy* **2015**, *11*, 196−210.

(22) Yan, Y.; Cheng, C.; Zhang, L.; Li, Y.; Lu, J. Deciphering the Reaction Mechanism of Lithium-Sulfur Batteries by In Situ/Operando Synchrotron-Based Characterization Techniques. *Adv. Energy Mater.* **2019**, *9* (18), 1900148.

(23) Liu, D.; Shadike, Z.; Lin, R.; Qian, K.; Li, H.; Li, K.; Wang, S.; Yu, Q.; Liu, M.; Ganapathy, S.; Qin, X.; Yang, Q.-H.; Wagemaker, M.; Kang, F.; Yang, X.-Q.; Li, B. Review of Recent Development of In Situ/Operando Characterization Techniques for Lithium Battery Research. *Adv. Mater.* **2019**, *31* (28), 1806620.

(24) Boebinger, M. G.; Lewis, J. A.; Sandoval, S. E.; McDowell, M. T. Understanding Transformations in Battery Materials Using in Situ and Operando Experiments: Progress and Outlook. *ACS Energy Lett.* **2020**, *5* (1), 335−345.

(25) Xiang, K.; Xing, W.; Ravnsbæk, D. B.; Hong, L.; Tang, M.; Li, Z.; Wiaderek, K. M.; Borkiewicz, O. J.; Chapman, K. W.; Chupas, P. J.; Chiang, Y.-M. Accommodating High Transformation Strains in Battery Electrodes via the Formation of Nanoscale Intermediate Phases: Operando Investigation of Olivine NaFePO4. *Nano Lett.* **2017**, *17* (3), 1696−1702.

(26) Xiao, B.; Wang, K.; Xu, G.-L.; Song, J.; Chen, Z.; Amine, K.; Reed, D.; Sui, M.; Sprenkle, V.; Ren, Y.; Yan, P.; Li, X. Revealing the Atomic Origin of Heterogeneous Li-Ion Diffusion by Probing Na. *Adv. Mater.* **2019**, *31* (29), 1805889.

(27) Williams, D. B.; Carter, C. B. *Transmission Electron Microscopy: A Textbook for Materials Science*, 2nd ed.; Springer: New York, 2008.

(28) Schmidt, J.; Hartmann, R.; Holl, P.; Huth, M.; Lutz, G.; Ryll, H.; Send, S.; Simson, M.; Steigenhöfer, D.; Soltau, J.; Soltau, H.; Strüder, L. Extending the Dynamic Range of Fully Depleted PnCCDs. *J. Instrum.* **2014**, *9* (10), P10008−P10008.

(29) Wang, C.-M. In Situ Transmission Electron Microscopy and Spectroscopy Studies of Rechargeable Batteries under Dynamic Operating Conditions: A Retrospective and Perspective View. *J. Mater. Res.* **2015**, *30* (3), 326−339.

(30) Rodriguez, J. R.; Aguirre, S. B.; Pol, V. G. Role of Operando Microscopy Techniques on the Advancement of Sustainable Sodium-Ion Battery Anodes. *J. Power Sources* **2019**, *437*, 226851.

(31) Huang, J. Y.; Zhong, L.; Wang, C. M.; Sullivan, J. P.; Xu, W.; Zhang, L. Q.; Mao, S. X.; Hudak, N. S.; Liu, X. H.; Subramanian, A.; Fan, H.; Qi, L.; Kushima, A.; Li, J. In Situ Observation of the Electrochemical Lithiation of a Single SnO2 Nanowire Electrode. *Science* **2010**, *330* (6010), 1515−1520.

(32) Gu, M.; Parent, L. R.; Mehdi, B. L.; Unocic, R. R.; McDowell, M. T.; Sacci, R. L.; Xu, W.; Connell, J. G.; Xu, P.; Abellan, P.; Chen, X.; Zhang, Y.; Perea, D. E.; Evans, J. E.; Lauhon, L. J.; Zhang, J.-G.; Liu, J.; Browning, N. D.; Cui, Y.; Arslan, I.; Wang, C.-M. Demonstration of an Electrochemical Liquid Cell for Operando Transmission Electron Microscopy Observation of the Lithiation/Delithiation Behavior of Si Nanowire Battery Anodes. *Nano Lett.* **2013**, *13* (12), 6106−6112.

(33) Liu, Y.; Fan, F.; Wang, J.; Liu, Y.; Chen, H.; Jungjohann, K. L.; Xu, Y.; Zhu, Y.; Bigio, D.; Zhu, T.; Wang, C. In Situ Transmission Electron Microscopy Study of Electrochemical Sodiation and Potassiation of Carbon Nanofibers. *Nano Lett.* **2014**, *14* (6), 3445−3452.

(34) Wen, Y.; He, K.; Zhu, Y.; Han, F.; Xu, Y.; Matsuda, I.; Ishii, Y.; Cumings, J.; Wang, C. Expanded Graphite as Superior Anode for Sodium-Ion Batteries. *Nat. Commun.* **2014**, *5* (1), 4033.

(35) Jian, Z.; Bommier, C.; Luo, L.; Li, Z.; Wang, W.; Wang, C.; Greaney, P. A.; Ji, X. Insights on the Mechanism of Na-Ion Storage in Soft Carbon Anode. *Chem. Mater.* **2017**, *29* (5), 2314−2320.

(36) Yoon, G.; Kim, H.; Park, I.; Kang, K. Conditions for Reversible Na Intercalation in Graphite: Theoretical Studies on the Interplay Among Guest Ions, Solvent, and Graphite Host. *Advanced Energy Materials* **2017**, *7* (2), 1601519.

(37) Yang, Y.; Tang, D.-M.; Zhang, C.; Zhang, Y.; Liang, Q.; Chen, S.; Weng, Q.; Zhou, M.; Xue, Y.; Liu, J.; Wu, J.; Cui, Q. H.; Lian, C.; Hou, G.; Yuan, F.; Bando, Y.; Golberg, D.; Wang, X. "Protrusions" or "Holes" in Graphene: Which Is the Better Choice for Sodium Ion Storage? *Energy Environ. Sci.* **2017**, *10* (4), 979−986.

(38) Chen, D.; Zhang, W.; Luo, K.; Song, Y.; Zhong, Y.; Liu, Y.; Wang, G.; Zhong, B.; Wu, Z.; Guo, X. Hard Carbon for Sodium Storage: Mechanism and Optimization Strategies toward Commercialization. *Energy Environ. Sci.* **2021**, *14* (4), 2244−2262.

(39) Li, X.; Zhao, L.; Li, P.; Zhang, Q.; Wang, M.-S. In-Situ Electron Microscopy Observation of Electrochemical Sodium Plating and Stripping Dynamics on Carbon Nanofiber Current Collectors. *Nano Energy* **2017**, *42*, 122−128.

(40) Wang, K.; Xu, Y.; Li, Y.; Dravid, V.; Wu, J.; Huang, Y. Sodium Storage in Hard Carbon with Curved Graphene Platelets as the Basic Structural Units. *J. Mater. Chem. A* **2019**, *7* (7), 3327−3335.

(41) Wang, J. W.; Liu, X. H.; Mao, S. X.; Huang, J. Y. Microstructural Evolution of Tin Nanoparticles during In Situ Sodium Insertion and Extraction. *Nano Lett.* **2012**, *12* (11), 5897−5902.

(42) Li, Z.; Tan, X.; Li, P.; Kalisvaart, P.; Janish, M. T.; Mook, W. M.; Luber, E. J.; Jungjohann, K. L.; Carter, C. B.; Mitlin, D. Coupling In Situ TEM and Ex Situ Analysis to Understand Heterogeneous Sodiation of Antimony. *Nano Lett.* **2015**, *15* (10), 6339−6348.

(43) Selvaraj, B.; Wang, C.-C.; Song, Y.-F.; Sheu, H.-S.; Liao, Y.-F.; Wu, N.-L. Remarkable Microstructural Reversibility of Antimony in Sodium Ion Battery Anodes. *J. Mater. Chem. A* **2020**, *8*, 22620−22625.

(44) Lu, X.; Adkins, E. R.; He, Y.; Zhong, L.; Luo, L.; Mao, S. X.; Wang, C.-M.; Korgel, B. A. Germanium as a Sodium Ion Battery Material: *In Situ* TEM Reveals Fast Sodiation Kinetics with High Capacity. *Chem. Mater.* **2016**, *28* (4), 1236−1242.

(45) Huang, Y.; Zhu, C.; Zhang, S.; Hu, X.; Zhang, K.; Zhou, W.; Guo, S.; Xu, F.; Zeng, H. Ultrathin Bismuth Nanosheets for Stable Na-Ion Batteries: Clarification of Structure and Phase Transition by in Situ Observation. *Nano Lett.* **2019**, *19* (2), 1118−1123.

(46) Xie, H.; Tan, X.; Luber, E. J.; Olsen, B. C.; Kalisvaart, W. P.; Jungjohann, K. L.; Mitlin, D.; Buriak, J. M. β-SnSb for Sodium Ion Battery Anodes: Phase Transformations Responsible for Enhanced Cycling Stability Revealed by In Situ TEM. *ACS Energy Lett.* **2018**, *3* (7), 1670−1676.

(47) Gutiérrez-Kolar, J. S.; Baggetto, L.; Sang, X.; Shin, D.; Yurkiv, V.; Mashayek, F.; Veith, G. M.; Shahbazian-Yassar, R.; Unocic, R. R. Interpreting Electrochemical and Chemical Sodiation Mechanisms and Kinetics in Tin Antimony Battery Anodes Using *in Situ* Transmission Electron Microscopy and Computational Methods. *ACS Appl. Energy Mater.* **2019**, *2* (5), 3578−3586.

(48) Fang, Y.; Xiao, L.; Chen, Z.; Ai, X.; Cao, Y.; Yang, H. Recent Advances in Sodium-Ion Battery Materials. *Electrochem. Energ. Rev.* **2018**, *1* (3), 294−323.

(49) Chen, D.; Peng, L.; Yuan, Y.; Zhu, Y.; Fang, Z.; Yan, C.; Chen, G.; Shahbazian-Yassar, R.; Lu, J.; Amine, K.; Yu, G. Two-Dimensional Holey Co3O4 Nanosheets for High-Rate Alkali-Ion Batteries: From Rational Synthesis to in Situ Probing. *Nano Lett.* **2017**, *17* (6), 3907−3913.

(50) Li, Q.; Wu, J.; Xu, J.; Dravid, V. P. Synergistic Sodiation of Cobalt Oxide Nanoparticles and Conductive Carbon Nanotubes (CNTs) for Sodium-Ion Batteries. *J. Mater. Chem. A* **2016**, *4* (22), 8669−8675.

(51) He, K.; Lin, F.; Zhu, Y.; Yu, X.; Li, J.; Lin, R.; Nordlund, D.; Weng, T.-C.; Richards, R. M.; Yang, X.-Q.; Doeff, M. M.; Stach, E. A.; Mo, Y.; Xin, H. L.; Su, D. Sodiation Kinetics of Metal Oxide

Conversion Electrodes: A Comparative Study with Lithiation. *Nano Lett.* **2015**, *15* (9), 5755−5763.

(52) Asayesh-Ardakani, H.; Yao, W.; Yuan, Y.; Nie, A.; Amine, K.; Lu, J.; Shahbazian-Yassar, R. In Situ TEM Investigation of ZnO Nanowires during Sodiation and Lithiation Cycling. *Small Methods* **2017**, *1* (9), 1700202.

(53) Xu, F.; Li, Z.; Wu, L.; Meng, Q.; Xin, H. L.; Sun, J.; Ge, B.; Sun, L.; Zhu, Y. In Situ TEM Probing of Crystallization Form-Dependent Sodiation Behavior in ZnO Nanowires for Sodium-Ion Batteries. *Nano Energy* **2016**, *30*, 771−779.

(54) Xia, W.; Xu, F.; Zhu, C.; Xin, H. L.; Xu, Q.; Sun, P.; Sun, L. Probing Microstructure and Phase Evolution of α-MoO3 Nanobelts for Sodium-Ion Batteries by in Situ Transmission Electron Microscopy. *Nano Energy* **2016**, *27*, 447−456.

(55) Zhu, C.; Xu, F.; Min, H.; Huang, Y.; Xia, W.; Wang, Y.; Xu, Q.; Gao, P.; Sun, L. Identifying the Conversion Mechanism of NiCo$_2$O$_4$ during Sodiation-Desodiation Cycling by In Situ TEM. *Adv. Funct. Mater.* **2017**, *27* (17), 1606163.

(56) Zhang, L.; Wang, Y.; Xie, D.; Tang, Y.; Wu, C.; Cui, L.; Li, Y.; Ning, X.; Shan, Z. In Situ Transmission Electron Microscopy Study of the Electrochemical Sodiation Process for a Single CuO Nanowire Electrode. *RSC Adv.* **2016**, *6* (14), 11441−11445.

(57) Liu, H.; Zheng, H.; Li, L.; Jia, S.; Meng, S.; Cao, F.; Lv, Y.; Zhao, D.; Wang, J. Surface-Coating-Mediated Electrochemical Performance in CuO Nanowires during the Sodiation-Desodiation Cycling. *Adv. Mater. Interfaces* **2018**, *5* (4), 1701255.

(58) Liu, H.; Cao, F.; Zheng, H.; Sheng, H.; Li, L.; Wu, S.; Liu, C.; Wang, J. In Situ Observation of the Sodiation Process in CuO Nanowires. *Chem. Commun.* **2015**, *51* (52), 10443−10446.

(59) Zhang, Z.; Qian, J.; Lu, W.; Chan, C. H.; Lau, S. P.; Dai, J.-Y. In Situ TEM Study of the Sodiation/Desodiation Mechanism of MnO2 Nanowire with Gel-Electrolytes. *Energy Storage Materials* **2018**, *15*, 91−97.

(60) Yuan, Y.; Ma, L.; He, K.; Yao, W.; Nie, A.; Bi, X.; Amine, K.; Wu, T.; Lu, J.; Shahbazian-Yassr, R. Dynamic Study of (De)Sodiation in Alpha-MnO2 Nanowires. *Nano Energy* **2016**, *19*, 382−390.

(61) Xia, X.; Wang, Q.; Zhu, Q.; Xie, J.; Wang, J.; Zhuang, D.; Zhang, S.; Cao, G.; Zhao, X. Improved Na-Storage Cycling of Amorphous-Carbon-Sheathed Ni$_3$S$_2$ Arrays and Investigation by in Situ TEM Characterization. *Materials Today Energy* **2017**, *5*, 99−106.

(62) Wu, K.; Chen, F.; Ma, Z.; Guo, B.; Lyu, Y.; Wang, P.; Yang, H.; Li, Q.; Wang, H.; Nie, A. In Situ TEM and Half Cell Investigation of Sodium Storage in Hexagonal FeSe Nanoparticles. *Chem. Commun.* **2019**, *55* (39), 5611−5614.

(63) Boebinger, M. G.; Xu, M.; Ma, X.; Chen, H.; Unocic, R. R.; McDowell, M. T. Distinct Nanoscale Reaction Pathways in a Sulfide Material for Sodium and Lithium Batteries. *J. Mater. Chem. A* **2017**, *5* (23), 11701−11709.

(64) Su, Q.; Du, G.; Zhang, J.; Zhong, Y.; Xu, B.; Yang, Y.; Neupane, S.; Li, W. In Situ Transmission Electron Microscopy Observation of Electrochemical Sodiation of Individual Co$_9$S$_8$-Filled Carbon Nanotubes. *ACS Nano* **2014**, *8* (4), 3620−3627.

(65) Ni, J.; Li, L.; Lu, J. Phosphorus: An Anode of Choice for Sodium-Ion Batteries. *ACS Energy Lett.* **2018**, *3* (5), 1137−1144.

(66) Sun, J.; Lee, H.-W.; Pasta, M.; Yuan, H.; Zheng, G.; Sun, Y.; Li, Y.; Cui, Y. A Phosphorene-Graphene Hybrid Material as a High-Capacity Anode for Sodium-Ion Batteries. *Nat. Nanotechnol.* **2015**, *10* (11), 980−985.

(67) Chen, T.; Zhao, P.; Guo, X.; Zhang, S. Two-Fold Anisotropy Governs Morphological Evolution and Stress Generation in Sodiated Black Phosphorus for Sodium Ion Batteries. *Nano Lett.* **2017**, *17* (4), 2299−2306.

(68) Nie, A.; Cheng, Y.; Ning, S.; Foroozan, T.; Yasaei, P.; Li, W.; Song, B.; Yuan, Y.; Chen, L.; Salehi-Khojin, A.; Mashayek, F.; Shahbazian-Yassar, R. Selective Ionic Transport Pathways in Phosphorene. *Nano Lett.* **2016**, *16* (4), 2240−2247.

(69) Shi, S.; Sun, C.; Yin, X.; Shen, L.; Shi, Q.; Zhao, K.; Zhao, Y.; Zhang, J. FeP Quantum Dots Confined in Carbon-Nanotube-Grafted P-Doped Carbon Octahedra for High-Rate Sodium Storage and Full-Cell Applications. *Adv. Funct. Mater.* **2020**, *30* (10), 1909283.

(70) Han, B.; Chen, S.; Zou, J.; Shao, R.; Dou, Z.; Yang, C.; Ma, X.; Lu, J.; Liu, K.; Yu, D.; Wang, L.; Wang, H.; Gao, P. Tracking Sodium Migration in TiS$_2$ Using in Situ TEM. *Nanoscale* **2019**, *11* (15), 7474−7480.

(71) Wang, X.; Yao, Z.; Hwang, S.; Pan, Y.; Dong, H.; Fu, M.; Li, N.; Sun, K.; Gan, H.; Yao, Y.; Aspuru-Guzik, A.; Xu, Q.; Su, D. In Situ Electron Microscopy Investigation of Sodiation of Titanium Disulfide Nanoflakes. *ACS Nano* **2019**, *13* (8), 9421−9430.

(72) Zhang, L.; Tang, Y.; Wang, Y.; Duan, Y.; Xie, D.; Wu, C.; Cui, L.; Li, Y.; Ning, X.; Shan, Z. In Situ TEM Observing Structural Transitions of MoS$_2$ upon Sodium Insertion and Extraction. *RSC Adv.* **2016**, *6* (98), 96035−96038.

(73) Li, Q.; Yao, Z.; Wu, J.; Mitra, S.; Hao, S.; Sahu, T. S.; Li, Y.; Wolverton, C.; Dravid, V. P. Intermediate Phases in Sodium Intercalation into MoS2 Nanosheets and Their Implications for Sodium-Ion Batteries. *Nano Energy* **2017**, *38*, 342−349.

(74) Boebinger, M. G.; Yeh, D.; Xu, M.; Miles, B. C.; Wang, B.; Papakyriakou, M.; Lewis, J. A.; Kondekar, N. P.; Cortes, F. J. Q.; Hwang, S.; Sang, X.; Su, D.; Unocic, R. R.; Xia, S.; Zhu, T.; McDowell, M. T. Avoiding Fracture in a Conversion Battery Material through Reaction with Larger Ions. *Joule* **2018**, *2* (9), 1783−1799.

(75) Xu, X.; Niu, C.; Duan, M.; Wang, X.; Huang, L.; Wang, J.; Pu, L.; Ren, W.; Shi, C.; Meng, J.; Song, B.; Mai, L. Alkaline Earth Metal Vanadates as Sodium-Ion Battery Anodes. *Nat. Commun.* **2017**, *8* (1), 460.

(76) Yao, L.; Xia, W.; Zhang, H.; Dong, H.; Xin, H. L.; Gao, P.; Cai, R.; Zhu, C.; Wu, Y.; Nie, M.; Lei, S.; Sun, L.; Xu, F. In Situ Visualization of Sodium Transport and Conversion Reactions of FeS2 Nanotubes Made by Morphology Engineering. *Nano Energy* **2019**, *60*, 424−431.

(77) Yao, S.; Cui, J.; Lu, Z.; Xu, Z.-L.; Qin, L.; Huang, J.; Sadighi, Z.; Ciucci, F.; Kim, J.-K. Unveiling the Unique Phase Transformation Behavior and Sodiation Kinetics of 1D van Der Waals Sb$_2$S$_3$ Anodes for Sodium Ion Batteries. *Adv. Energy Mater.* **2017**, *7* (8), 1602149.

(78) Marino, C.; Block, T.; Pöttgen, R.; Villevieille, C. CuSbS2 as a Negative Electrode Material for Sodium Ion Batteries. *J. Power Sources* **2017**, *342*, 616−622.

(79) Yang, C.; Liang, X.; Ou, X.; Zhang, Q.; Zheng, H.-S.; Zheng, F.; Wang, J.-H.; Huang, K.; Liu, M. Heterostructured Nanocube-Shaped Binary Sulfide (SnCo)S$_2$ Interlaced with S-Doped Graphene as a High-Performance Anode for Advanced Na + Batteries. *Adv. Funct. Mater.* **2019**, *29* (9), 1807971.

(80) Wu, Y.; Luo, W.; Gao, P.; Zhu, C.; Hu, X.; Qu, K.; Chen, J.; Wang, Y.; Sun, L.; Mai, L.; Xu, F. Unveiling the Microscopic Origin of Asymmetric Phase Transformations in (de)Sodiated Sb2Se3 with in Situ Transmission Electron Microscopy. *Nano Energy* **2020**, *77*, 105299.

(81) Cui, J.; Zheng, H.; Zhang, Z.; Hwang, S.; Yang, X.-Q.; He, K. Origin of Anomalous High-Rate Na-Ion Electrochemistry in Layered Bismuth Telluride Anodes. *Matter* **2021**, *4* (4), 1335−1351.

(82) Gu, M.; Kushima, A.; Shao, Y.; Zhang, J.-G.; Liu, J.; Browning, N. D.; Li, J.; Wang, C. Probing the Failure Mechanism of SnO$_2$ Nanowires for Sodium-Ion Batteries. *Nano Lett.* **2013**, *13* (11), 5203−5211.

(83) Yuan, Y.; Amine, K.; Lu, J.; Shahbazian-Yassar, R. Understanding Materials Challenges for Rechargeable Ion Batteries with in Situ Transmission Electron Microscopy. *Nat. Commun.* **2017**, *8* (1), 15806.

(84) Lin, S.; Li, Y.; Lu, W.; Chui, Y. S.; Rogée, L.; Bao, Q.; Lau, S. P. *In Situ* Observation of the Thermal Stability of Black Phosphorus. *2D Mater.* **2017**, *4* (2), 025001.

(85) Hwang, S.; Lee, Y.; Jo, E.; Chung, K. Y.; Choi, W.; Kim, S. M.; Chang, W. Investigation of Thermal Stability of P2-Na$_x$CoO$_2$ Cathode Materials for Sodium Ion Batteries Using Real-Time Electron Microscopy. *ACS Appl. Mater. Interfaces* **2017**, *9* (22), 18883−18888.

(86) Liu, X.; Wood, J. D.; Chen, K.-S.; Cho, E.; Hersam, M. C. In Situ Thermal Decomposition of Exfoliated Two-Dimensional Black Phosphorus. *J. Phys. Chem. Lett.* **2015**, *6* (5), 773−778.

(87) Liu, Q.; Zhang, L.; Sun, H.; Geng, L.; Li, Y.; Tang, Y.; Jia, P.; Wang, Z.; Dai, Q.; Shen, T.; Tang, Y.; Zhu, T.; Huang, J. *In Situ* Observation of Sodium Dendrite Growth and Concurrent Mechanical Property Measurements Using an Environmental Transmission Electron Microscopy-Atomic Force Microscopy (ETEM-AFM) Platform. *ACS Energy Lett.* **2020**, *5* (8), 2546−2559.

(88) Fincher, C. D.; Zhang, Y.; Pharr, G. M.; Pharr, M. Elastic and Plastic Characteristics of Sodium Metal. *ACS Appl. Energy Mater.* **2020**, *3* (2), 1759−1767.

(89) Chauhan, A. Powder XRD Technique and Its Applications in Science and Technology. *J. Anal. Bioanal. Tech.* **2014**, *5* (5), 1000212.

(90) Toby, B. H.; Von Dreele, R. B. *GSAS-II*: The Genesis of a Modern Open-Source All Purpose Crystallography Software Package. *J. Appl. Crystallogr.* **2013**, *46* (2), 544−549.

(91) O'Connor, B. H.; Raven, M. D. Application of the Rietveld Refinement Procedure in Assaying Powdered Mixtures. *Powder Diffr.* **1988**, *3* (1), 2−6.

(92) Sedigh Rahimabadi, P.; Khodaei, M.; Koswattage, K. R. Review on Applications of Synchrotron-based X-ray Techniques in Materials Characterization. *X-Ray Spectrom.* **2020**, *49* (3), 348−373.

(93) Lin, F.; Liu, Y.; Yu, X.; Cheng, L.; Singer, A.; Shpyrko, O. G.; Xin, H. L.; Tamura, N.; Tian, C.; Weng, T.-C.; Yang, X.-Q.; Meng, Y. S.; Nordlund, D.; Yang, W.; Doeff, M. M. Synchrotron X-Ray Analytical Techniques for Studying Materials Electrochemistry in Rechargeable Batteries. *Chem. Rev.* **2017**, *117* (21), 13123−13186.

(94) Shadike, Z.; Zhao, E.; Zhou, Y.-N.; Yu, X.; Yang, Y.; Hu, E.; Bak, S.; Gu, L.; Yang, X.-Q. Advanced Characterization Techniques for Sodium-Ion Battery Studies. *Adv. Energy Mater.* **2018**, *8* (17), 1702588.

(95) Hu, Z.; Liu, Q.; Zhang, K.; Zhou, L.; Li, L.; Chen, M.; Tao, Z.; Kang, Y.-M.; Mai, L.; Chou, S.-L.; Chen, J.; Dou, S.-X. All Carbon Dual Ion Batteries. *ACS Appl. Mater. Interfaces* **2018**, *10* (42), 35978−35983.

(96) Bak, S.-M.; Shadike, Z.; Lin, R.; Yu, X.; Yang, X.-Q. In Situ/Operando Synchrotron-Based X-Ray Techniques for Lithium-Ion Battery Research. *NPG Asia Mater.* **2018**, *10* (7), 563−580.

(97) Qiu, S.; Xiao, L.; Sushko, M. L.; Han, K. S.; Shao, Y.; Yan, M.; Liang, X.; Mai, L.; Feng, J.; Cao, Y.; Ai, X.; Yang, H.; Liu, J. Manipulating Adsorption-Insertion Mechanisms in Nanostructured Carbon Materials for High-Efficiency Sodium Ion Storage. *Adv. Energy Mater.* **2017**, *7* (17), 1700403.

(98) Xu, Z.-L.; Lim, K.; Park, K.-Y.; Yoon, G.; Seong, W. M.; Kang, K. Engineering Solid Electrolyte Interphase for Pseudocapacitive Anatase TiO$_2$ Anodes in Sodium-Ion Batteries. *Adv. Funct. Mater.* **2018**, *28* (29), 1802099.

(99) Lee, J.; Lee, J. K.; Chung, K. Y.; Jung, H.-G.; Kim, H.; Mun, J.; Choi, W. Electrochemical Investigations on TiO 2 -B Nanowires as a Promising High Capacity Anode for Sodium-Ion Batteries. *Electrochim. Acta* **2016**, *200*, 21−28.

(100) Delmas, C.; Fouassier, C.; Hagenmuller, P. Structural Classification and Properties of the Layered Oxides. *Physica B+C* **1980**, *99* (1-4), 81−85.

(101) Zheng, X.; Li, P.; Zhu, H.; Rui, K.; Zhao, G.; Shu, J.; Xu, X.; Sun, W.; Dou, S. X. New Insights into Understanding the Exceptional Electrochemical Performance of P2-Type Manganese-Based Layered Oxide Cathode for Sodium Ion Batteries. *Energy Storage Materials* **2018**, *15*, 257−265.

(102) Wen, Y.; Wang, B.; Zeng, G.; Nogita, K.; Ye, D.; Wang, L. Electrochemical and Structural Study of Layered P2-Type Na$_{2/3}$Ni$_{1/3}$Mn$_{2/3}$O$_2$ as Cathode Material for Sodium-Ion Battery. *Chem. - Asian J.* **2015**, *10* (3), 661−666.

(103) He, X.; Wang, J.; Qiu, B.; Paillard, E.; Ma, C.; Cao, X.; Liu, H.; Stan, M. C.; Liu, H.; Gallash, T.; Meng, Y. S.; Li, J. Durable High-Rate Capability Na0.44MnO2 Cathode Material for Sodium-Ion Batteries. *Nano Energy* **2016**, *27*, 602−610.

(104) Bianchini, M.; Wang, J.; Clément, R.; Ceder, G. A First-Principles and Experimental Investigation of Nickel Solubility into the P2 Na$_x$CoO$_2$ Sodium-Ion Cathode. *Adv. Energy Mater.* **2018**, *8* (26), 1801446.

(105) Jung, Y. H.; Christiansen, A. S.; Johnsen, R. E.; Norby, P.; Kim, D. K. In Situ X-Ray Diffraction Studies on Structural Changes of a P2 Layered Material during Electrochemical Desodiation/Sodiation. *Adv. Funct. Mater.* **2015**, *25* (21), 3227−3237.

(106) Han, M. H.; Gonzalo, E.; Sharma, N.; López del Amo, J. M.; Armand, M.; Avdeev, M.; Saiz Garitaonandia, J. J.; Rojo, T. High-Performance P2-Phase Na$_{2/3}$Mn$_{0.8}$Fe$_{0.1}$Ti$_{0.1}$O$_2$ Cathode Material for Ambient-Temperature Sodium-Ion Batteries. *Chem. Mater.* **2016**, *28* (1), 106−116.

(107) Xu, S.; Wu, J.; Hu, E.; Li, Q.; Zhang, J.; Wang, Y.; Stavitski, E.; Jiang, L.; Rong, X.; Yu, X.; Yang, W.; Yang, X.-Q.; Chen, L.; Hu, Y.-S. Suppressing the Voltage Decay of Low-Cost P2-Type Iron-Based Cathode Materials for Sodium-Ion Batteries. *J. Mater. Chem. A* **2018**, *6* (42), 20795−20803.

(108) Xiao, J.; Zhang, F.; Tang, K.; Li, X.; Wang, D.; Wang, Y.; Liu, H.; Wu, M.; Wang, G. Rational Design of a P2-Type Spherical Layered Oxide Cathode for High-Performance Sodium-Ion Batteries. *ACS Cent. Sci.* **2019**, *5* (12), 1937−1945.

(109) Bucher, N.; Hartung, S.; Franklin, J. B.; Wise, A. M.; Lim, L. Y.; Chen, H.-Y.; Weker, J. N.; Toney, M. F.; Srinivasan, M. P2-Na$_x$Co$_y$Mn$_{1-y}$O$_2$ (y = 0, 0.1) as Cathode Materials in Sodium-Ion Batteries—Effects of Doping and Morphology To Enhance Cycling Stability. *Chem. Mater.* **2016**, *28* (7), 2041−2051.

(110) Xie, Y.; Gabriel, E.; Fan, L.; Hwang, I.; Li, X.; Zhu, H.; Ren, Y.; Sun, C.; Pipkin, J.; Dustin, M.; Li, M.; Chen, Z.; Lee, E.; Xiong, H. Role of Lithium Doping in P2-Na0.67Ni0.33Mn0.67O2 for Sodium-Ion Batteries. *Chem. Mater.* **2021**, *33* (12), 4445−4455.

(111) Konarov, A.; Kim, H. J.; Voronina, N.; Bakenov, Z.; Myung, S.-T. P2-Na$_{2/3}$MnO$_2$ by Co Incorporation: As a Cathode Material of High Capacity and Long Cycle Life for Sodium-Ion Batteries. *ACS Appl. Mater. Interfaces* **2019**, *11* (32), 28928−28933.

(112) Wang, P.-F.; Yao, H.-R.; Liu, X.-Y.; Yin, Y.-X.; Zhang, J.-N.; Wen, Y.; Yu, X.; Gu, L.; Guo, Y.-G. Na+/Vacancy Disordering Promises High-Rate Na-Ion Batteries. *Sci. Adv.* **2018**, *4* (3), No. aaar6018.

(113) Wang, L.; Sun, Y.-G.; Hu, L.-L.; Piao, J.-Y.; Guo, J.; Manthiram, A.; Ma, J.; Cao, A.-M. Copper-Substituted Na$_{0.67}$Ni$_{0.3-x}$Cu$_x$Mn$_{0.7}$O$_2$ Cathode Materials for Sodium-Ion Batteries with Suppressed P2-O2 Phase Transition. *J. Mater. Chem. A* **2017**, *5* (18), 8752−8761.

(114) Wu, X.; Xu, G.-L.; Zhong, G.; Gong, Z.; McDonald, M. J.; Zheng, S.; Fu, R.; Chen, Z.; Amine, K.; Yang, Y. Insights into the Effects of Zinc Doping on Structural Phase Transition of P2-Type Sodium Nickel Manganese Oxide Cathodes for High-Energy Sodium Ion Batteries. *ACS Appl. Mater. Interfaces* **2016**, *8* (34), 22227−22237.

(115) Wen, Y.; Fan, J.; Shi, C.; Dai, P.; Hong, Y.; Wang, R.; Wu, L.; Zhou, Z.; Li, J.; Huang, L.; Sun, S.-G. Probing into the Working Mechanism of Mg versus Co in Enhancing the Electrochemical Performance of P2-Type Layered Composite for Sodium-Ion Batteries. *Nano Energy* **2019**, *60*, 162−170.

(116) Xiao, Y.; Zhu, Y.; Yao, H.; Wang, P.; Zhang, X.; Li, H.; Yang, X.; Gu, L.; Li, Y.; Wang, T.; Yin, Y.; Guo, X.; Zhong, B.; Guo, Y. A Stable Layered Oxide Cathode Material for High-Performance Sodium-Ion Battery. *Adv. Energy Mater.* **2019**, *9* (19), 1803978.

(117) Kubota, K.; Asari, T.; Yoshida, H.; Yaabuuchi, N.; Shiiba, H.; Nakayama, M.; Komaba, S. Understanding the Structural Evolution and Redox Mechanism of a NaFeO$_2$-NaCoO$_2$ Solid Solution for Sodium-Ion Batteries. *Adv. Funct. Mater.* **2016**, *26* (33), 6047−6059.

(118) Qi, X.; Wang, Y.; Jiang, L.; Mu, L.; Zhao, C.; Liu, L.; Hu, Y.-S.; Chen, L.; Huang, X. Sodium-Deficient O3-Na$_{0.9}$[Ni$_{0.4}$Mn$_x$Ti$_{0.6-x}$]O$_2$ Layered-Oxide Cathode Materials for Sodium-Ion Batteries. *Part. Part. Syst. Charact.* **2016**, *33* (8), 538−544.

(119) Wang, P.-F.; Yao, H.-R.; Liu, X.-Y.; Zhang, J.-N.; Gu, L.; Yu, X.-Q.; Yin, Y.-X.; Guo, Y.-G. Ti-Substituted NaNi$_{0.5}$Mn$_{0.5-x}$Ti$_x$O$_2$ Cathodes with Reversible O3-P3 Phase Transition for High-

Performance Sodium-Ion Batteries. *Adv. Mater.* **2017**, *29* (19), 1700210.

(120) Su, N.; Lyu, Y.; Guo, B. Electrochemical and In-Situ X-Ray Diffraction Studies of Na1.2Ni0.2Mn0.2Ru0.4O2 as a Cathode Material for Sodium-Ion Batteries. *Electrochem. Commun.* **2018**, *87*, 71−75.

(121) Zhang, G.; Xiong, T.; Yan, M.; Xu, Y.; Ren, W.; Xu, X.; Wei, Q.; Mai, L. In Operando Probing of Sodium-Incorporation in NASICON Nanomaterial: Asymmetric Reaction and Electrochemical Phase Diagram. *Chem. Mater.* **2017**, *29* (19), 8057−8064.

(122) Zhu, T.; Hu, P.; Wang, X.; Liu, Z.; Luo, W.; Owusu, K. A.; Cao, W.; Shi, C.; Li, J.; Zhou, L.; Mai, L. Realizing Three-Electron Redox Reactions in NASICON-Structured Na $_3$ MnTi(PO $_4$) $_3$ for Sodium-Ion Batteries. *Adv. Energy Mater.* **2019**, *9* (9), 1803436.

(123) Wang, W.; Gang, Y.; Hu, Z.; Yan, Z.; Li, W.; Li, Y.; Gu, Q.-F.; Wang, Z.; Chou, S.-L.; Liu, H.-K.; Dou, S.-X. Reversible Structural Evolution of Sodium-Rich Rhombohedral Prussian Blue for Sodium-Ion Batteries. *Nat. Commun.* **2020**, *11* (1), 980.

(124) Palaniselvam, T.; Goktas, M.; Anothumakkool, B.; Sun, Y.; Schmuch, R.; Zhao, L.; Han, B.; Winter, M.; Adelhelm, P. Sodium Storage and Electrode Dynamics of Tin-Carbon Composite Electrodes from Bulk Precursors for Sodium-Ion Batteries. *Adv. Funct. Mater.* **2019**, *29* (18), 1900790.

(125) Palaniselvam, T.; Babu, B.; Moon, H.; Hasa, I.; Santhosha, A. L.; Goktas, M.; Sun, Y.; Zhao, L.; Han, B.; Passerini, S.; Balducci, A.; Adelhelm, P. Tin-Containing Graphite for Sodium-Ion Batteries and Hybrid Capacitors. *Batteries & Supercaps* **2021**, *4* (1), 173−182.

(126) Ellis, L. D.; Hatchard, T. D.; Obrovac, M. N. Reversible Insertion of Sodium in Tin. *J. Electrochem. Soc.* **2012**, *159* (11), A1801−A1805.

(127) Zhou, J.; Chen, J.; Chen, M.; Wang, J.; Liu, X.; Wei, B.; Wang, Z.; Li, J.; Gu, L.; Zhang, Q.; Wang, H.; Guo, L. Few-Layer Bismuthene with Anisotropic Expansion for High-Areal-Capacity Sodium-Ion Batteries. *Adv. Mater.* **2019**, *31* (12), 1807874.

(128) Gao, H.; Yan, X.; Niu, J.; Zhang, Y.; Song, M.; Shi, Y.; Ma, W.; Qin, J.; Zhang, Z. Scalable Structural Refining via Altering Working Pressure and In-Situ Electrochemically-Driven Cu-Sb Alloying of Magnetron Sputtered Sb Anode in Sodium Ion Batteries. *Chem. Eng. J.* **2020**, *388*, 124299.

(129) Ellis, L. D.; Wilkes, B. N.; Hatchard, T. D.; Obrovac, M. N. In Situ XRD Study of Silicon, Lead and Bismuth Negative Electrodes in Nonaqueous Sodium Cells. *J. Electrochem. Soc.* **2014**, *161* (3), A416−A421.

(130) Ma, W.; Yin, K.; Gao, H.; Niu, J.; Peng, Z.; Zhang, Z. Alloying Boosting Superior Sodium Storage Performance in Nanoporous Tin-Antimony Alloy Anode for Sodium Ion Batteries. *Nano Energy* **2018**, *54*, 349−359.

(131) Guo, S.; Li, H.; Lu, Y.; Liu, Z.; Hu, X. Lattice Softening Enables Highly Reversible Sodium Storage in Anti-Pulverization Bi-Sb Alloy/Carbon Nanofibers. *Energy Storage Materials* **2020**, *27*, 270−278.

(132) Edison, E.; Sreejith, S.; Madhavi, S. Melt-Spun Fe-Sb Intermetallic Alloy Anode for Performance Enhanced Sodium-Ion Batteries. *ACS Appl. Mater. Interfaces* **2017**, *9* (45), 39399−39406.

(133) Xiao, Y.; Su, D.; Wang, X.; Wu, S.; Zhou, L.; Shi, Y.; Fang, S.; Cheng, H.-M.; Li, F. CuS Microspheres with Tunable Interlayer Space and Micropore as a High-Rate and Long-Life Anode for Sodium-Ion Batteries. *Adv. Energy Mater.* **2018**, *8* (22), 1800930.

(134) Huang, Z.; Hou, H.; Wang, C.; Li, S.; Zhang, Y.; Ji, X. Molybdenum Phosphide: A Conversion-Type Anode for Ultralong-Life Sodium-Ion Batteries. *Chem. Mater.* **2017**, *29* (17), 7313−7322.

(135) Yang, D.; Chen, W.; Zhang, X.; Mi, L.; Liu, C.; Chen, L.; Guan, X.; Cao, Y.; Shen, C. Facile and Scalable Synthesis of Low-Cost FeS@C as Long-Cycle Anodes for Sodium-Ion Batteries. *J. Mater. Chem. A* **2019**, *7* (34), 19709−19718.

(136) Ou, X.; Xiong, X.; Zheng, F.; Yang, C.; Lin, Z.; Hu, R.; Jin, C.; Chen, Y.; Liu, M. In Situ X-Ray Diffraction Characterization of NbS2 Nanosheets as the Anode Material for Sodium Ion Batteries. *J. Power Sources* **2016**, *325*, 410−416.

(137) Sun, R.; Liu, S.; Wei, Q.; Sheng, J.; Zhu, S.; An, Q.; Mai, L. Mesoporous NiS $_2$ Nanospheres Anode with Pseudocapacitance for High-Rate and Long-Life Sodium-Ion Battery. *Small* **2017**, *13* (39), 1701744.

(138) Ou, X.; Yang, C.; Xiong, X.; Zheng, F.; Pan, Q.; Jin, C.; Liu, M.; Huang, K. A New RGO-Overcoated Sb $_2$ Se $_3$ Nanorods Anode for Na + Battery: In Situ X-Ray Diffraction Study on a Live Sodiation/Desodiation Process. *Adv. Funct. Mater.* **2017**, *27* (13), 1606242.

(139) Ma, T.; Xu, G.-L.; Zeng, X.; Li, Y.; Ren, Y.; Sun, C.; Heald, S. M.; Jorne, J.; Amine, K.; Chen, Z. Solid State Synthesis of Layered Sodium Manganese Oxide for Sodium-Ion Battery by in-Situ High Energy X-Ray Diffraction and X-Ray Absorption near Edge Spectroscopy. *J. Power Sources* **2017**, *341*, 114−121.

(140) Dai, H.; Yang, C.; Ou, X.; Liang, X.; Xue, H.; Wang, W.; Xu, G. Unravelling the Electrochemical Properties and Thermal Behavior of NaNi2/3Sb1/3O2 Cathode for Sodium-Ion Batteries by in Situ X-Ray Diffraction Investigation. *Electrochim. Acta* **2017**, *257*, 146−154.

(141) *X-Ray Absorption Spectroscopy of Semiconductors*; Schnohr, C. S., Ridgway, M. C., Eds.; Springer Series in Optical Sciences; Springer: Berlin Heidelberg, 2015; Vol. *190*. DOI: 10.1007/978-3-662-44362-0.

(142) Bunker, G. *Introduction to XAFS: A Practical Guide to X-Ray Absorption Fine Structure Spectroscopy*; Cambridge University Press: Cambridge, 2010; p 270.

(143) Ravel, B.; Newville, M. ATHENA, ARTEMIS, HEPHAESTUS: Data Analysis for X-Ray Absorption Spectroscopy Using IFEFFIT. *J. Synchrotron Radiat.* **2005**, *12* (4), 537−541.

(144) McBreen, J. The Application of Synchrotron Techniques to the Study of Lithium-Ion Batteries. *J. Solid State Electrochem.* **2009**, *13* (7), 1051−1061.

(145) Axnanda, S.; Crumlin, E. J.; Mao, B.; Rani, S.; Chang, R.; Karlsson, P. G.; Edwards, M. O. M.; Lundqvist, M.; Moberg, R.; Ross, P.; Hussain, Z.; Liu, Z. Using "Tender" X-Ray Ambient Pressure X-Ray Photoelectron Spectroscopy as A Direct Probe of Solid-Liquid Interface. *Sci. Rep.* **2015**, *5* (1), 9788.

(146) Zhu, W.; Wang, Y.; Liu, D.; Gariépy, V.; Gagnon, C.; Vijh, A.; Trudeau, M.; Zaghib, K. Application of Operando X-Ray Diffractometry in Various Aspects of the Investigations of Lithium/Sodium-Ion Batteries. *Energies* **2018**, *11* (11), 2963.

(147) Fehse, M.; Henry, A.; Zitolo, A.; Boury, B.; Louvain, N.; Stievano, L. Revisiting the Sodiation Mechanism of TiO2 via Operando X-Ray Absorption Spectroscopy. *Appl. Sci.* **2020**, *10* (16), 5547.

(148) Siebert, A.; Dou, X.; Garcia-Diez, R.; Buchholz, D.; Félix, R.; Handick, E.; Greco, G.; Hasa, I.; Wilks, R. G.; Passerini, S.; Bär, M. Monitoring the Sodiation Mechanism of Anatase TiO $_2$ Nanoparticle-Based Electrodes for Sodium-Ion Batteries by *Operando* XANES Measurements. *ACS Appl. Energy Mater.* **2021**, *4*, 164.

(149) Deng, C.; Gabriel, E.; Skinner, P.; Lee, S.; Barnes, P.; Ma, C.; Gim, J.; Lau, M. L.; Lee, E.; Xiong, H. Origins of Irreversibility in Layered NaNixFeyMnzO2 Cathode Materials for Sodium Ion Batteries. *ACS Appl. Mater. Interfaces* **2020**, *12* (46), 51397−51408.

(150) Karan, N. K.; Slater, M. D.; Dogan, F.; Kim, D.; Johnson, C. S.; Balasubramanian, M. Operando Structural Characterization of the Lithium-Substituted Layered Sodium-Ion Cathode Material P2-Na $_{0.85}$ Li $_{0.17}$ Ni $_{0.21}$ Mn $_{0.64}$ O $_2$ by X-Ray Absorption Spectroscopy. *J. Electrochem. Soc.* **2014**, *161* (6), A1107−A1115.

(151) Ma, C.; Alvarado, J.; Xu, J.; Clément, R. J.; Kodur, M.; Tong, W.; Grey, C. P.; Meng, Y. S. Exploring Oxygen Activity in the High Energy P2-Type Na $_{0.78}$ Ni $_{0.23}$ Mn $_{0.69}$ O $_2$ Cathode Material for Na-Ion Batteries. *J. Am. Chem. Soc.* **2017**, *139* (13), 4835−4845.

(152) Cheng, J.-H.; Pan, C.-J.; Lee, J.-F.; Chen, J.-M.; Guignard, M.; Delmas, C.; Carlier, D.; Hwang, B.-J. Simultaneous Reduction of Co3+ and Mn4+ in P2-Na2/3Co2/3Mn1/3O2 As Evidenced by X-ray Absorption Spectroscopy during Electrochemical Sodium Intercalation. *Chem. Mater.* **2014**, *26* (2), 1219−1225.

(153) Mortemard de Boisse, B.; Cheng, J.-H.; Carlier, D.; Guignard, M.; Pan, C.-J.; Bordère, S.; Filimonov, D.; Drathen, C.; Suard, E.;

Hwang, B.-J.; Wattiaux, A.; Delmas, C. O3-Na$_x$ Mn$_{1/3}$ Fe$_{2/3}$ O$_2$ as a Positive Electrode Material for Na-Ion Batteries: Structural Evolutions and Redox Mechanisms upon Na + (de)Intercalation. *J. Mater. Chem. A* **2015**, *3* (20), 10976−10989.

(154) Ding, J. J.; Zhou, Y. N.; Sun, Q.; Yu, X. Q.; Yang, X. Q.; Fu, Z. W. Electrochemical Properties of P2-Phase Na0.74CoO2 Compounds as Cathode Material for Rechargeable Sodium-Ion Batteries. *Electrochim. Acta* **2013**, *87*, 388−393.

(155) Seok, J.; Yu, S.-H.; Abruña, H. D. *Operando* Synchrotron-Based X-Ray Study of Prussian Blue and Its Analogue as Cathode Materials for Sodium-Ion Batteries. *J. Phys. Chem. C* **2020**, *124* (30), 16332−16337.

(156) Keller, M.; Eisenmann, T.; Meira, D.; Aquilanti, G.; Buchholz, D.; Bresser, D.; Passerini, S. In Situ Investigation of Layered Oxides with Mixed Structures for Sodium-Ion Batteries. *Small Methods* **2019**, *3* (11), 1900239.

(157) Maletti, S.; Sarapulova, A.; Schökel, A.; Mikhailova, D. *Operando* Studies on the NaNi$_{0.5}$ Ti$_{0.5}$ O$_2$ Cathode for Na-Ion Batteries: Elucidating Titanium as a Structure Stabilizer. *ACS Appl. Mater. Interfaces* **2019**, *11* (37), 33923−33930.

(158) Huang, W.; Zhou, J.; Li, B.; Ma, J.; Tao, S.; Xia, D.; Chu, W.; Wu, Z. Detailed Investigation of Na2.24FePO4CO3 as a Cathode Material for Na-Ion Batteries. *Sci. Rep.* **2015**, *4* (1), 4188.

(159) Susanto, D.; Cho, M. K.; Ali, G.; Kim, J.-Y.; Chang, H. J.; Kim, H.-S.; Nam, K.-W.; Chung, K. Y. Anionic Redox Activity as a Key Factor in the Performance Degradation of NaFeO$_2$ Cathodes for Sodium Ion Batteries. *Chem. Mater.* **2019**, *31* (10), 3644−3651.

(160) Zhou, D.; Wang, J.; Liu, X.; He, X.; Sun, F.; Murzin, V.; Schumacher, G.; Yao, X.; Winter, M.; Li, J. Operando X-Ray Absorption Spectroscopy Investigations on NaxNi1/3Fe1/3Mn1/3O2 Positive Electrode Materials for Sodium and Sodium Ion Batteries. *J. Power Sources* **2020**, *473*, 228557.

(161) Darwiche, A.; Fehse, M.; Mahmoud, A.; La Fontaine, C.; Fraisse, B.; Hermann, R.; Doublet, M.-L.; Monconduit, L.; Sougrati, M.; Ben Yahia, M.; Stievano, L. The Electrochemical Sodiation of Sb Investigated by Operando X-Ray Absorption and 121Sb Mössbauer Spectroscopy: What Does One Really Learn? *Batteries* **2018**, *4* (2), 25.

(162) Fehse, M.; Sougrati, M. T.; Darwiche, A.; Gabaudan, V.; La Fontaine, C.; Monconduit, L.; Stievano, L. Elucidating the Origin of Superior Electrochemical Cycling Performance: New Insights on Sodiation-Desodiation Mechanism of SnSb from *Operando* Spectroscopy. *J. Mater. Chem. A* **2018**, *6* (18), 8724−8734.

(163) Kim, M.-K.; Yu, S.-H.; Jin, A.; Kim, J.; Ko, I.-H.; Lee, K.-S.; Mun, J.; Sung, Y.-E. Bismuth Oxide as a High Capacity Anode Material for Sodium-Ion Batteries. *Chem. Commun.* **2016**, *52* (79), 11775−11778.

(164) Weng, Y.-T.; Huang, T.-Y.; Lim, C.-H.; Shao, P.-S.; Hy, S.; Kuo, C.-Y.; Cheng, J.-H.; Hwang, B.-J.; Lee, J.-F.; Wu, N.-L. An Unexpected Large Capacity of Ultrafine Manganese Oxide as a Sodium-Ion Battery Anode. *Nanoscale* **2015**, *7* (47), 20075−20081.

(165) Patra, J.; Chen, H.-C.; Yang, C.-H.; Hsieh, C.-T.; Su, C.-Y.; Chang, J.-K. High Dispersion of 1-Nm SnO2 Particles between Graphene Nanosheets Constructed Using Supercritical CO2 Fluid for Sodium-Ion Battery Anodes. *Nano Energy* **2016**, *28*, 124−134.

(166) Dixon, D.; Avila, M.; Ehrenberg, H.; Bhaskar, A. Difference in Electrochemical Mechanism of SnO2 Conversion in Lithium-Ion and Sodium-Ion Batteries: Combined in Operando and Ex Situ XAS Investigations. *ACS Omega* **2019**, *4* (6), 9731−9738.

(167) Xu, G.-L.; Sheng, T.; Chong, L.; Ma, T.; Sun, C.-J.; Zuo, X.; Liu, D.-J.; Ren, Y.; Zhang, X.; Liu, Y.; Heald, S. M.; Sun, S.-G.; Chen, Z.; Amine, K. Insights into the Distinct Lithiation/Sodiation of Porous Cobalt Oxide by in Operando Synchrotron X-ray Techniques and Ab Initio Molecular Dynamics Simulations. *Nano Lett.* **2017**, *17* (2), 953−962.

(168) Kim, H.; Kim, H.; Kim, H.; Kim, J.; Yoon, G.; Lim, K.; Yoon, W.-S.; Kang, K. Understanding Origin of Voltage Hysteresis in Conversion Reaction for Na Rechargeable Batteries: The Case of Cobalt Oxides. *Adv. Funct. Mater.* **2016**, *26* (28), 5042−5050.

(169) Zhao, Y.; Fu, Q.; Wang, D.; Pang, Q.; Gao, Y.; Missiul, A.; Nemausat, R.; Sarapulova, A.; Ehrenberg, H.; Wei, Y.; Chen, G. Co9S8@carbon Yolk-Shell Nanocages as a High Performance Direct Conversion Anode Material for Sodium Ion Batteries. *Energy Storage Materials* **2019**, *18*, 51−58.

(170) Smith, J. W.; Saykally, R. J. Soft X-Ray Absorption Spectroscopy of Liquids and Solutions. *Chem. Rev.* **2017**, *117* (23), 13909−13934.

(171) Lin, F.; Nordlund, D.; Markus, I. M.; Weng, T.-C.; Xin, H. L.; Doeff, M. M. Profiling the Nanoscale Gradient in Stoichiometric Layered Cathode Particles for Lithium-Ion Batteries. *Energy Environ. Sci.* **2014**, *7* (9), 3077.

(172) Yang, W.; Qiao, R. Soft X-Ray Spectroscopy for Probing Electronic and Chemical States of Battery Materials. *Chin. Phys. B* **2016**, *25* (1), 017104.

(173) Wu, J.; Shen, Z.; Yang, W. Redox Mechanism in Na-Ion Battery Cathodes Probed by Advanced Soft X-Ray Spectroscopy. *Front. Chem.* **2020**, *8*, 816.

(174) Yoon, W.-S.; Balasubramanian, M.; Chung, K. Y.; Yang, X.-Q.; McBreen, J.; Grey, C. P.; Fischer, D. A. Investigation of the Charge Compensation Mechanism on the Electrochemically Li-Ion Deintercalated Li$_{1-x}$ Co$_{1/3}$ Ni$_{1/3}$ Mn$_{1/3}$ O$_2$ Electrode System by Combination of Soft and Hard X-Ray Absorption Spectroscopy. *J. Am. Chem. Soc.* **2005**, *127* (49), 17479−17487.

(175) Nanba, Y.; Iwao, T.; de Boisse, B. M.; Zhao, W.; Hosono, E.; Asakura, D.; Niwa, H.; Kiuchi, H.; Miyawaki, J.; Harada, Y.; Okubo, M.; Yamada, A. Redox Potential Paradox in Na$_x$MO$_2$ for Sodium-Ion Battery Cathodes. *Chem. Mater.* **2016**, *28* (4), 1058−1065.

(176) Dai, K.; Mao, J.; Zhuo, Z.; Feng, Y.; Mao, W.; Ai, G.; Pan, F.; Chuang, Y.; Liu, G.; Yang, W. Negligible Voltage Hysteresis with Strong Anionic Redox in Conventional Battery Electrode. *Nano Energy* **2020**, *74*, 104831.

(177) Wang, L.; Song, J.; Qiao, R.; Wray, L. A.; Hossain, M. A.; Chuang, Y.-D.; Yang, W.; Lu, Y.; Evans, D.; Lee, J.-J.; Vail, S.; Zhao, X.; Nishijima, M.; Kakimoto, S.; Goodenough, J. B. Rhombohedral Prussian White as Cathode for Rechargeable Sodium-Ion Batteries. *J. Am. Chem. Soc.* **2015**, *137* (7), 2548−2554.

(178) Li, Q.; Qiao, R.; Wray, L. A.; Chen, J.; Zhuo, Z.; Chen, Y.; Yan, S.; Pan, F.; Hussain, Z.; Yang, W. Quantitative Probe of the Transition Metal Redox in Battery Electrodes through Soft X-Ray Absorption Spectroscopy. *J. Phys. D: Appl. Phys.* **2016**, *49* (41), 413003.

(179) Li, Y.; Gao, Y.; Wang, X.; Shen, X.; Kong, Q.; Yu, R.; Lu, G.; Wang, Z.; Chen, L. Iron Migration and Oxygen Oxidation during Sodium Extraction from NaFeO2. *Nano Energy* **2018**, *47*, 519−526.

(180) Chen, X.; Li, N.; Kedzie, E.; McCloskey, B. D.; Tang, H.; Tong, W. High-Capacity P2-Type Na$_x$ Li$_{0.25}$ Mn$_{0.75}$ O$_2$ Cathode Enabled by Anionic Oxygen Redox. *J. Electrochem. Soc.* **2019**, *166* (16), A4136−A4140.

(181) Deng, C.; Skinner, P.; Liu, Y.; Sun, M.; Tong, W.; Ma, C.; Lau, M. L.; Hunt, R.; Barnes, P.; Xu, J.; Xiong, H. Li-Substituted Layered Spinel Cathode Material for Sodium Ion Batteries. *Chem. Mater.* **2018**, *30* (22), 8145−8154.

(182) Mason, C. W.; Lange, F.; Saravanan, K.; Lin, F.; Nordlund, D. Beyond Divalent Copper: A Redox Couple for Sodium Ion Battery Cathode Materials. *ECS Electrochem. Lett.* **2015**, *4* (5), A41−A44.

(183) Xu, H.; Cheng, C.; Chu, S.; Zhang, X.; Wu, J.; Zhang, L.; Guo, S.; Zhou, H. Anion-Cation Synergetic Contribution to High Capacity, Structurally Stable Cathode Materials for Sodium-Ion Batteries. *Adv. Funct. Mater.* **2020**, *30* (50), 2005164.

(184) Rong, X.; Hu, E.; Lu, Y.; Meng, F.; Zhao, C.; Wang, X.; Zhang, Q.; Yu, X.; Gu, L.; Hu, Y.-S.; Li, H.; Huang, X.; Yang, X.-Q.; Delmas, C.; Chen, L. Anionic Redox Reaction-Induced High-Capacity and Low-Strain Cathode with Suppressed Phase Transition. *Joule* **2019**, *3* (2), 503−517.

(185) Rong, X.; Liu, J.; Hu, E.; Liu, Y.; Wang, Y.; Wu, J.; Yu, X.; Page, K.; Hu, Y.-S.; Yang, W.; Li, H.; Yang, X.-Q.; Chen, L.; Huang, X. Structure-Induced Reversible Anionic Redox Activity in Na Layered Oxide Cathode. *Joule* **2018**, *2* (1), 125−140.

(186) Sato, K.; Nakayama, M.; Glushenkov, A. M.; Mukai, T.; Hashimoto, Y.; Yamanaka, K.; Yoshimura, M.; Ohta, T.; Yabuuchi, N. Na-Excess Cation-Disordered Rocksalt Oxide: $Na_{1.3}Nb_{0.3}Mn_{0.4}O_2$. *Chem. Mater.* **2017**, *29* (12), 5043−5047.

(187) Yang, W.; Devereaux, T. P. Anionic and Cationic Redox and Interfaces in Batteries: Advances from Soft X-Ray Absorption Spectroscopy to Resonant Inelastic Scattering. *J. Power Sources* **2018**, *389*, 188−197.

(188) Zhang, Y.; Yang, Z.; Tian, C. Probing and Quantifying Cathode Charge Heterogeneity in Li Ion Batteries. *J. Mater. Chem. A* **2019**, *7* (41), 23628−23661.

(189) Mu, L.; Feng, X.; Kou, R.; Zhang, Y.; Guo, H.; Tian, C.; Sun, C.-J.; Du, X.-W.; Nordlund, D.; Xin, H. L.; Lin, F. Deciphering the Cathode-Electrolyte Interfacial Chemistry in Sodium Layered Cathode Materials. *Adv. Energy Mater.* **2018**, *8* (34), 1801975.

(190) Altin, S.; Oz, E.; Altin, E.; Demirel, S.; Bayri, A.; Avci, S. Investigations of the Capacity Fading Mechanism of $Na_{0.44}MnO_2$ via *Ex Situ* XAS and Magnetization Measurements. *Dalton Trans.* **2018**, *47* (47), 17102−17108.

(191) Qiao, R.; Dai, K.; Mao, J.; Weng, T.-C.; Sokaras, D.; Nordlund, D.; Song, X.; Battaglia, V. S.; Hussain, Z.; Liu, G.; Yang, W. Revealing and Suppressing Surface Mn(II) Formation of $Na0.44MnO_2$ Electrodes for Na-Ion Batteries. *Nano Energy* **2015**, *16*, 186−195.

(192) Wang, P.; Weng, M.; Xiao, Y.; Hu, Z.; Li, Q.; Li, M.; Wang, Y.; Chen, X.; Yang, X.; Wen, Y.; Yin, Y.; Yu, X.; Xiao, Y.; Zheng, J.; Wan, L.; Pan, F.; Guo, Y. An Ordered Ni_6-Ring Superstructure Enables a Highly Stable Sodium Oxide Cathode. *Adv. Mater.* **2019**, *31* (43), 1903483.

(193) Hakim, C.; Sabi, N.; Ma, L. A.; Dahbi, M.; Brandell, D.; Edström, K.; Duda, L. C.; Saadoune, I.; Younesi, R. Understanding the Redox Process upon Electrochemical Cycling of the P2-$Na0.78Co1/2Mn1/3Ni1/6O2$ Electrode Material for Sodium-Ion Batteries. *Commun Chem* **2020**, *3* (1), 9.

(194) Huang, Y.; Yan, Z.; Luo, W.; Hu, Z.; Liu, G.; Zhang, L.; Yang, X.; Ou, M.; Liu, W.; Huang, L.; Lin, H.; Chen, C.-T.; Luo, J.; Li, S.; Han, J.; Chou, S.; Huang, Y. Vitalization of P2-$Na2/3Ni1/3Mn2/3O2$ at High-Voltage Cyclability via Combined Structural Modulation for Sodium-Ion Batteries. *Energy Storage Materials* **2020**, *29*, 182−189.

(195) Ma, C.; Alvarado, J.; Xu, J.; Clément, R. J.; Kodur, M.; Tong, W.; Grey, C. P.; Meng, Y. S. Exploring Oxygen Activity in the High Energy P2-Type $Na_{0.78}Ni_{0.23}Mn_{0.69}O_2$ Cathode Material for Na-Ion Batteries. *J. Am. Chem. Soc.* **2017**, *139* (13), 4835−4845.

(196) Liu, Y.; Fang, X.; Zhang, A.; Shen, C.; Liu, Q.; Enaya, H. A.; Zhou, C. Layered P2-$Na2/3[Ni1/3Mn2/3]O2$ as High-Voltage Cathode for Sodium-Ion Batteries: The Capacity Decay Mechanism and $Al2O3$ Surface Modification. *Nano Energy* **2016**, *27*, 27−34.

(197) Mu, L.; Rahman, M. M.; Zhang, Y.; Feng, X.; Du, X.-W.; Nordlund, D.; Lin, F. Surface Transformation by a "Cocktail" Solvent Enables Stable Cathode Materials for Sodium Ion Batteries. *J. Mater. Chem. A* **2018**, *6* (6), 2758−2766.

(198) Xu, S.; Wu, J.; Hu, E.; Li, Q.; Zhang, J.; Wang, Y.; Stavitski, E.; Jiang, L.; Rong, X.; Yu, X.; Yang, W.; Yang, X.-Q.; Chen, L.; Hu, Y.-S. Suppressing the Voltage Decay of Low-Cost P2-Type Iron-Based Cathode Materials for Sodium-Ion Batteries. *J. Mater. Chem. A* **2018**, *6* (42), 20795−20803.

(199) Rahman, M. M.; Zhang, Y.; Xia, S.; Kan, W. H.; Avdeev, M.; Mu, L.; Sokaras, D.; Kroll, T.; Du, X.-W.; Nordlund, D.; Liu, Y.; Lin, F. Surface Characterization of Li-Substituted Compositionally Heterogeneous $NaLi_{0.045}Cu_{0.185}Fe_{0.265}Mn_{0.505}O_2$ Sodium-Ion Cathode Material. *J. Phys. Chem. C* **2019**, *123* (18), 11428−11435.

(200) Xiao, W.; Sun, Q.; Banis, M. N.; Wang, B.; Li, W.; Li, M.; Lushington, A.; Li, R.; Li, X.; Sham, T.; Sun, X. Understanding the Critical Role of Binders in Phosphorus/Carbon Anode for Sodium-Ion Batteries through Unexpected Mechanism. *Adv. Funct. Mater.* **2020**, *30* (32), 2000060.

(201) Xiao, W.; Sun, Q.; Banis, M. N.; Wang, B.; Liang, J.; Lushington, A.; Li, R.; Li, X.; Sham, T.-K.; Sun, X. Unveiling the Interfacial Instability of the Phosphorus/Carbon Anode for Sodium-Ion Batteries. *ACS Appl. Mater. Interfaces* **2019**, *11* (34), 30763−30773.

(202) Balasubramanian, M.; Lee, H. S.; Sun, X.; Yang, X. Q.; Moodenbaugh, A. R.; McBreen, J.; Fischer, D. A.; Fu, Z. Formation of SEI on Cycled Lithium-Ion Battery Cathodes: Soft X-Ray Absorption Study. *Electrochem. Solid-State Lett.* **2002**, *5* (1), A22.

(203) Augustsson, A.; Herstedt, M.; Guo, J.-H.; Edström, K.; Zhuang, G. V.; Ross, P. N., Jr.; Rubensson, J.-E.; Nordgren, J. Solid Electrolyte Interphase on Graphite Li-Ion Battery Anodes Studied by Soft X-Ray Spectroscopy. *Phys. Chem. Chem. Phys.* **2004**, *6* (16), 4185−4189.

(204) Kim, Y.; Kim, D. S.; Um, J. H.; Yoon, J.; Kim, J. M.; Kim, H.; Yoon, W.-S. Revisiting Solid Electrolyte Interphase on the Carbonaceous Electrodes Using Soft X-Ray Absorption Spectroscopy. *ACS Appl. Mater. Interfaces* **2018**, *10* (35), 29992−29999.

(205) Maibach, J.; Jeschull, F.; Brandell, D.; Edström, K.; Valvo, M. Surface Layer Evolution on Graphite During Electrochemical Sodium-Tetraglyme Co-Intercalation. *ACS Appl. Mater. Interfaces* **2017**, *9* (14), 12373−12381.

(206) Zhang, J.; Wang, D.-W.; Lv, W.; Zhang, S.; Liang, Q.; Zheng, D.; Kang, F.; Yang, Q.-H. Achieving Superb Sodium Storage Performance on Carbon Anodes through an Ether-Derived Solid Electrolyte Interphase. *Energy Environ. Sci.* **2017**, *10* (1), 370−376.

(207) Rezvani, S. J.; Nobili, F.; Gunnella, R.; Ali, M.; Tossici, R.; Passerini, S.; Di Cicco, A. SEI Dynamics in Metal Oxide Conversion Electrodes of Li-Ion Batteries. *J. Phys. Chem. C* **2017**, *121* (47), 26379−26388.

(208) Di Cicco, A.; Giglia, A.; Gunnella, R.; Koch, S. L.; Mueller, F.; Nobili, F.; Pasqualini, M.; Passerini, S.; Tossici, R.; Witkowska, A. SEI Growth and Depth Profiling on ZFO Electrodes by Soft X-Ray Absorption Spectroscopy. *Adv. Energy Mater.* **2015**, *5* (18), 1500642.

(209) Qiao, R.; Lucas, I. T.; Karim, A.; Syzdek, J.; Liu, X.; Chen, W.; Persson, K.; Kostecki, R.; Yang, W. Distinct Solid-Electrolyte-Interphases on Sn (100) and (001) Electrodes Studied by Soft X-Ray Spectroscopy. *Adv. Mater. Interfaces* **2014**, *1* (3), 1300115.

(210) Mu, L.; Hou, Q.; Yang, Z.; Zhang, Y.; Rahman, M. M.; Kautz, D. J.; Sun, E.; Du, X.-W.; Du, Y.; Nordlund, D.; Lin, F. Water-Processable P2-$Na_{0.67}Ni_{0.22}Cu_{0.11}Mn_{0.56}Ti_{0.11}O_2$ Cathode Material for Sodium Ion Batteries. *J. Electrochem. Soc.* **2019**, *166* (2), A251−A257.

(211) Tesch, M. F.; Bonke, S. A.; Jones, T. E.; Shaker, M. N.; Xiao, J.; Skorupska, K.; Mom, R.; Melder, J.; Kurz, P.; Knop-Gericke, A.; Schlögl, R.; Hocking, R. K.; Simonov, A. N. Evolution of Oxygen-Metal Electron Transfer and Metal Electronic States During Manganese Oxide Catalyzed Water Oxidation Revealed with In Situ Soft X-Ray Spectroscopy. *Angew. Chem., Int. Ed.* **2019**, *58* (11), 3426−3432.

(212) Beaumont, S. K. Soft XAS as an *in Situ* Technique for the Study of Heterogeneous Catalysts. *Phys. Chem. Chem. Phys.* **2020**, *22* (34), 18747−18756.

(213) Yamamoto, K.; Zhou, Y.; Yabuuchi, N.; Nakanishi, K.; Yoshinari, T.; Kobayashi, T.; Kobayashi, Y.; Yamamoto, R.; Watanabe, A.; Orikasa, Y.; Tsuruta, K.; Park, J.; Byon, H. R.; Tamenori, Y.; Ohta, T.; Uchimoto, Y. Charge Compensation Mechanism of Lithium-Excess Metal Oxides with Different Covalent and Ionic Characters Revealed by *Operando* Soft and Hard X-Ray Absorption Spectroscopy. *Chem. Mater.* **2020**, *32* (1), 139−147.

(214) Wang, L.; Wang, J.; Zuo, P. Probing Battery Electrochemistry with In Operando Synchrotron X-Ray Imaging Techniques. *Small Methods* **2018**, *2* (8), 1700293.

(215) Heenan, T. M. M.; Tan, C.; Hack, J.; Brett, D. J. L.; Shearing, P. R. Developments in X-Ray Tomography Characterization for Electrochemical Devices. *Mater. Today* **2019**, *31*, 69−85.

(216) Wei, C.; Xia, S.; Huang, H.; Mao, Y.; Pianetta, P.; Liu, Y. Mesoscale Battery Science: The Behavior of Electrode Particles Caught on a Multispectral X-Ray Camera. *Acc. Chem. Res.* **2018**, *51* (10), 2484−2492.

(217) Liu, Y.; Nelson, J.; Holzner, C.; Andrews, J. C.; Pianetta, P. Recent Advances in Synchrotron-Based Hard x-Ray Phase Contrast Imaging. *J. Phys. D: Appl. Phys.* **2013**, *46* (49), 494001.

(218) Tian, C.; Xu, Y.; Nordlund, D.; Lin, F.; Liu, J.; Sun, Z.; Liu, Y.; Doeff, M. Charge Heterogeneity and Surface Chemistry in Polycrystalline Cathode Materials. *Joule* **2018**, *2* (3), 464−477.

(219) Xie, Y.; Wang, H.; Xu, G.; Wang, J.; Sheng, H.; Chen, Z.; Ren, Y.; Sun, C.-J.; Wen, J.; Wang, J.; Miller, D. J.; Lu, J.; Amine, K.; Ma, Z.-F. In Operando XRD and TXM Study on the Metastable Structure Change of NaNi$_{1/3}$Fe$_{1/3}$Mn$_{1/3}$O$_2$ under Electrochemical Sodium-Ion Intercalation. *Adv. Energy Mater.* **2016**, *6* (24), 1601306.

(220) Wang, L.; Wang, J.; Zhang, X.; Ren, Y.; Zuo, P.; Yin, G.; Wang, J. Unravelling the Origin of Irreversible Capacity Loss in NaNiO2 for High Voltage Sodium Ion Batteries. *Nano Energy* **2017**, *34*, 215−223.

(221) Wang, J.; Eng, C.; Chen-Wiegart, Y. K.; Wang, J. Probing Three-Dimensional Sodiation-Desodiation Equilibrium in Sodium-Ion Batteries by in Situ Hard X-Ray Nanotomography. *Nat. Commun.* **2015**, *6* (1), 7496.

(222) He, K.; Lin, F.; Zhu, Y.; Yu, X.; Li, J.; Lin, R.; Nordlund, D.; Weng, T.-C.; Richards, R. M.; Yang, X.-Q.; Doeff, M. M.; Stach, E. A.; Mo, Y.; Xin, H. L.; Su, D. Sodiation Kinetics of Metal Oxide Conversion Electrodes: A Comparative Study with Lithiation. *Nano Lett.* **2015**, *15* (9), 5755−5763.

(223) Yu, Z.; Wang, J.; Wang, L.; Xie, Y.; Lou, S.; Jiang, Z.; Ren, Y.; Lee, S.; Zuo, P.; Huo, H.; Yin, G.; Pan, Q.; Wang, J. Unraveling the Origins of the "Unreactive Core" in Conversion Electrodes to Trigger High Sodium-Ion Electrochemistry. *ACS Energy Lett.* **2019**, *4* (8), 2007−2012.

(224) Wang, J.; Wang, L.; Eng, C.; Wang, J. Elucidating the Irreversible Mechanism and Voltage Hysteresis in Conversion Reaction for High-Energy Sodium-Metal Sulfide Batteries. *Adv. Energy Mater.* **2017**, *7* (14), 1602706.

(225) Wang, L.; Wang, J.; Guo, F.; Ma, L.; Ren, Y.; Wu, T.; Zuo, P.; Yin, G.; Wang, J. Understanding the Initial Irreversibility of Metal Sulfides for Sodium-Ion Batteries via Operando Techniques. *Nano Energy* **2018**, *43*, 184−191.

(226) Liu, Q.; Gao, J.; Cao, C.; Yin, G.; Jiang, Z.; Ge, M.; Xiao, X.; Lee, W.-K.; Wang, J. Insights into Enhanced Sodium Ion Storage Mechanism in Fe3S4: The Coupling of Surface Chemistry, Microstructural Regulation and 3D Electronic Transport. *Nano Energy* **2019**, *62*, 384−392.

(227) Sottmann, J.; Di Michiel, M.; Fjellvåg, H.; Malavasi, L.; Margadonna, S.; Vajeeston, P.; Vaughan, G. B. M.; Wragg, D. S. Chemical Structures of Specific Sodium Ion Battery Components Determined by Operando Pair Distribution Function and X-Ray Diffraction Computed Tomography. *Angew. Chem., Int. Ed.* **2017**, *56* (38), 11385−11389.

(228) Billinge, S. J. L. The Atomic Pair Distribution Function: Past and Present. *Z. Kristallogr. - Cryst. Mater.* **2004**, *219* (3), 117−121.

(229) Lee, S.; Xu, H. Using Complementary Methods of Synchrotron Radiation Powder Diffraction and Pair Distribution Function to Refine Crystal Structures with High Quality Parameters—A Review. *Minerals* **2020**, *10* (2), 124.

(230) Qiu, X.; Thompson, J. W.; Billinge, S. J. L. PDFgetX2: A GUI-Driven Program to Obtain the Pair Distribution Function from X-Ray Powder Diffraction Data. *J. Appl. Crystallogr.* **2004**, *37* (4), 678−678.

(231) Proffen, Th; Billinge, S. J. L. PDFFIT, a Program for Full Profile Structural Refinement of the Atomic Pair Distribution Function. *J. Appl. Crystallogr.* **1999**, *32* (3), 572−575.

(232) Deng, C.; Ma, C.; Lau, M. L.; Skinner, P.; Liu, Y.; Xu, W.; Zhou, H.; Ren, Y.; Yin, Y.; Williford, B.; Dahl, M.; Xiong, H. Amorphous and Crystalline TiO2 Nanoparticle Negative Electrodes for Sodium-Ion Batteries. *Electrochim. Acta* **2019**, *321*, 134723.

(233) Mathiesen, J. K.; Väli, R.; Härmas, M.; Lust, E.; Fold von Bülow, J.; Jensen, K. M. Ø.; Norby, P. Following the In-Plane Disorder of Sodiated Hard Carbon through *Operando* Total Scattering. *J. Mater. Chem. A* **2019**, *7* (19), 11709−11717.

(234) Li, Z.; Ma, L.; Surta, T. W.; Bommier, C.; Jian, Z.; Xing, Z.; Stickle, W. F.; Dolgos, M.; Amine, K.; Lu, J.; Wu, T.; Ji, X. High Capacity of Hard Carbon Anode in Na-Ion Batteries Unlocked by PO$_x$ Doping. *ACS Energy Lett.* **2016**, *1* (2), 395−401.

(235) Allan, P. K.; Griffin, J. M.; Darwiche, A.; Borkiewicz, O. J.; Wiaderek, K. M.; Chapman, K. W.; Morris, A. J.; Chupas, P. J.; Monconduit, L.; Grey, C. P. Tracking Sodium-Antimonide Phase Transformations in Sodium-Ion Anodes: Insights from Operando Pair Distribution Function Analysis and Solid-State NMR Spectroscopy. *J. Am. Chem. Soc.* **2016**, *138* (7), 2352−2365.

(236) Stratford, J. M.; Mayo, M.; Allan, P. K.; Pecher, O.; Borkiewicz, O. J.; Wiaderek, K. M.; Chapman, K. W.; Pickard, C. J.; Morris, A. J.; Grey, C. P. Investigating Sodium Storage Mechanisms in Tin Anodes: A Combined Pair Distribution Function Analysis, Density Functional Theory, and Solid-State NMR Approach. *J. Am. Chem. Soc.* **2017**, *139* (21), 7273−7286.

(237) Spence, J. C. H. Outrunning Damage: Electrons vs X-Rays—Timescales and Mechanisms. *Struct. Dyn.* **2017**, *4* (4), 044027.

(238) Lyu, Y.; Liu, Y.; Cheng, T.; Guo, B. High-Throughput Characterization Methods for Lithium Batteries. *Journal of Materiomics* **2017**, *3* (3), 221−229.

(239) Kang, H. S.; Lee, J. Y.; Choi, S.; Kim, H.; Park, J. H.; Son, J. Y.; Kim, B. H.; Noh, S. D. Smart Manufacturing: Past Research, Present Findings, and Future Directions. *Int. J. of Precis. Eng. and Manuf.-Green Tech.* **2016**, *3* (1), 111−128.

(240) Jordan, M. I.; Mitchell, T. M. Machine Learning: Trends, Perspectives, and Prospects. *Science* **2015**, *349* (6245), 255−260.